Theoretical investigation of erythrocytes optical trapping in ray optics approximation

Riccardo Tognato

Thesis submitted for the degree of Doctor of Philosophy

Department of Physics & Astronomy
University College London (UCL)
January 2022

Declaration

I, Riccardo Tognato, confirm that the work presented in this thesis is my own. Where information has been derived from other sources, I confirm that this has been specified in the thesis.

Riccardo Tognato….....

Abstract

The thesis presents a theoretical investigation of the optical trapping of erythrocytes in the ray optics approximation. The thesis is divided in two parts: Part I provides an introduction on the general background on erythrocytes and the physics underlaying the work presented in the thesis; Part II presents the results obtained during my studies.

In the first chapter of Part II, I introduce the ray-tracing scheme useful to perform the geometrical optics calculations for a healthy red blood cell that will be used extensively in the thesis. Therefore, I present a methodology for the identification of the equilibrium configuration of a red blood cell (RBC) for the simple case of a single-beam optical tweezers. Then, I proceed to investigate the equilibrium configuration of a RBC optically trapped with a double-, triple- and four-beam optical tweezers comparing my results with experiments.

In the second chapter of Part II, I introduce a numerical scheme useful to simulate the Brownian dynamics of a non-spherical particle in a force-field (i.e. an optically trapped particle). This scheme is then applied to investigate the possibility to control the position and orientation of a

healthy RBC with a reconfigurable triple-beam optical tweezers.

In the third chapter of Part II, I investigate the possibility of optically confine and deliberately rotate a healthy RBC with a light-sheet optical tweezers (i.e. beam focused over a line instead of a point).

In the fourth chapter of Part II, I present the research carried out in collaboration with Nano-Soft Lab at CNR in Messina, Italy. Here we couple the geometrical optics calculation with machine learning to improve the accuracy and the speed of geometrical optics calculations.

Lastly, in the fifth chapter of Part II, I extend the work presented in the previous chapters to a pathological RBC conformation (i.e. sickle cell).

Impact Statement

Issue: Since its invention optical tweezers (OT) have brought unprecedented possibilities to basic and applied biophysical research. To unlock new horizons, experiments have been accompanied by a rigorous theoretical treatment, and often, the privileged methods for the description, interpretation and planning of new experiments is the geometrical optics approximation (GO). OT has been extensively applied in red blood (RBC) research to sense and screen various biochemical and biomechanical properties of erythrocytes. However, to date, nothing has been done to theoretically describe the optical trapping of healthy and pathological erythrocytes.

What has been done:

In the present work, the well-known GO approximation is applied for the first time to investigate the optical trapping of healthy and pathological RBC via OT unravelling the theoretical understanding of the RBC optical trapping.

Although GO is well-established, it is also intrinsically slow, and this results in major drawbacks that limits their application when thousands or millions of recursive calculations are needed. In collaboration with Nano-Soft Lab (CNR in Messina, Italy), I couple GO with a machine learning

algorithm to consistently decrease the computation time opening up the possibility to simulate the dynamics of a trapped RBC for longer time and multiple repetitions (tens or thousands).

Several medical conditions are associated to a change in the RBC morphology and membrane elasticity, a prominent example being sickle cell anaemia. Sensors able to screen and investigate the membrane elasticity are essential for the correct diagnosis and the following treatment of the disease. However, the sickled cell presents a very complex morphology, and the standard GO calculations are impossible in this context. For this reason, I introduce a relatively new methodology to perform GO calculations on pathological RBCs with the aim of identifying the possibility to optically trap pathological RBCs.

Impact: Overall, this work has manifold importance paving the way for experimentalists to envisage new experiments, and at the same time, providing insights on the mechanism of red blood cells trapping. The overall impact is not confined to the basic biophysical research in academia, but it can also help in making significant progress in interdisciplinary applied research outside academia underpinning future studies where the mechanical properties of the erythrocytes are investigated by deforming/stretching the RBCs through OT.

Publications and conferences:

Peer reviewed journal articles:

- **Tognato R.**, Jones P.H., “Ray Optics Model for Trapping of Biconcave Red Blood Cells in Single- and Multi-beams Optical Tweezerss”. To be submitted.
- ***Tognato R.**, *Bronte Ciriza D., Maragò O., Jones P.H., "Machine learning for the simulation of optically trapped erythrocytes". In preparation. *Authors contributed equally.
- **Tognato R.**, Jones P.H., “Theoretical investigation of optical trapping of a sickle cell with a double beam optical tweezers. In preparation.

Conference proceedings:

- **Tognato R.**, Jones P.H., “Ray Optics Model for Trapping of Biconcave Red Blood Cells in Single- and Dual-Beam Optical Tweezers” in *Biophotonics Congress* 2021, OSA Technical Digest (Optical Society of America, 2021), Washington DC, United States, ISBN 978-1-943580-85-9.

Conferences:

- OSA Biophotonics Congress, Washington, DC United States, 12-16 April 2021. Oral presentation.
- Joint 12th EBSA-10th ICBP-IUPAP Biophysics Congress Madrid, Spain, 20-24 July 2019. Poster presentation.

Schools:

- Complex nanophotonics science camp, online, July 2021.

- XXIII School of pure and applied biophysics on **"**Emerging Tools in Biomechanics: from tissues down to single molecules", Venice, Italy, 4-8 February 2019.

Prizes and awards:

- Best poster presentation in session "New Frontiers in Bioimaging" at the Joint 12th EBSA-10th ICBP-IUPAP Biophysics Congress Madrid, Spain, 20-24 July 2019.

Acknowledgements

I would like to thank my doctoral supervisor Professor Philip H. Jones for his patient support that guide me during this work and to give me the opportunity to work in his laboratory during a period of my PhD journey. I would also like to thank Professor Stan Zochowski who supported me in a difficult period half way through my studies. My thanks also to David Bronte Ciriza that set-up and trained the neural networks used in chapter 6. I would like to thank all my family and my girlfriend, Adriana, for her patience and endless support. Lastly, I would like to thank my cat, Marie, that kept me company during the darkest days of the pandemic.

Table of contents

List of figures

List of tables

Part I:

Introduction

1. General introduction: red blood cell

In this Chapter 1 I will describe the properties and function of red blood cell, and the interdependence of the two that is required for their normal operation.

Red blood cells (RBC) or erythrocytes are the most abundant cell present in most vertebrates' blood. In humans, mature and healthy RBCs are biconcave disks with a typical diameter of 6-8 μm, 2-3 μm thick in the periphery and 1-2 μm thick in the centre, Figure 1.1.[1] The cell's interior is delimited from the external world by a highly organised and very flexible cell membrane. Three different layers compose the cell's membrane in RBC: an outer layer, formed mainly of carbohydrates, known as glycocalyx, an intermediate lipidic bilayer, constituted mainly from cholesterol, phospholipids and membrane protein, and the membrane skeleton, a proteic structural scaffold in the interior of the cell, Figure 1.1.[2,3]

Mature RBCs lack the nucleus and the organelles found in most cells. The cell's inner portion, known as cytosol, is mainly filled by a concentrated protein solution known as haemoglobin. Thanks to the presence of iron atoms in a dedicated pocket in the protein three-dimensional structure, haemoglobin can bind O_2 or CO_2 with high efficiency for a

prolonged period of time. Haemoglobin is responsible for the characteristic red colour of the RBC.[2,4]

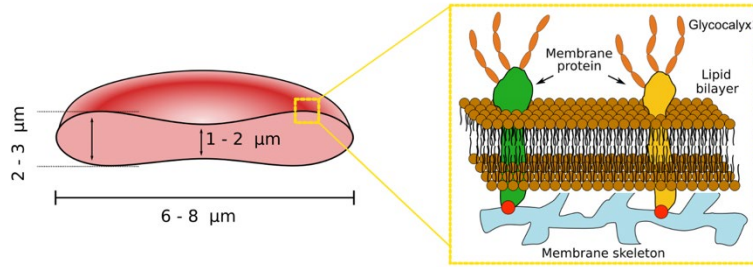

Figure 1.1. Morphology and cell membrane structure of a healthy red blood cell.

The RBCs' primary function is delivering oxygen to peripheral tissues and organs of the human body. The complex series of events that leads to oxygenation starts in the lungs, where O_2 diffuses within the RBC and binds to haemoglobin. Successively, the oxygenated RBCs travel within arteries until the peripheral tissues, where oxygen is released and diffuses into tissues/organs. After the release of oxygen, RBC takes up gaseous residues of the metabolic activity (i.e. CO_2), and transports them back to the lungs, where they are released and expelled from the organism, Figure 1.2. Then the cycle starts again.[5] A complete RBC's circulation takes about 60 seconds, and typically RBCs remains in the bloodstream for about 100–120 days before their components are recycled by specialised cells.[2]

During the cycle, RBCs must enter a system of small vessels where the gaseous components are exchanged. This system is called microcirculation. The microcirculation comprises arterioles with an inner diameter (i.d.) of ~100 µm, venules with i.d. ~150 µm, and capillaries i.d. ~5-8 µm, Figure 1.2.[6]

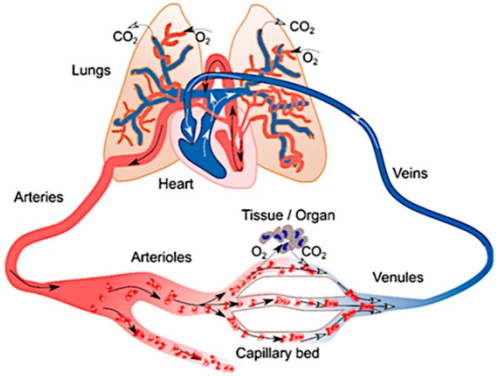

Figure 1.2. Cardiovascular system. The heart pumps oxygen-rich blood into the circulatory system. Blood flows through arteries and arterioles before reaching capillaries, supplying organs and tissues with oxygen and other nutrients. Successively, the oxygen-poor blood travels within venules and veins back to the heart, where it is pumped to the lungs, and the red blood cells are reloaded with oxygen. Adapted from ref. [5].

It appears immediately evident that RBCs must have a high degree of reversible flexibility and that any variation of their biomechanical properties could lead to severe dysfunctions in the microcirculation. In the most severe cases

of RBCs' alteration, the capillaries can be obstructed entirely, leading to tissues necrosis or organ damage and failure.[7]

The main origins of severe alteration of the RBC deformability can be genetic or a consequence of a pathogen's infection. Hereditary spherocytosis, elliptocytosis and sickle cell disease are examples of genetically inherited disorders that affect the shape and deformability of the RBCs, even if the molecular mechanisms that lead to the diseases are different.[7] On the contrary, malaria is a pathogenic disease that impairs the elastic properties of the erythrocytes.[8] The cause of malaria is the infection of microorganisms of the Plasmodium group, and mosquitoes are generally the primary transmission source.[9] Moreover, change in the RBC elasticity has also been correlated to a metabolic disorder such as diabetes,[10] and more recently also to SARS-CoV-2 viral infection, which leads to the Covid-19 disease.[11]

Optical tweezers (OTs) are a handy tool able to confine and manipulate single micron-sized objects thanks to a tightly focused laser beam. During the last two decades, OTs have been demonstrated to be an effective technique to investigate, sense, and screen the biomechanical properties of healthy and unhealthy RBCs, as well as pathogens infection.[12]

Now that we discussed the function, the morphology and some of the important biophysical properties that are required for the correct operation of the RBCs, we will look in more detail into the mechanism behind optical trapping that will underpin the work in this thesis.

1.1. Bibliography:

[1] E. Evans, Y. C. Fung, *Microvasc. Res.* **1972**, *4*, 335.

[2] S. De Oliveira, C. Saldanha, *Clin. Hemorheol. Microcirc.* **2010**, *44*, 63.

[3] A. Elgsaeter, B. T. Stokke, A. Mikkelsen, D. Branton, *Science (80-.).* **1986**, *234*, 1217.

[4] A. N. Schechter, *Blood* **2008**, *112*, 3927.

[5] D. Huber, A. Oskooei, X. Casadevall Solvas, Andrew Demello, G. V. Kaigala, *Chem. Rev.* **2018**, *118*, 2042.

[6] A. S. Popel, P. C. Johnson, *Annu. Rev. Fluid Mech.* **2005**, *37*, 43.

[7] M. Diez-Silva, M. Dao, J. Han, C. T. Lim, S. Suresh, *MRS Bull.* **2010**, *35*, 382.

[8] J. M. A. Mauritz, A. Esposito, T. Tiffert, J. N. Skepper, A. Warley, Y. Z. Yoon, P. Cicuta, V. L. Lew, J. R. Guck, C. F. Kaminski, *Med. Biol. Eng. Comput.* **2010**, *48*, 1055.

[9] E. A. Ashley, A. Pyae Phyo, C. J. Woodrow, *Lancet* **2018**, *391*, 1608.

[10] R. Agrawal, T. Smart, J. Nobre-Cardoso, C. Richards, R. Bhatnagar, A. Tufail, D. Shima, P. H. Jones, C. Pavesio, *Sci. Rep.* **2016**, *6*, 1.

[11] M. Kubánková, B. Hohberger, J. Hoffmanns, J. Fürst, M. Herrmann, J. Guck, M. Kräter, *bioRxiv* **2021**, *2019*,

2021.02.12.429482.

[12] R. Zhu, T. Avsievich, A. Popov, I. Meglinski, *Cells* **2020**, *9*, 545.

2. BACKGROUND AND THEORY

In this chapter, I will introduce the history that bring to the development of optical tweezer before to introduce the underlying physics that is required in the following of the thesis.

2.1. A brief history of optical tweezers

The first speculation that light can exert mechanical forces on particles dates back to the 17th century when Kepler observed that the comet tails always point away from the Sun. He attributed this phenomenon to a pressure exerted by the sunlight on the matter of the comet's tail.[1] Such an assumption entered modern science when Maxwell and Bartoli described the radiation pressure as a consequence of the electromagnetic theory and the second law of thermodynamics.[2,3] The first direct experimental observation of radiation pressure was made only ca. 30 years after the first theoretical description. Independently of each other, Pyotr Lebedev and Nichols and Hull evaluated the radiation pressure using a torsion radiometer.[4,5] However, to generate forces able to overcome gravitational or frictional forces are needed light sources with considerable intensity in most circumstances. For this reason, the phenomenon of radiation pressure seemed destined to remain confined to be

a novelty in physics rather than to have any interesting technological application.

In 1970, Arthur Ashkin realised that, even though the forces resulting from radiation pressure are small, so are the forces required to move small particles (microparticles). Furthermore, the invention of the laser in 1960 had provided a light source of sufficiently high brightness to make effects of radiation pressure more easily observable. In his first experiment, Ashkin could three-dimensionally confine a polystyrene microparticle using two counter-propagating and slightly divergent beams.[6] Soon after, in 1986, Ashkin and his collaborators demonstrated the possibility to confine microparticles by a single tightly focused laser beam, and the optical tweezers appeared on the scene.[7]

2.2. Optical forces and optical tweezers

Traditionally, optical forces are understood within approximations based on limiting size regimes based on the size parameter, ξ:[8]

$$\xi = 2\pi a n_m / \lambda_0$$

where a is the characteristic size of the object (i.e. the radius of the sphere), n_m is the refractive of the surrounding

medium, and λ_0 is the wavelength of the incident light in vacuum.

In the limit of $\xi \ll 1$ (i.e. particle much smaller than the wavelength), the calculations are based on the dipole approximation. In the dipole approximation, the optical forces are calculated as a consequence of the interaction of the incoming electromagnetic wave with the small dipole induced by the electromagnetic field approximating the trapped object. If the object's typical size is comparable to the optical wavelength, the intermediate regime ($\xi \approx 1$), a wave-optical approach is necessary for calculating the optical forces, and the Lorenz–Mie theory can be exploited to obtain accurate calculations for spherical particles of essentially any size and refractive index. However, the situation becomes more complex for non-spherical particles, e.g. elongated particles, optically anisotropic particles, and inhomogeneous particles. At the other limit of the limiting size regimes ($\xi \gg 1$) there is the geometrical optics approximation (GO).[8–10]

GO is well suited for biological samples, particularly for cells that show diameter ≥ 5 - 10 μm. In experiments with living cells, the photodamage of the light beam must be minimised, usually selecting light sources in the first or second biological window, a region of the electromagnetic spectrum with the lowest water absorption, assures a consistent decrement in the sample's photodamaging. For

biological samples, this happens for wavelengths around 0.850 μm and 1.064 μm.[11] These wavelengths are considerably smaller than the typical sizes of cellular samples, and thus the GO can be generally applied to a good level of approximation.

2.2.1. Optical forces and torques in geometrical optics approximation

In GO, an optical beam can be decomposed in a bundle of light rays provided with appropriate direction intensity and polarisation. Each light ray travels in straight lines within homogenous media. From a quantum mechanical point of view, electromagnetic radiation (light rays in GO) can be seen as particles rather than waves. These particles are known as photons. Each photon, with a wavelength λ_0 carries an energy $E_{ph} = hc/\lambda_0$ where h is the Plank's constant and c is the speed of light in vacuum. The momentum of each photon is given by:[10]

$$\boldsymbol{p} = \frac{h}{\lambda_0}\hat{\boldsymbol{\imath}} \qquad 2.1$$

where $\hat{\boldsymbol{\imath}}$ is the direction of propagation of the light ray.[10] Therefore, an optical ray ($\boldsymbol{r}$) of total power (P) carries $N = P/E_{ph}$ photons per second at a fixed point.

When a light ray travelling in a medium with a refractive index (RI) n_1, hits an object with RI = n_2 at an angle θ_i in respect to the line normal to the surface at the point of incidence, part of it is reflected at an angle $\theta_r = \theta_i$, and part of it is transmitted in a direction defined by Snell's law ($n_1 \sin\theta_i = n_2 \sin\theta_t$), Figure 2.1-a. In non-absorbing media, as a consequence of the conservation of energy, the incoming power (P_i) must be equal to the sum of the reflected (P_r) and the transmitted (P_t) power ($P_i = P_r + P_t$). The repartition of the power between the transmitted and the reflected rays is calculated according to Fresnel's reflection and transmission coefficients, for the s (R_s) and p (R_p) polarised light:[10]

$$R_s = \left|\frac{n_1 \cos\theta_i - n_2 \cos\theta_t}{n_1 \cos\theta_i + n_2 \cos\theta_t}\right|^2 ; R_p = \left|\frac{n_1 \cos\theta_t - n_2 \cos\theta_i}{n_1 \cos\theta_t + n_2 \cos\theta_i}\right|^2 \quad 2.2$$

where θ_i and θ_t are the angle between the direction of propagation of the incident and refracted ray with the normal to the surface at the incidence point, respectively. From this follows that the transmission coefficients (T) for the s-polarized light is $T_s = 1 - R_s$, and for the p-polarized light is $T_p = 1 - R_p$. For circularly polarised or unpolarised light, R and T are treated as an equal mix of the two polarisations, and the total reflection and transmission coefficients are $R = (R_s + R_p)/2$ and $T = (T_p + T_s)/2$.[10]

Thus, the optical forces generated by a stream of photons on the surface can be calculated as the rate of change of momentum between the incident, reflected and transmitted ray:[10]

$$\boldsymbol{F}_{ray} = \frac{n_1 P_i}{c}\hat{\boldsymbol{r}}_i - \frac{n_1 P_r}{c}\hat{\boldsymbol{r}}_r - \frac{n_2 P_t}{c}\hat{\boldsymbol{r}}_t \qquad 2.2$$

where n_1 and n_2 are defined previously, P_i, P_r and P_t are the power of the incident, reflected and transmitted ray respectively, *c* is the speed of light in vacuum and $\hat{\boldsymbol{r}}_i$, $\hat{\boldsymbol{r}}_r$ and $\hat{\boldsymbol{r}}_t$ are the direction of the incident, reflected and transmitted light ray. The first term on the right-hand side of eq. 2.2 represents the rate at which the momentum is incident on the surface, the second two are the rate at which it leaves the surface after reflection and transmission respectively. This difference is the total force exerted by a ray on a given surface.

However, if the light rays hit a closed surface (*e.g.* a spherical particle), the transmitted light ray at the first surface becomes the incident ray at the rear surface where it is again partially reflected and partially transmitted, Figure 2.1-b. The reflected ray at rear surface continues to be incident on the surface with decreased amplitude. Therefore, the total force exerted by the ray on a closed surface must account for this infinite reflection/refraction:[10]

$$\boldsymbol{F}_{ray} = \frac{n_1 P_i}{c}\hat{\boldsymbol{r}}_i - \frac{n_1 P_r}{c}\hat{\boldsymbol{r}}_r - \sum_{n=1}^{+\infty} \frac{n_i P_{t,n}}{c}\hat{\boldsymbol{r}}_{i,n}. \qquad 2.3$$

In practice, the last in term on the right hand side of 2.3 is truncated after few terms since the total reflected power decreases considerably, especially for biological sample. Since $\boldsymbol{r}_i$, $\boldsymbol{r}_r$ and $\boldsymbol{r}_t$ are all contained in the plane of incidence, the components of $\boldsymbol{F}_{ray}$ are contained in the same plane. It is then possible to split $\boldsymbol{F}_{ray}$ into the optical scattering force ($\boldsymbol{F}_{ray,s}$), that pushes the particle in the direction of propagation of the light ray and into the optical gradient force ($\boldsymbol{F}_{ray,g}$) that acts into the direction transverse to the light ray axis.[10] Lastly, the total optical force due to a set of m light rays can be calculated as the sum of the contribution of each single light ray:[10]

$$\boldsymbol{F}_{GO} = \sum_m \boldsymbol{F}_{ray}^{(m)} = \sum_m \left[\frac{n_1 P_i^{(m)}}{c}\hat{\boldsymbol{r}}_i^{(m)} - \frac{n_1 P_r^{(m)}}{c}\hat{\boldsymbol{r}}_{r,0}^{(m)} - \sum_{n=1}^{+\infty} \frac{n_i P_{t,n}^{(m)}}{c}\hat{\boldsymbol{r}}_{t,n}^{(m)} \right]. \qquad 2.4$$

The total optical force ($\boldsymbol{F}_{GO}$) acts on the centre of mass of the particle.

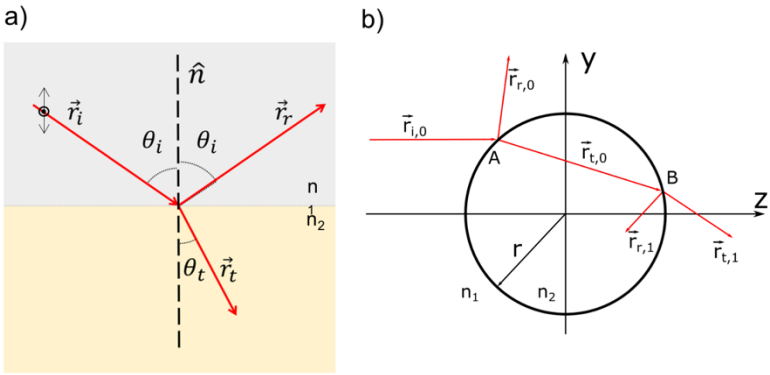

Figure 2.1. a) Schematisation of the law of reflection and Snell's Law The black arrows indicate the polarization. b) Interaction of a single light ray with a cross-section of a spherical particle.

However, significant torques can arise if the light rays interact with non-spherical particles, such as a cylinder, an ellipsoid, or (of particular relevance for this thesis) an RBC. The torque generated by a single light ray can be calculated as the difference of the angular momentum associated with the incoming ray and that of the outgoing rays:[10]

$$\boldsymbol{T}_{ray}^{(m)} = (\boldsymbol{P}_0 - \boldsymbol{C}) \times \frac{n_i P_i^{(m)}}{c} \hat{\boldsymbol{r}}_i^{(m)} - (\boldsymbol{P}_0 - \boldsymbol{C}) \times \frac{n_i P_r^{(m)}}{c} \hat{\boldsymbol{r}}_{r,0}^{(m)} - \sum_{n=1}^{+\infty} (\boldsymbol{P}_n - \boldsymbol{C}) \times \frac{n_i P_{t,n}^{(m)}}{c} \hat{\boldsymbol{r}}_{t,n}^{(m)} \qquad 2.5$$

where $\boldsymbol{C}$ is the centre of mass of the object, $\boldsymbol{P}_0$ is the incidence point of the incoming ray and $\boldsymbol{P}_n$ are the scattering points of the subsequently scattered rays.[10]

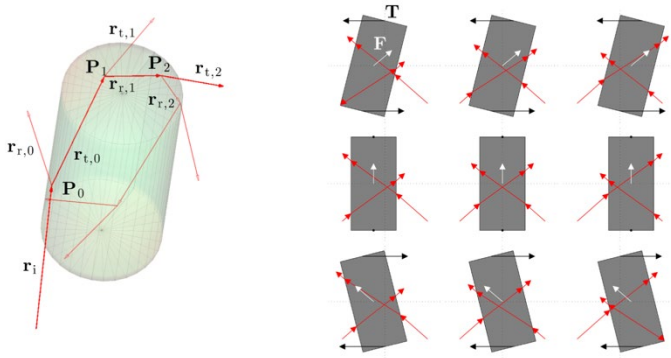

Figure 2.2. Optical torque acting on a non-spherical particle. On the left is shown the ray tracing of a light ray interacting with a cylindrical particle in three dimensions. On the right, the torques (black arrows) generated by a couple of light rays incident on a cylindrical particle are schematically depicted.*[10]*

Therefore, the total torque acting on the object is the sum of each contribution. Interestingly, the generated torques align the asymmetric particle along the axis of propagation of the light beam, as shown in Figure 2.2, so that it is rotationally confined as well as translationally confined, although the details of the orientation depend on the shape of the particle. Another characteristic example is given by ellipsoidal particles which tend to align their major axis along

the propagation direction of the light beam when optically trapped by an optical tweezers.

2.2.2. Optical trap

Optical tweezers (OT) is a technique able to three-dimensionally confine and manipulate microscopic objects through single or multiple laser beams. Figure 2.3 schematically depicts the trapping mechanism for a spherical particle with a refractive index higher than that of the surrounding medium. The laser beam's intensity distribution is considered Gaussian, and for simplicity, only two highly converging light rays originating at the fringe of the beam are shown.

If the spherical particle centre of mass (CM) does not lie on the optical axis, the two light rays strike the particle's surface asymmetrically. Consequently, the forces generated by the two light rays do not cancel out, and as a result of Newton's action-reaction law, the total optical force acting on the centre of mass of the particle pulls the object towards the optical axis, Figure 2.3-a. Simultaneously, the scattering force generated by the two light rays push the particle along the direction of propagation of the light beam. If the particle becomes consistently displaced in the axial direction, the two highly converging light rays generate a total optical force that pulls the object towards the region of higher intensity (i.e. the

beam focus), Figure 2.3-b. Importantly, the strong light convergence is essential in assuring a stable axial trapping. In fact, the absence of a strong light gradient in the direction of propagation of the light beam would prevent the emergence of a gradient force that counteracts the scattering component which would end up propelling the particle along the optical axis.

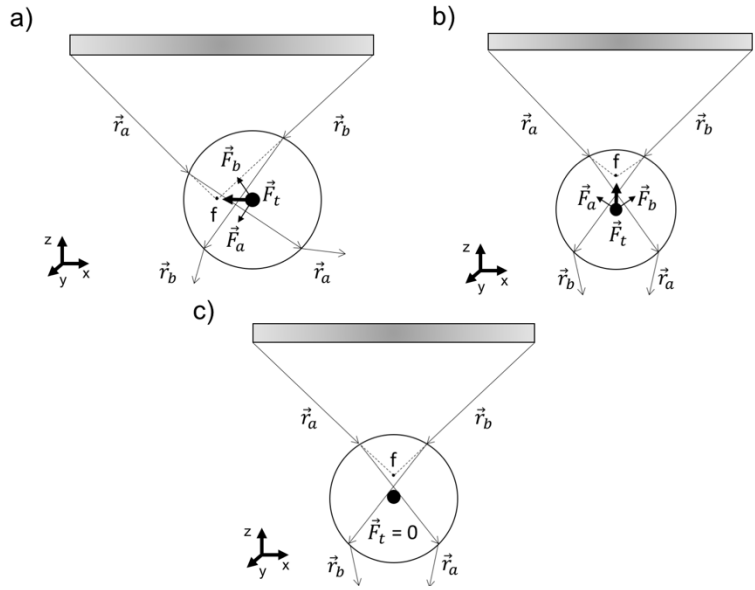

Figure 2.3. Schematic depiction of the working principle of optical tweezer: restoring forces generated by a couple of highly converging light rays in a direction transverse to the optical axis (a), on the optical axis (b), and particle at the point of equilibrium (c).

However, the axial restoring force is not able to counteract the scattering force completely, and the two forces cancel out

in a position slightly over the beam focus, Figure 2.3-c. Importantly, there would be no stable axial trapping in absence of highly converging light rays, and gravity or other forces would be needed to obtain stable axial trapping.[12]

The location where all the forces cancel out is called equilibrium position. Hence, for each particle displacements from the equilibrium position, or at least for small displacements from the equilibrium position, the particle is subjected to a restoring force that is proportional to the particle's displacement from the equilibrium position:[10]

$$\begin{cases} F_{GO,x} \approx -k_x\left(x - x_{eq}\right) \\ F_{GO,y} \approx -k_y\left(y - y_{eq}\right) \\ F_{GO,z} \approx -k_z\left(z - z_{eq}\right) \end{cases} \qquad 2.6$$

where $\mathrm{k_x}$, $\mathrm{k_y}$ and $\mathrm{k_z}$ are the spring constant or trap stiffness. The trap stiffnesses are used to characterise the trap's strength along the different cartesian directions.[10]

Non-spherical particles find an equilibrium configuration when the major axis is aligned with the optical axis. Similarly to the previous case, restoring torques are present for particles' rotation around each of the Cartesian components (x, y, z, respectively α, β and γ) which can be characterised by the rotational trapping stiffnesses:[10]

$$\begin{cases} T_{GO,x} \approx -k_{\alpha}(\alpha - \alpha_{eq}) \\ T_{GO,y} \approx -k_{\beta}(\beta - \beta_{eq}) \\ T_{GO,z} \approx -k_{\gamma}(\gamma - \gamma_{eq}) \end{cases} \qquad 2.7$$

2.2.3. Particle dynamics

Colloidal particles suspended within a fluid constantly change their position because of the thermal agitation of the surrounding molecules. This motion is known as *Brownian Motion* (BM) named after the botanist Robert Brown who first described this erratic particles' movement.[13] BM is the opponent to the confining forces of optical tweezers. Even if OT can decrease the amplitude of this motion, BM cannot be totally eliminated, even at thermal equilibrium. For this reason, in this section, I introduce the mathematical framework to simulate the motion of an optically trapped spherical colloid.

In principle, it is possible to write down and solve the equation of motion for every molecule of the fluid to calculate the trajectory of the larger colloid. However, this is a prohibitive task given the huge number of molecules of fluids involved in real situations.[14] Conversely, it is possible to reduce the number of effective degrees of freedom by describing the stochastic trajectory of a single particle with differential equations to which a stochastic force is added to

account for the interaction with the molecules of the surrounding fluid.[15]

2.2.3.1. Langevin equation

Brownian particles are subjected to Newton's second law of motion, which states that the total force acting on an object is equal to the mass of the object times its acceleration:

$$\mathbf{F_{tot}} = \mathrm{m}\dot{\mathbf{v}}(\mathrm{t}). \qquad 2.8$$

If we assume the mass of the particle to be unity, the equation of motion for a particle in a viscous fluid can be written as:

$$\dot{\mathbf{v}}(\mathrm{t}) = -\gamma\mathbf{v}(\mathrm{t}) + \boldsymbol{\chi}(\mathrm{t}) \qquad 2.9$$

where γ is the particle friction coefficient, and for a spherical particle with radius a, moving in a fluid of viscosity η, is defined by Stokes' law:

$$\gamma = 6\pi\eta\mathrm{a}. \qquad 2.10$$

The term $\boldsymbol{\chi}(t)$ is a random force that accounts for the particles' collision with the surrounding molecules of fluid and has the following properties:[16]

1. The mean of $\boldsymbol{\chi}(t)$ vanishes:

$$\langle \boldsymbol{\chi}(t) \rangle = 0; \qquad 2.11$$

2. It is uncorrelated with the particle's position:

$$\langle \boldsymbol{\chi}(t)\mathbf{r}(t) \rangle = 0; \qquad 2.12$$

3. $\boldsymbol{\chi}(t)$ is caused by the collision with the molecules of the surrounding fluids and varies rapidly. This is expressed by postulating for its autocorrelation function:

$$\langle \boldsymbol{\chi}(t_1)\boldsymbol{\chi}(t_2) \rangle = \Gamma\delta(t_1 - t_2) \qquad 2.13$$

where Γ is a constant (see next paragraph), and δ is the Dirac delta function with the following properties:

$$\delta(t_1 - t_2) = \begin{cases} \infty, t_1 = t_2 \\ 0, t_1 \neq t_2 \end{cases} \qquad 2.14$$

The basic idea is that each collision is instantaneous and that successive collisions are uncorrelated. Equation 2.9 is known as the Langevin equation.[15,16]

2.2.3.2. Fluctuation-dissipation theorem

It is impossible to know the time-dependence of the stochastic force term $\boldsymbol{\chi}(\mathrm{t})$, so it is assumed as a stochastic variable with some plausible distribution. It is possible to find a solution to eq. 2.9 in terms of $\boldsymbol{\chi}(\mathrm{t})$, allowing us to identify the mean and the variance of the velocity and to obtain a relationship that defines the magnitude of the fluctuating term. Eq. 2.9 can be solved with the use of integration factor $\mathrm{e}^{\gamma \mathrm{t}}$:

$$\mathbf{v}(\mathrm{t}) = \mathbf{v}_0 \mathrm{e}^{-\gamma \mathrm{t}} + \int_0^{\mathrm{t}} \mathrm{d}s \mathrm{e}^{-\gamma(\mathrm{t}-\mathrm{s})} \boldsymbol{\chi}(\mathrm{s}) \qquad 2.14$$

where $\mathbf{v}_0$ is the velocity at $\mathrm{t} = 0$. Taking the average of the velocity over an ensemble of trajectories and employing eq. 2.11, we find that:

$$\langle \mathbf{v}(\mathrm{t}) \rangle = \mathbf{v}_0 \mathrm{e}^{-\gamma \mathrm{t}} \qquad 2.15$$

which indicates that the average velocity of a Brownian particle decays exponentially with a characteristic time scale

$1/\gamma$. This time scale $(1/\gamma)$ is known as momentum relaxation time and is typically in the orders of tens of nanoseconds. We also take the variance of the velocity:

$$\langle \mathbf{v}^2(t) \rangle = e^{-2\gamma t}\mathbf{v}_0^2 + \int_0^t \int_0^t ds_1 ds_2 e^{-\gamma(t-s_1)} e^{-\gamma(t-s_2)} \langle \boldsymbol{\chi}(s_1)\boldsymbol{\chi}(s_2) \rangle . \quad 2.16$$

Given eq. 2.13 and the properties of δ, the only contribution to the integral in eq. 2.16 is when $s_1 = s_2$. Thus:

$$\langle \mathbf{v}^2(t) \rangle = e^{-2\gamma t}\mathbf{v}_0^2 + \Gamma \int_0^t ds_1 e^{-2\gamma(t-s_1)}$$

$$= e^{-2\gamma t}\mathbf{v}_0^2 + \frac{\Gamma}{2\gamma}(1 - e^{-2\gamma t}). \quad 2.17$$

at long times, $t \to \infty$, by the equipartition theorem, the mean squared velocity has the known thermal value $k_b T$, where k_b is the Boltzmann constant and T is the absolute temperature, and we see that:

$$\langle \mathbf{v}^2(\infty) \rangle = \frac{\Gamma}{2\gamma} = k_b T. \quad 2.18$$

We have obtained the constant Γ that describes the size of the fluctuation term in eq. 2.13:

$$\Gamma = 2\gamma k_b T. \qquad 2.19$$

The size of the fluctuations is dictated only by the temperature and the damping coefficient γ. Eq. 2.19 is an expression of the fluctuation-dissipation theorem, which relates the size of the fluctuation to the rate of dissipation (γ). Eq. 2.13 may now be written as:[16]

$$\langle \boldsymbol{\chi}(t_1)\boldsymbol{\chi}(t_2)\rangle = 2\gamma k_b T\delta(t_1 - t_2). \qquad 2.20$$

As we will see later in the text, the intensity of the noise fluctuation can be used to extract important trap information (e.g. trap constants).

2.2.3.3. Overdamped Langevin equation

Until now, we have considered a Langevin equation that describes the free diffusion of a Brownian particle. We now include an additional force term to account for the confining effect of an optical trapping potential, $U(\mathbf{x})$:

$$m\dot{\mathbf{v}}(t) = -\gamma\mathbf{v}(t) + \boldsymbol{\chi}(t) - \frac{dU(\mathbf{x})}{dx}. \qquad 2.21$$

The numerical experiments described in this thesis takes place in a *low-Reynolds-number* regime. The Reynolds

number, $\mathrm{Re} = \mathrm{av}\rho/\eta$ (where ρ is the density of the fluid and η the viscosity), describes the ratio of inertial and viscous forces acting on a particle moving through a fluid. In the low-Reynolds number regime ($\mathrm{Re} \leq 1$), viscosity dominates over inertia, which means that the inertial term in eq. 2.21 ($-\mathrm{m}\dot{\mathbf{v}}(\mathrm{t})$) is negligible and may be omitted:

$$0 = -\gamma \mathbf{v}(\mathrm{t}) + \boldsymbol{\chi}(\mathrm{t}) - \frac{\mathrm{dU}(\mathbf{x})}{\mathrm{dx}}. \qquad 2.22$$

The force produced by the optical tweezers behaves like the force produced by a Hookean spring (eq. 2.6), and thus the potential has the form $\mathrm{U}(\mathbf{x}) = \frac{1}{2}\mathrm{k}\mathbf{x}^2$. Eq. 2.22 in terms of the positions, becomes:

$$\gamma \dot{\mathbf{x}}(\mathrm{t}) = \boldsymbol{\chi}(\mathrm{t}) - \mathrm{k}\mathbf{x}(\mathrm{t}) \qquad 2.23$$

where k is the trap stiffness and $\mathbf{x}(\mathrm{t})$ is the particle's position relative to the minimum of the Harmonic potential. The solution of eq. 2.23, with initial condition $\mathbf{x}(0) = \mathbf{x}'$, is:

$$\boldsymbol{x}(t) = \boldsymbol{x}' e^{\frac{-t}{\tau}} + \frac{1}{\gamma}\int dt' e^{\frac{(t-t')}{\tau}} \boldsymbol{\chi}(t). \qquad 2.24$$

Eq. 2.24 is an exponential decay towards equilibrium. This tells us that the system is an overdamped oscillator with a decay constant $\omega_{OT} = \gamma/k$, and this is the position relaxation

time, which is a much longer timescale (milliseconds) than the momentum relaxation time.[14,17]

2.2.3.4. Position auto-correlation function

The autocorrelation function (ACF) is a valuable tool for the characterisation of a harmonic trapping potential. The ACF correlates a signal with itself as a function of lag-time. The ACF describes how similar a particle's position is to some initial position. At short lag-time, the particle does not move far from its initial position, so it will be highly correlated. At long lag-time, the particle is unlikely to have remained close to its initial location and thus becomes uncorrelated with the initial position. The ACF described the temporal transition from correlation to non-correlation. This can be thought of as the time taken by a particle to 'forget' its original position. The position ACF is defined as:[14,18]

$$C_{xx}(t) = \langle \boldsymbol{x}(0) \cdot \boldsymbol{x}(t) \rangle. \qquad 2.25$$

If we take the time derivative of the auto-correlation:

$$\dot{C}_{xx}(t) = \langle \boldsymbol{x}(0) \cdot \dot{\boldsymbol{x}}(t) \rangle \qquad 2.26$$

and substitute for the time-derivative term in eq. 2.23, we find that:

$$\dot{C}_{xx}(t) = \frac{1}{\gamma}\langle \boldsymbol{x}(0) \cdot \big(\boldsymbol{\chi}(\mathrm{t}) - \mathrm{k}\mathbf{x}(\mathrm{t})\big)\rangle. \qquad 2.27$$

Now, because $\boldsymbol{x}(t)$ and $\boldsymbol{\chi}(\mathrm{t})$ are uncorrelated at all times other than $\mathrm{t} = 0$, the term $\langle \mathrm{x}(0)\boldsymbol{\chi}(\mathrm{t})\rangle$ is zero and:

$$\dot{C}_{xx}(t) = -\frac{k}{\gamma}\langle \boldsymbol{x}(0) \cdot \mathbf{x}(\mathrm{t})\rangle = -\frac{k}{\gamma}C_{xx} \qquad 2.28$$

which has the simple solution:

$$\mathrm{C_{xx}(t)} = \mathrm{C_{xx}(0)e^{-\frac{k}{\gamma}t}}. \qquad 2.29$$

An exponential decay describes the transition from the correlation to non-correlation with a characteristic frequency that depends on the trap spring constant and the drag coefficient ($\omega_{\mathrm{OT}} = \gamma/\mathrm{k}$). At zero lag-time, the energy stored in the trap is:

$$\mathrm{U} = \frac{\mathrm{k}}{2}\langle \mathrm{x}^2(0)\rangle = \frac{\mathrm{k}}{2}\mathrm{C_{xx}}(0) \qquad 2.30$$

we can equate this to $\mathrm{k_bT}/2$ via the equipartition theorem, allowing us to write:

$$\mathrm{C_{xx}(t)} = \frac{\mathrm{k_bT}}{\mathrm{k}}\mathrm{e^{-\frac{k}{\gamma}t}}. \qquad 2.31$$

Two assumptions have been made to arrive at this equality. Firstly, $\mathrm{U}(\mathbf{x})$ has been approximated as harmonic. Accordingly, we assume a linear response of the restoring force for small particle's displacements from its equilibrium. Secondly, the force field has been approximated as conservative.

2.2.3.5. Brownian dynamics simulations

The Langevin equation can be solved numerically to obtain the time evolution of the position of the Brownian particle. This offers a practical methodology for simulating experimental particle's trajectories. The basic idea is to estimate the continuous-time solution, $\mathbf{x}(\mathrm{t})$, with a discrete-time series, $\mathrm{x_i}$. The discrete terms of the time sequence are obtained by recursively solving the Langevin equation at finite time steps, $t_i = i\Delta t$. For determined values of Δt, the discrete terms (i.e. x_i) are good approximations of continuous-time solution $\boldsymbol{x}(t)$, as it will be explained shortly after in the text.

The overdamped Langevin equation (eq. 2.23) can be re-written as:[14]

$$\dot{\boldsymbol{x}}(t) = -\frac{k}{\gamma}\boldsymbol{x}(t) + \sqrt{2\Gamma}W(t) \qquad 2.32$$

where $\mathrm{W}(\mathrm{t})$ is a white noise with the following properties:

1. $\langle W(t) \rangle = 0$ for each t;
2. $\langle W(t)^2 \rangle = 1$ for each t;
3. $W(t_1)$ and $W(t_2)$ are independent of each other for $t_1 \neq t_2$.

To write the finite-difference equation, the particle position (i.e. $\boldsymbol{x}(t)$) and its time derivative have to be replaced in eq. 2.32 with the following:

$$\boldsymbol{x}(t) \rightarrow \boldsymbol{x}_i; \qquad \dot{\boldsymbol{x}}(t) \rightarrow \frac{\boldsymbol{x}_i - \boldsymbol{x}_{i-1}}{\Delta t}. \qquad 2.33$$

The noise is included in the finite-difference scheme as a sequence of random numbers that mimic the properties of $\mathrm{W(t)}$:

1. $\mathrm{W_i}$ must be a series of random numbers with zero mean;
2. $\mathrm{W_i}$ must satisfy the condition that:

$$\frac{\langle (\mathrm{W_i} \Delta \mathrm{t})^2 \rangle}{\Delta \mathrm{t}} = 1$$

   thus ensuring that the variance per unit time is unitary;
3. $\mathrm{W_i}$ and $\mathrm{W_j}$ must be independent for $\mathrm{i} \neq \mathrm{j}$.

Therefore, it will be used a sequence of random numbers with zero mean and variance $1/\Delta t$. Practically, this can be obtained by generating a sequence w_I of Gaussian-distributed random numbers with zero mean and unitary variance, and then rescale it to get the series $W_i = w_i/\sqrt{\Delta t}$ with variance $1/\Delta t$.[14] Therefore, eq. 2.32 becomes:

$$\mathbf{x}_i = \mathbf{x}_{i-1} - \frac{k}{\gamma}\mathbf{x}_{i-1}\Delta t + \sqrt{2\Gamma\Delta t}\, w_i \qquad 2.34$$

where the second term on the right-hand side is the deterministic contribution to the particle's motion (i.e. optical trap), and the third term is the diffusive term.

In performing the numerical simulation, Δt should be chosen to be significantly smaller than the relaxation time of the trapped particle, $\omega_{OT} = \gamma/k$. In the case that $\Delta t \gtrsim \omega$, the simulation will show unphysical behaviour, and the particle may escape the trap or appear to oscillate. Moreover, Δt should be considerably longer than the momentum relaxation time, $\omega_m = \frac{m}{\gamma}$. If $\Delta t \lesssim \omega_m$, the ballistic motion of the particle becomes significant, and the over-damped Langevin equation cannot describe the dynamics of the particle.[14,19]

Figure 2.4-a shows the trajectories simulated in presence (red trajectory) and absence (blue trajectory) of a confining potential acting on a spherical particle. Here it can be seen the effect of the confining potential force of eq. 2.32.

In fact, a particle that is not subjected to restoring forces is free to diffuse away from the original position with an erratic motion typical of Brownian particles. On the contrary, an optically trapped particle explores an ellipsoidal volume in the vicinity of the objective focus.

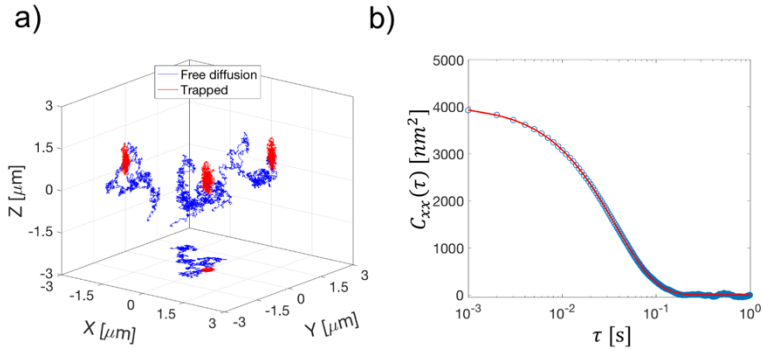

Figure 2.4. a) Brownian dynamics simulation of an optically trapped particle and a freely diffusive particle and autocorrelation analysis of the trapped particle (b)

The asymmetry between the volume explored in the x- and y-direction compared to the z-direction is a consequence of the scattering force acting on the dielectric colloid. As mentioned before, the autocorrelation analysis can be used to extract the stiffness of the optical trap. In Figure 2.4-b, the spatial autocorrelation function (only along the x-direction) can be fitted with an equation of the form of eq. 2.31. In this example, the particle has a radius a = 2 μm, the system's temperature is 293 K, the viscosity of the water

(η) is 0.001 Pa·s. Therefore, the friction coefficient (γ) can be calculated via Stokes' equation ($\gamma = 6 \cdot \pi \cdot \eta \cdot a = 3.97 \times 10^{-8}$ kg·s^{-1}), and the trap stiffness obtained by the parameters of the fit. The trap stiffness is k_x = 1.011 pN·μm-1 in very good agreement with the k_x used for the simulation (k_x= 1 pN·μm^{-1}).

In this Chapter I introduced the underlying physics that is require in this thesis for the study of particles trapped in optical tweezer, namely the mechanism by which force is exerted in the geometrical optics approximation, and the Brownian motion of the particles as well the methodology to determine the trap stiffness from the Brownian motion.

2.3. Bibliography

[1] J. Kepler, *De Cometis Libelli Tres*; Augsburg, 1619.

[2] A. Bortoli, *Nuovo Cim.* **1884**, *15*, 193.

[3] J. C. Maxwell, *A Treatise on Electricity and Magnetism*; 1873.

[4] P. N. Lebedev, *Ann. Phys.* **1901**, *6*, 433.

[5] E. F. Nichols, G. Hull, *Astrophys. J.* **1903**, *17*, 315.

[6] A. Ashkin, *Phys. Rev. Lett.* **1970**, *24*, 156.

[7] A. Ashkin, J. M. Dziedzic, J. E. Bjorkholm, S. Chu, *Opt. Lett.* **1986**, *11*, 196.

[8] G. Pesce, P. H. Jones, O. M. Maragò, G. Volpe, *Optical tweezers: theory and practice*; Springer Berlin Heidelberg, 2020; Vol. 135.

[9] O. M. Maragò, P. H. Jones, P. G. Gucciardi, G. Volpe, A. C. Ferrari, *Nat. Nanotechnol.* **2013**, *8*, 807.

[10] P. H. Jones, O. M. Maragò, G. Volpe, In *Optical Tweezers Principles and applications*; Cambridge University Press: Cambridge, 2015; pp. 19–41.

[11] A. Blázquez-Castro, *Micromachines* **2019**, *10*, 1.

[12] A. Ashkin, *Biophys. J.* **1992**, *61*, 569.

[13] R. Brown, *Philos. Mag. Ann. Philos.* **1829**, *4(21)*, 161.

[14] P. H. Jones, O. M. Maragò, G. Volpe, In *Optical tweezers principles and applications*; 2015; pp. 188–218.

[15] D. S. Lemons, A. Gythiel, *Am. J. Phys.* **1997**, *65*, 1079.

[16] N. G. Van Kampen, *Stochastic Processes in Physics and Chemistry*; iv.; Elsevier, 2003.

[17] L. S. Ornstein, G. E. Uhlenbeck, *Phys. Rev.* **1930**, *36*, 823.

[18] H. Risken, *The Fokker-Planck Equation*; Springer US, 1996.

[19] G. Volpe, G. Volpe, *Am. J. Phys.* **2013**, *81*, 224.

Part II:

Results

3. THEORETICAL INVESTIGATION OF OPTICAL TRAPPING OF BICONCAVE RED BLOOD CELL WITH SINGLE- AND MULTI-BEAMS OPTICAL TWEEZER

In this chapter I present the result regarding the theoretical investigation of optical trapping of healthy biconcave red blood cell in the geometrical optics approximation. Initially, I introduce the ray tracing approach used to perform the geometrical optics calculations that are used extensively throughout the thesis. Successively, I propose the methodology used to characterize the optical trapping of a healthy erythrocyte in the simple case of a single-beam optical tweezer. Lastly, I investigate the optical trapping of healthy red blood cell with a double-, triple- and four-beam optical tweezers.

3.1. Introduction

The application of optical tweezers in red blood cell (RBC) studies has seen a rapid growth in the last two decades.[1] Two main approaches to optically trap RBC have been adopted so far. The first contemplates the use of

handles, such as polystyrene or silica microsphere, which are allowed to adhere to the cell membrane and are then used to trap, manipulate, or stretch the cell.[1,2] In the second mechanism, the cell is confined and manipulated by a single or multiple focused laser beams which illuminate the cell directly.[1,3] The latter is referred to as direct trapping henceforth. Since the direct trapping has been previously used in our laboratory to optically trap erythrocytes,[4,5] in the remainder of this thesis, only the direct trapping of RBC will be considered.

A single-beam optical tweezer (SBOT) is the most straightforward option for the direct trapping of a RBC. In a representative experiment, the plane of the RBC is initially transverse to the propagating light beam, from now on referred to as 'flat' configuration, Figure 3.1-a. The optical force ‘draws’ the RBC into the beam(s) while optical torques rotates the cell, such that its plane becomes oriented parallel to the optical axis, Figure 3.1-a and -b. This phenomenon is referred to as the RBC getting folded into an optical trap and this RBC configuration is referred to as 'folded' configuration henceforward.[1,6]

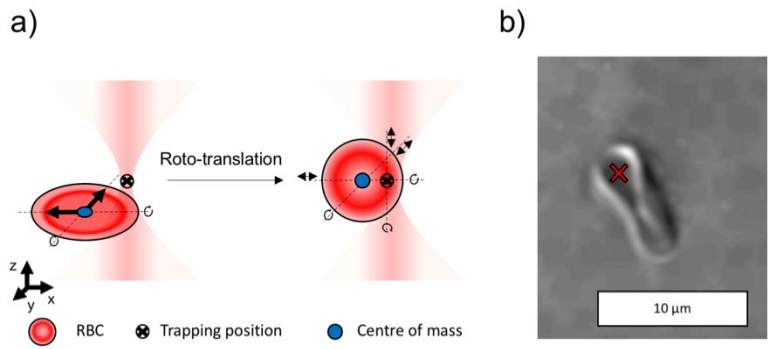

Figure 3.1. a) Schematic depiction of the equilibrium configuration of a biconcave erythrocyte trapped by a single-beam optical tweezer. b) Micrograph of an RBC trapped by a single-beam optical trap. The red cross indicates the approximate trap position. Image adapted from [3].

SBOT can be used for a variety of different analytical applications. For example, the single-beam set-up has been used to study the trapping dynamics of RBCs, whose shapes are slightly modified by the osmolarity of the cell suspension medium.[6] A more intriguing application of a single-beam set-up is given in [7]. In their research, Brandão and collaborators measured the elasticity and the viscosity of healthy and unhealthy RBCs. The authors used a SBOT to keep the RBC in the 'folded' configuration while a fluid with a defined velocity deforms the cell in the direction of flow.

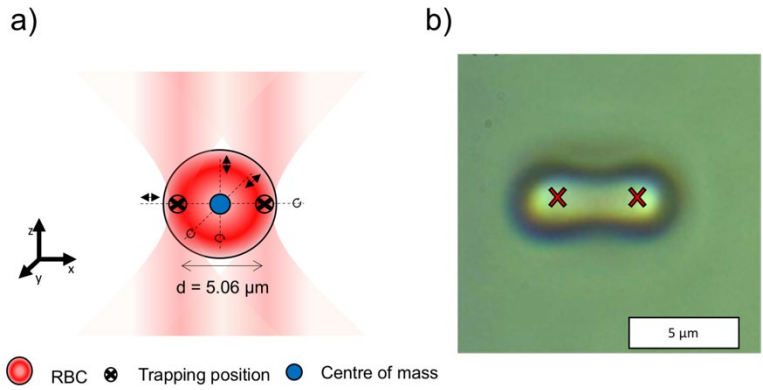

Figure 3.2. RBC trapping with a double-beam optical tweezer. a) Schematic depiction of an RBC in its equilibrium configuration. b) Experimental observation of an RBC optically trapped by a double-beam optical tweezer. The red crosses indicate the approximate trap position. Image adapted from [5].

An experimental configuration with increased complexity is given by a double-beam optical tweezer (DBOT). In DBOT, two beams are used to directly trap the RBC. Importantly, the beams' foci must be spaced to fall within the RBC's border, at least initially, Figure 3.2-a and -b.[5] DBOT has been used mainly to stretch the RBC along the line connecting the two beams' foci. For example, Liao *et al.* studied the transverse extent of an RBC stretch using a rapidly jumping beam between two points. After the cell gets trapped, by increasing the spacing between the points in which the beams jump, they could induce and measure the deformation of the RBC.[8] More recently, this methodology

(with two static beams) has also been used to measure and correlate the deformability of the RBC of patients affected by type 2 diabetes with diabetic retinopathy.[4]

Other applications of OT to RBC relies on the combination of spectroscopic techniques such as Raman spectroscopy with multi-beams optical tweezer, application often called Raman-Tweezers (RT). An elegant example of the use of RT to RBC studies was given by G. Rusciano *et al*.[9] In these experiments a four-beams optical tweezer (FBOT) was used to orient and maintain the cell in the 'flat' configuration, while a fifth laser beam with a different wavelength scanned the cell to excite the Raman mode of the biomolecule of interest, Figure 3.3-a and -b. With this set-up, the investigators were able to obtain 2D-maps of the distribution of the biomolecules within the cell. Interestingly, the researchers were able to cancel out the torques contribution due to each beam, which should induce the cell folding, so that the equilibrium configuration is for a RBC in its 'flat' configuration as shown in Figure 3.3-b.

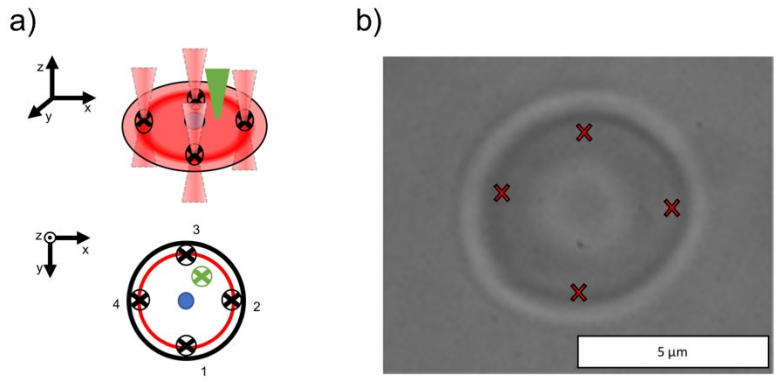

Figure 3.3. RBC trapping with a four-beam optical tweezer. a) Schematic depiction of an RBC in its equilibrium configuration. The green light beam indicates the beam used for Raman spectroscopy. b) Micrograph of an RBC optically trapped by a four-beam optical tweezer. The red crosses indicate the approximate trap position. Image adapted from [9].

Although numerous experiments demonstrated how it is possible to optically confine healthy RBCs and control the orientation by using a different number of laser beams, relatively little theoretical work has been performed to investigate the trapping mechanism necessary for these experiments and the cell stretching experiments described above. To the best of my knowledge, only one work explores the RBC equilibrium configuration in an optical trap theoretically.[10] Grover *et al.* investigated the final orientation of an RBC trapped by a counter-propagating beam trap. However, the trapping mechanism of a counter-propagating beam trap is fundamentally different from that of OT since it

relies on a balance of optical scattering forces for stability. A theoretical investigation of the mechanism of trapping is necessary to understand better how the intricate shape of the RBC (that is crucial for its function) affects the optical trapping via optical tweezers. Moreover, a methodology to calculate the optical forces and torques along with the trapping stiffnesses is vital for the experimentalists to optimize these parameters before performing real experiment on e.g. RBC deformability.

For these reasons, in the next sections I will introduce a method to calculate the optical forces generated by tightly focused beam/beams on a healthy RBC in the geometrical optics approximation (GO). The methodology is then applied to study the trapping mechanism of an RBC extensively.

3.2. Model

In my model a three-dimensional Cartesian co-ordinate system is considered. The light beams possess a Gaussian light intensity distribution and propagate along the $+\hat{\mathbf{z}}$. The wavelength of the light beam (1.064 μm) is selected to matches with the vast majority of experiments and to coincide with the light source present in our laboratory (Nd:YAG laser).[1,11]

To illustrate the mode of operation some plausible values have been chosen for the beam waist at the back

aperture of the objective (50 μm), objective numerical aperture (1.3), and the objective back aperture (9.78 μm). In this conditions the objective's back aperture is completely overfilled by the incoming beam, and the high light rays' convergence is assured. It must be stressed that these values can be completely tuned according to the particular conditions one wants to explore. However, the tuning of these values could results in slightly different trap constants and positions of equilibrium obtained via the numerical simulations. The power of the beam is always 5 mW. In multi-beam optical trap calculations, each beam has the properties just described.

The beams' power is kept in the mW range for two reasons. Firstly, high laser powers (>100 mW) can damage the cell significantly, and thus such conditions are unrealistic from an experimental point of view.[11] Secondly, as introduced previously in the text, the RBCs are elastic and can deform considerably under the effect of radiation pressure generated by a high power laser beam.[8,12]

According to experiments, the RBC is immersed in a water-based medium (refractive index $n_1 = 1.33$). The cell membrane is modelled as a single net line. The interior of the RBC is considered to be filled by a non-absorbing medium with isotropic physical properties. The refractive index of the

cell interior is $n_2 = 1.38$, and the cell's density is 1.11 g/cm^3.[13]

The RBC is in its healthy biconcave disk conformation and the parameters describing the RBC disk are those reported by Evans and collaborators.[14] A radius of 3.91 μm characterises the RBC, the central dimple has a thickness of 0.81 μm, while the thickest portion, located at 2.76 μm from the axis of symmetry, has a thickness of 2.52 μm. For the low optical powers used in the calculations the RBC is always considered to be non-deforming in response to radiation pressure.

For biological samples such as RBC, the fraction of power that is reflected after a scattering event is very low (< 0.001).[15] Therefore, only the first two scattering events are considered.

Considering a cell radius of a= 3.91 μm, the medium refractive index n_m = 1.33, a wavelength of the incoming beam λ_0 = 1.064 μm, we found that the size parameter $\zeta = (2\pi a n_m/\lambda_0) \approx 80$. In this conditions, the GO optics approximation is entirely fulfilled. Thus, the optical forces acting on the RBC can be calculated with GO. However, to calculate the ray traces, an appropriate mathematical description of the RBC is needed. In the next section, the mathematical model used to describe a red blood cell outline is discussed.

3.3. Mathematical description of a RBC

In chapter 1, I introduced the native structure of a healthy RBCs. Generally, the RBC shape is geometrically described as axially symmetric. The meridional cross-section is characterised by a radius (r), a minimum thickness (t_{min}), a maximum thickness (t_{max}), and the radius where the maximum thickness occurs (d). Several well-known and widely recognised models describing the biconcave shape of the RBC have been proposed, and an extensive overview of the available descriptions is given in the work proposed by Valchev and collaborators.[16] Here the authors provided a series of useful formulae that correlate the parameters describing the cell with the meridional cross-section. In Figure 3.4-a some of the available models describing the RBC are overimposed to the experimental data obtained by Evans *et al*., and reported as in Valchev's work.[14,16]

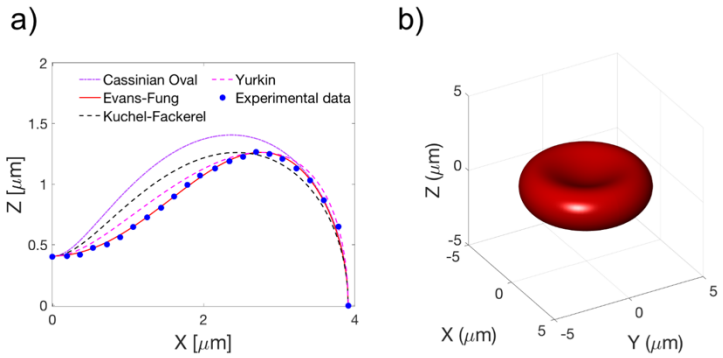

Figure 3.4. a) Different models used to describe the RBC cross-section are plotted and compared to the experimental values obtained by Evans et al., [14] and vastly discussed by Valchev et al.[16] Thanks to the symmetry of the RBC geometry, the values of the meridional cross-section are plotted only for the first quadrant. b) Three-dimensional rendering of the RBC geometry described by the Evans-Fung model.

Some of these models are relatively simple and describe the RBC meridional cross-section via biquadratic polynomials, such as the description based on Cassini's oval or that offered by Kuchel-Fackerell's model.[17,18] Even if these simple models can describe the rough outline, they fail to carefully represent the RBC's curvature of the central dimple, Figure 3.4-a. As we will see in more detail later, this portion of the RBC is vital in determining the optical forces acting on the cell, and therefore the stability of the optical trap.

An improved version of the RBC description has been proposed by Yurkin and co-workers.[19] Although a significant enhancement in the RBC description is obtained, the model still fails to precisely describe the central dimple, Figure 3.4-a. A significant improvement in the RBC's morphology description can be obtained using polynomials of degree higher than four as proposed in [14], Figure 3.4-a. According to the Evans-Fung model, the thickness (Z) of a section of the RBC reads:

$$Z(\rho) = \left[1 - \left(\frac{\rho}{r}\right)^2\right]^{\frac{1}{2}} \left[C_0 + C_2\left(\frac{\rho}{r}\right)^2 + C_4\left(\frac{\rho}{r}\right)^4\right] \qquad 3.1$$

where ρ is the radial distance from the axis of symmetry, r the cell radius and C_0, C_2 and C_4 are numerical values that can be related to the observable parameters that describe the cell morphology through the following equations:

$$C_0 = \frac{t_{min}}{2r}$$

$$C_2 = \frac{4r^2}{2d^2}\left[-4C_0 + \frac{t_{max}|5d^2 - 16r^2|}{(4r^2 - d^2)^{3/2}}\right] \qquad 3.2$$

$$C_4 = \frac{16r^2}{2d^4}\left[2C_0 + \frac{t_{max}(16r^2 - 3d^2)}{sgn(5d^2 - 16r^2)(16r^2 - d^2)^{\frac{3}{2}}}\right]$$

where t_{min}, t_{max} and d were defined previously and r is the RBC radius.[14,16] Figure 3.4-b shows the 3D rendering of the

RBC surface described by the Evans-Fung model. With an accurate description of the RBC outline, it is possible to ray trace the optical rays and calculate the optical forces due to each ray. Due to its better ability to describe the RBC outline, the model proposed by Evans-Fung will be used in the remainder of this thesis.

3.4. Ray tracing procedure for the RBC

In this section, the algorithm used to trace the trajectories of the optical rays impinging on the RBC is described. The methodology is based on standard ray tracing procedure,[20] and is incorporated in a new object and used in the well-known Optical Tweezer In Geometrical Optics (OTGO) software.[21]

During the ray-tracing procedure, two primary pieces of information must be geometrically extracted to describe the interaction between a light ray and the object: the intersection point between the ray and the object, and the unit normal vector at the point of intersection. Knowing these two quantities it is possible to obtain the angle of incidence of the light ray and describe the rays' path according to Snell's law and the law of reflection.

A light ray can be defined by its origin $\boldsymbol{o} = (o_x, o_y, o_z)$ and its ending point $\boldsymbol{e} = (e_x, e_y, e_z)$. An optical ray ($\boldsymbol{p}$) is a

straight line which can be modelled by its origin and the displacement vector $\boldsymbol{d} = \boldsymbol{e} - \boldsymbol{o} = (d_x, d_y, d_z)$, and a parameter $t \geq 0$. t defines the distance from the origin of the vector along the ray. In terms of the three Cartesian components, this can be written as:

$$\begin{cases} p_x = o_x + td_x \\ p_y = o_x + td_y \\ p_z = o_z + td_z \end{cases}; t \geq 0. \qquad 3.3$$

Thus, to find the intersection between the vector describing the light ray, and the object, p_x, p_y, and p_z must be replaced for x, y and z in the equation that describes the object. Transforming eq. 3.13.1 to Cartesian co-ordinates, and replacing x, y, z as just described, one obtains:

$$\left(\frac{p_z}{R}\right)^2 - \left(1 - \frac{\left(p_x^2 + p_y^2\right)}{r^2}\right) \left(C_0 + C_2\left(\frac{p_x^2 + p_y^2}{r^2}\right) + C_4\left(\frac{p_x^2 + p_y^2}{r^2}\right)^2\right)^2 = 0. \qquad 3.4$$

Therefore, eq. 3.4 must be solved for t. t is obtained via a numerical roots finder. If there are no real values for t, the ray does not intersect the object. If there are more than one real positive values for t, then the intersection point is the smallest. If there are only negative values, then the line describing the light ray intersects the object in a portion that does not describe the optical ray.

Figure 3.5-a and b illustrate the calculation of the intersection point between a light ray and the RBC surface calculated with the described methodology. Once the intersection point is obtained, the unit normal vector is calculated as the normalised gradient of the surface at the intersection point.

If the RBC is roto-translated into a configuration that does not coincide with standard position (centre of mass in (0,0,0) and not rotated, in the 'flat' configuration), it is possible to take the inverse transformation of the light ray, and then calculate the intersection between the transformed light ray and the RBC in its standard position.

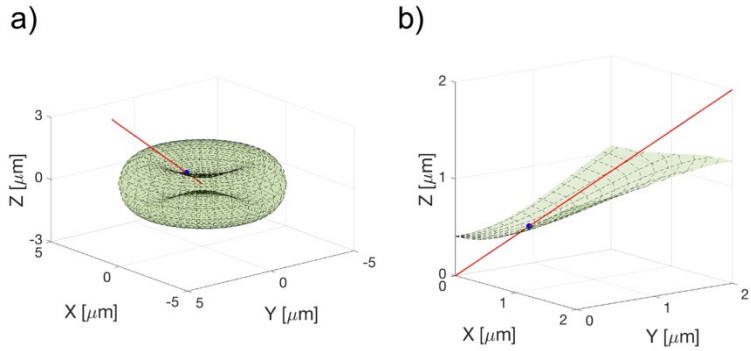

Figure 3.5. a) Example of the intersection point between an RBC in its standard position and modelled with the Evans-Fung model and a light ray. The light originates at $\boldsymbol{o}$ *= (5,5,5) and end in* $\boldsymbol{e}$ *= (0,0,0). b) Enlargement of (a) to better appreciate the intersection point.*

In the specific case, the transformations are only rotation and translation and are encoded in the rotation ($\boldsymbol{R}$) and translation ($\boldsymbol{T}$) matrix. If the RBC in its standard position $\widehat{\boldsymbol{B}}$ undergone the transformation $\boldsymbol{TR}$ to get in the desired position $\boldsymbol{B}$:

$$\boldsymbol{B} = \boldsymbol{TR}\widehat{\boldsymbol{B}} \qquad 3.5$$

therefore, $\boldsymbol{o}$ and $\boldsymbol{d}$ need to be transformed as follows:

$$\widehat{\boldsymbol{o}} = \boldsymbol{T}^{-1}\boldsymbol{R}^{-1}\boldsymbol{o};\ \widehat{\boldsymbol{d}} = \boldsymbol{R}^{-1}\boldsymbol{d}. \qquad 3.6$$

Hence, the intersection point and the normal vector are calculated as previously. Lastly, the intersection point's co-ordinates have to be roto-translated back to the initial condition, while the normal vector has to be rotated only.

Figure 3.6 shows an example of the calculation of the intersection point for a roto-translated cell. This process is repeated for each light ray and for each scattering event.

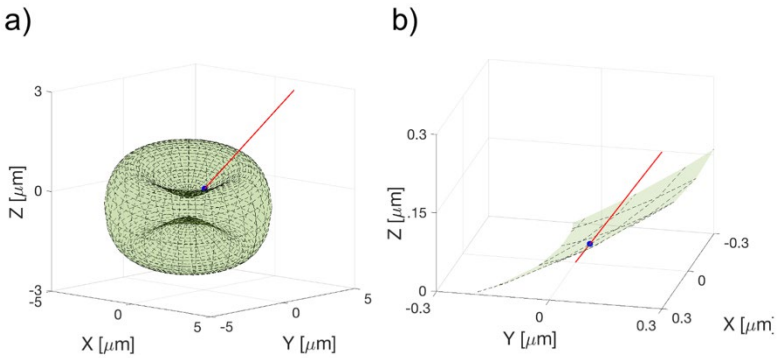

Figure 3.6. a) Example of calculation of intersection point between a roto-translated RBC modelled with the Evans- Fung model and a light ray. The light ray originates at $\boldsymbol{o}$ *= (5,5,5) and end in* $\boldsymbol{e}$ *= (0,0,0). b) Enlargement of (a) to better appreciate the intersection point.*

3.5. Numerical computation

In this section, the numerical investigation of optical forces acting on an RBC trapped by a single and multi-beams OT is presented. The investigation starts by analysing the forces and the torques exerted by a single-beam OT for RBC's displacements and rotations in respect to all the Cartesian co-ordinates to illustrate the methodology used to investigate the equilibrium configuration. The same analysis is then used to characterise the optical trapping of a RBC with two, three and four focused laser beams in highly symmetric configurations. The entire set of numerical computations

made in this thesis has been carried out with a standard labtop unless otherwise stated.

3.5.1. Single-beam optical tweezers

3.5.1.1. Optical forces

I first consider an RBC trapped by a single-beam optical tweezer (SBOT) in its 'folded' configuration. The RBC is firstly displaced along the x-direction (i.e. the direction perpendicular to the optical axis in the plane of the cell) between -3 μm and +3 μm with steps of 0.01 μm as schematically depicted in Figure 3.7-a. After each step, the optical forces are calculated in all three dimension via eq. 2.4.

Since the density of the RBC (ρ_{RBC} = 1.11 g/cm^3 = 1100 kg/m^3) is higher than that of the surrounding medium (ρ_w = 1 g/cm^3 = 1000 kg/m^3), the action of a constant force acting along the negative z-direction must be considered:

$$\boldsymbol{F}_b = V_{RBC}(\rho_{RBC} - \rho_w)\boldsymbol{g} \qquad 3.7$$

Considering a cell volume of 94 x 10^{-18} m^3,[14] $\boldsymbol{F}_b$ = -0.1 pN. $\boldsymbol{F}_b$ is always considered in my calculation unless otherwise stated.

As a first step in my numerical investigation, I determine the convergence of the simulation as a function of

the number of light rays used to describe the light beam. To do so, I simulate numerically the total optical force ($\boldsymbol{F}_{tot}$) acting on the centre of cell as function of the cell displacements from the origin of the reference frame along the x-direction. More information regarding the particular shape of the force-displacements curves will be given shortly after in the text.

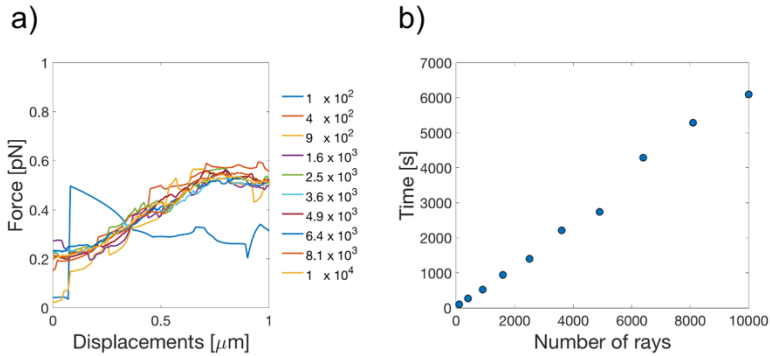

Figure 3.7. a) Simulation of $F_{tot}(x)$ as a function of the number of light rays used in the simulation, and (b) time required to simulate points 601 as a function of the number of light rays.

To evaluate the convergence, $\boldsymbol{F}_{tot}(x)$ is simulated starting from $1{\cdot}10^2$ light rays with up to $1{\cdot}10^4$ light rays. Figure 3.7-a shows $\boldsymbol{F}_{tot}(x)$ as a function of the number of light rays for cell displacement between 0 and 1 μm. Here, it can be seen that $\boldsymbol{F}_{tot}(x)$ rapidly converges as the number of light rays increases. In particular, if more than $1.6{\cdot}10^3$ light rays are used $\boldsymbol{F}_{tot}(x)$ seems not variate further. Moreover, the

computation time increases linearly with the number of light rays used in the simulation. Thus, since the convergence seemed reached when $1.6 \cdot 10^3$ are used, in the following of my thesis I make use of $1.6 \cdot 10^3$ (unless otherwise stated) to save computation time.

Figure 3.8-b shows the total optical force in terms of the three Cartesian components as a function of the displacement of the cell's centre mass (CM) from the origin (the focal point of the beam). For x-displacements, no net forces act along the y-component ($F_{y,1}(x)$). On the contrary, significant forces arise along x- and z-direction. $F_{z,1}(x)$ originates from the scattering force generated by the trapping laser, and acts pushing the cell towards $+\hat{\boldsymbol{z}}$. The shape of $F_{x,1}(x)$ demonstrates the transverse trapping. Near the origin $F_{x,1}(x)$ has positive gradient, suggesting that the RBC is pushed away from the optical axis until it reaches a position where $F_{x,1}(x)$ vanishes with negative gradient at $x_{eq,1}$ = ±1.95 μm, Figure 3.8-b. This is a consequence of the biconcave disc shape of the RBC, since the RBC can maximize the overlap of the cell volume with the beam when the beam focus is near the thickest part of the cell. Via a linear fit to the roughly linear portion of the graph in the region of the equilibrium positions yields a (power normalized) spring constant of $k_{x,1}$ = 0.17 pN·μm^{-1}·mW^{-1}.

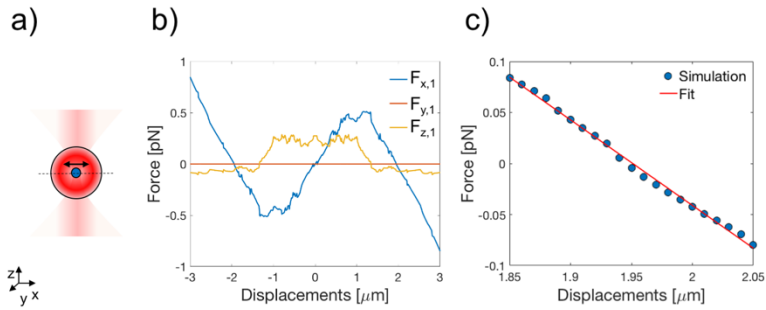

Figure 3.8. Force-displacement curve for cell displacements along the x-direction. a) The cell is positioned in the folded state and then is displaced along the x-direction. In blue is highlighted the centre of mass of the cell. b) Total optical force as a function of the cell displacements from the origin of the Cartesian co-ordinates system. The total force is shown in terms of the Cartesian co-ordinates. c) Trap stiffness extrapolation from the force-displacement curve.

The origin of fluctuations present in the force traces must be sought in the finite number of light rays used for the simulation. As said above in the text, a consistent increment in the number of light rays would slightly decreases these features, but it does not eliminate completely, Figure 3.7-a. This would also increases the time of simulation consistently, Figure 3.7-b. Moreover, the peculiar shape of the red blood cell could induce total internal reflection when a light ray hit the interior of the dimple at specific angles. The latter could cause force spikes that reflects in inhomogeneities in the force trace as extensively discussed later in the text.

Subsequently, the RBC is placed at $x_{eq,1}$ in its 'folded' configuration (Figure 3.9-a), and the force-displacements curve is obtained for displacements along the y-direction (i.e. normal to the cell's plane), Figure 3.9-b. In this case the range of displacements is smaller compared to Figure 3.8-b, since the cell is thinner in this direction. From Figure 3.9-b can be seen that $F_{y,1}(y)$ decreases linearly within the interval analysed (vanishes at $y_{eq,1}$ = 0 μm), and fitting a line to the linear part of the data I extrapolate the trap stiffness in this direction $k_{y,1}$ = 0.30 pN·μm^{-1}·mW^{-1}, Figure 3.9-c.

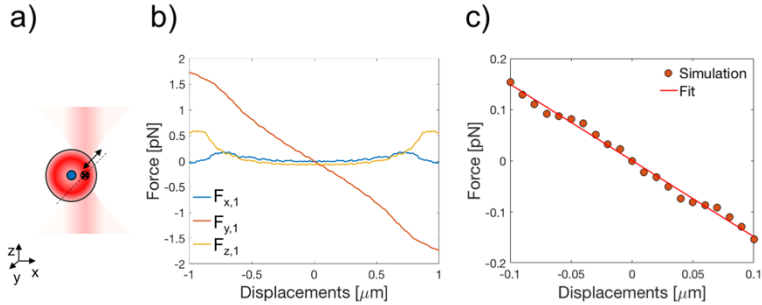

Figure 3.9. Force-displacement curve for cell displacements along the y-direction. a) The cell is positioned $x_{eq,1}$, and then is displaced along the y-direction. In blue is highlighted the centre of mass of the cell. b) Optical force as a function of the displacements from the origin (focal point of the beam). The force is presented in terms of the Cartesian co-ordinates. c) Trap stiffness extrapolation from the force-displacement curve.

The RBC is then placed at $x_{eq,1}$ and $y_{eq,1}$, Figure 3.10-a, and the optical forces are calculated for displacements

along the z-direction. Along this direction the trapping behaviour, that is the total force $F_{z,1}(z)$ = 0 with a negative slope around an equilibrium position, emerges only when the effective weight of the cell (approximately 0.1 pN) is also included and is located at $z_{eq,1}$ = -0.8 μm. The linear fit of the approximately linear part of the data produces a (power normalized) trap stiffness $k_{z,1}$ = 0.04 pN·μm^{-1}·mW^{-1}. As expected, $k_{z,1}$ is smaller than $k_{x,1}$ and $k_{y,1}$ since the gradient in the light intensity is smaller along the z-direction. However, both $F_{x,1}(z)$ and $F_{z,1}(z)$ have an unexpected behaviour that suggests the impossibility to have a stable trapping for a single-beam optical tweezer since there are no positions for which the total force vanishes.

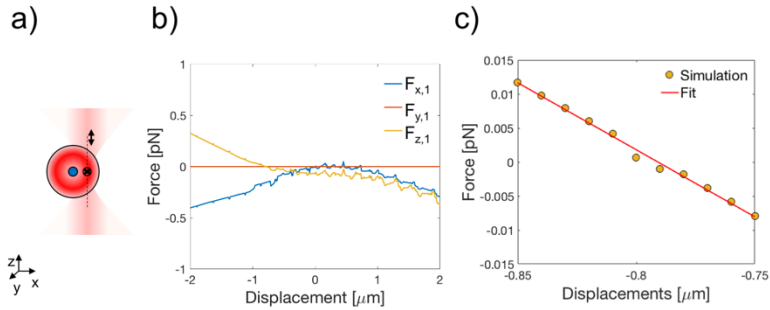

Figure 3.10. Force-displacement plot for cell displacement along the z-direction. a) The cell is positioned in the equilibrium position along x and y and then is displaced along the z-direction. In blue is highlighted the centre of mass of the cell. b) Optical force as a function of the displacements. The force is presented in terms of the Cartesian co-ordinates, c) Trap stiffness evaluation from the force-displacement curve.

To better comprehend this unexpected behaviour, $F_{x,1}(z)$ and $F_{z,1}(z)$ are decomposed in the scattering ($\boldsymbol{F}_{s,1}$) and gradient ($\boldsymbol{F}_{g,1}$) components, Figure 3.10-a and -b. Comparing $F_{s,z,1}$ and $F_{g,z,1}$ with $F_{z,1}(z)$, it is possible to directly associate the unexpected behaviour of $F_{z,1}(z)$ to a strong scattering components that arises at slightly negative displacements. It could be hypothesised that this trend is related not only to the presence of the dimple but also to its shape. Moreover, even $F_{x,1}(z)$ presents a significant scattering component and even in this case, this behaviour could be associated to the dimple. It seems clear that the dimple plays a critical role in determining the optical forces. In the next section, the influence of the dimple on the ray path and therefore on the optical forces is analysed meticulously.

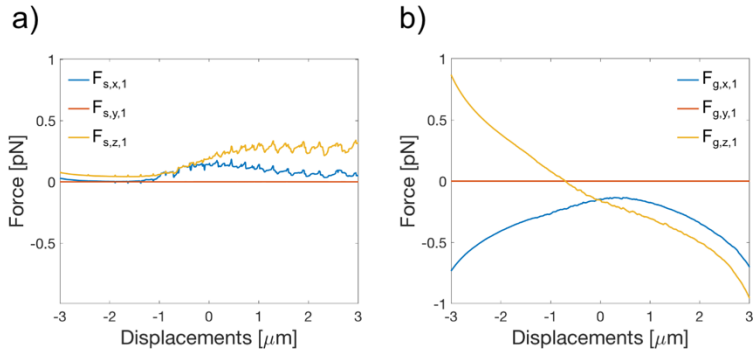

Figure 3.11. Scattering (a) and gradient (b) component of the total optical force acting on the centre of mass of the cell as a function of the cell's displacement along the z-direction, Figure 3.9.

3.5.1.1.1. The importance of being dimpled

The typical conformation of a healthy red blood cell is that of a biconcave disk. This morphology has strong repercussions on the optical properties of a RBC. Indeed, the healthy cell can be seen as a negative lenses. Intuitively, this means that the cell is repelled away from the origin because of the concavity in the middle, while it is trapped at the thickest portion at the periphery in order to maximise the overlap between the cell volume with the high intensity part of the beam.

The importance of the presence of the dimple, and its shape, in determining the force displacements curve observed for cell displacement along the z-direction is investigated (see section 3.5.1.1). The force-displacements curves for cell displacements along the z-direction are analysed in detail (considering every single ray) while keeping the cell at the $x_{eq,1}$ and $y_{eq,1}$ (see section 3.5.1.1). Since I am investigating the influence of the cell shape on the optical forces, I exclude the $\boldsymbol{F}_b$ during the present analysis.

Figure 3.12-a shows an example of rays traces for the RBC located at the point of equilibrium ($x_{eq,1}$= +1.95 μm, $y_{eq,1}$ = 0 μm, $z_{eq,1}$ = -0.8 μm), and the light ray exerting the highest force on the cell is highlighted in blue. The blue ray hits the cell at an angle such that it undergoes to total internal

reflection (TIR) in the interior of the dimple. This ray trajectories is common for a RBC in this configuration, and these rays are associated with the force spikes observable along every Cartesian direction which contributes to increase the scattering component, Figure 3.12-b.

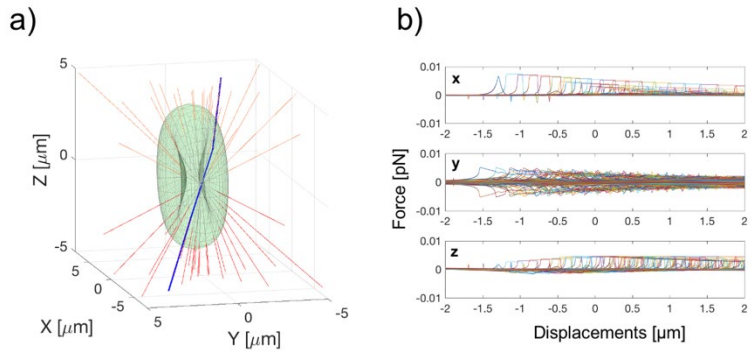

Figure 3.12. Effect of the dimple on the ray path and the optical forces for a cell placed at $x_{eq,1}$ and $y_{eq,1}$. a) Ray tracing for a dimpled cell and the forces generated along every direction by every single ray (b), In (a) the blue-ray is the light ray that generates the highest force on the cell.

However, due to the symmetry of the system, the effect of a pair of rays along the y-direction cancel out and not net optical force is present along this direction, Figure 3.12-b and Figure 3.10-b. Conversely, in this condition, the system lack of symmetry along the x- and z-direction, and the contribution of every two light rays does not cancel out generating the inhomogeneous and unexpected force traces

observable for $F_{x,1}(z)$ and $F_{z,1}(z)$, Figure 3.12-b and Figure 3.10-b. Intuitively, the behaviour of $F_{x,1}(z)$ would be the same but with opposite sign if the cell is displaced at -$x_{eq,1}$. Notably, in absence of $\boldsymbol{F}_b$ the light gradient alone would not be able to stably trap the RBC along the beam propagation direction. In this condition, the cell 'optically levitates' since the balance between $\boldsymbol{F}_b$and $F_{1,s,z}$ determine the point of equilibrium along the z-direction.[22] However, despite this, in real experiments conducted at higher beam powers (10-100 of mW), the cell may deform in response to the radiation pressure (see paragraph 3.5.1.3).[23] Consequently, the dimple structure changes, and thus the ray paths could be less affected by the cell's shape, and subsequently $F_{1,s,z}$ could decrease significantly.

In absence of the dimple the light rays do not undergo TIR, and the strong force of each light ray contribution are visible only along the y-direction, Figure 3.12-a-b. However, in this case the contribution of every two light rays cancels out and no net force arises along this direction, Figure 3.12-c. On the contrary,

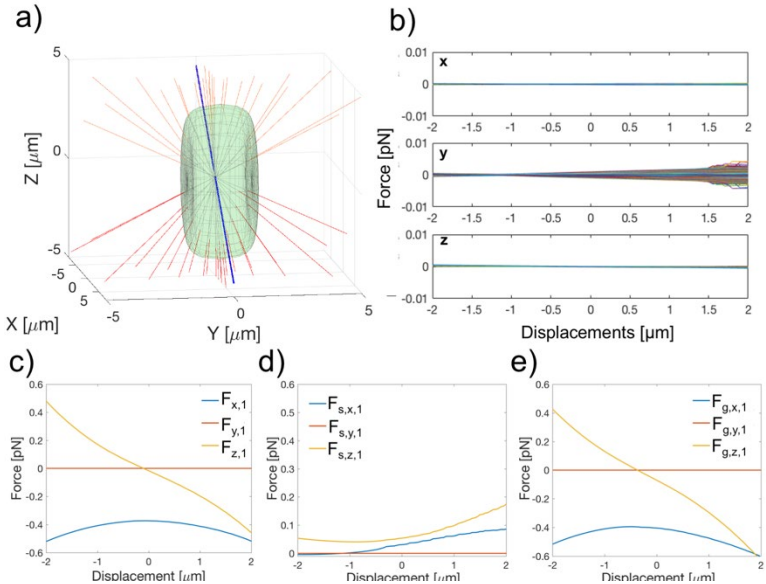

Figure 3.13. Effect of the dimple on the ray path and the optical forces for a RBC without dimple (i.e. flat disk) placed at $x_{eq,1}$ and $y_{eq,1}$. a) Ray tracing for a flat disk and the forces generated along every direction by every single ray (b), In (a) the blue-ray is the light ray that generates the highest force on the cell. c) Total optical force acting on the cell as function of the cell displacements form the origin. d) and e) scattering and gradient component of the optical forces as function of the cell distance from the origin. The forces are shown in terms of the Cartesian components.

since the dimple is not present, a strong negative force component is always present along the x-direction which pulls the cell towards the point of higher light intensity (origin), and is almost completely attributable to the gradient component, Figure 3.13-d and -e. On the other hand, $F_{z,1}(z)$

is homogeneous and decreases monotonically over the entire interval.

Therefore, it is clear as the complex biconcave shape of a healthy RBC is of paramount importance in determining the ray trajectories, the optical forces and ultimately the point of equilibrium for a RBC.

3.5.1.2. Optical torques

In chapter 2 the effect of the optical pressure on non-spherical object like cylinders or ellipsoids is introduced. For these non-spherical objects, optical torques arise and tend to align the particles with the optical axis. As introduced in section 3.1, this is the case for an optically trapped RBC. Experiments have shown that the RBC gets folded in the optical trap acquiring the equilibrium configuration shown in Figure 3.1-b. Therefore, apart from the forces analysed in section 3.5.1.1, there must also be restoring torques that act on the RBC to keep it in the folded configuration.

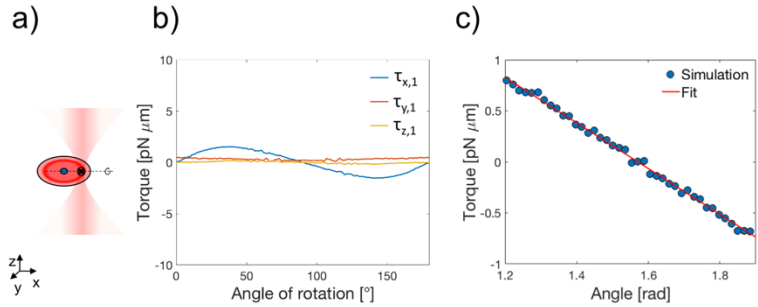

Figure 3.14. Optical torques acting on an RBC for cell rotation around the x-direction. a) Schematic depiction of the rotation. b) Total τ as a function of the angle of rotation given in terms of the three-cartesian component. c) Rotational trap stiffness calculation.

To analyse the torques generated by a single tightly focused laser beam on an RBC, the rotations around the x-axis are analysed first. The cell initially is placed at ($x_{eq,1}$, $y_{eq,1}$) in the flat configuration as schematically in Figure 3.14-a. The cell is rotated around an axis passing through the centre of the trap and parallel to the x-axis with steps of 1° and the optical torques are calculated after each step through equation 2.5. Figure 3.14-b shows the torque (τ) components acting on the cell while rotating 180°. As the cell starts to rotate from the flat configuration (0° and 180°), $\tau_{x,1}$ increases reaching a peak at 35°. After this peak, $\tau_{x,1}$ decreases linearly towards a second peak at 145°, where $\tau_{x,1}$ is equal in magnitude, but the sign is inverted. On the contrary, $\tau_{y,1}$ and $\tau_{z,1}$ fluctuates around 0.

The point at which $\tau_{x,1}$ vanishes with negative slope is the rotational point of equilibrium.[10] It occurs when the cell is rotated of 90° around the x-axis which corresponds to the 'folded' configuration observed experimentally.[6] For every rotation from this configuration, a restoring torque acts on the RBC pushing back the cell at the rotational equilibrium orientation. The linearity of $\tau_{x,1}$, for small angular displacement from 90°, allows one to extract a 'rotational' trap stiffness. By the fit of $\tau_{x,1}$ vs angle plot with a line, the (power normalized) angular stiffness can be extracted $k_{\alpha,1}$ = 0.22 pN·µm·rad^{-1}·mW^{-1}.

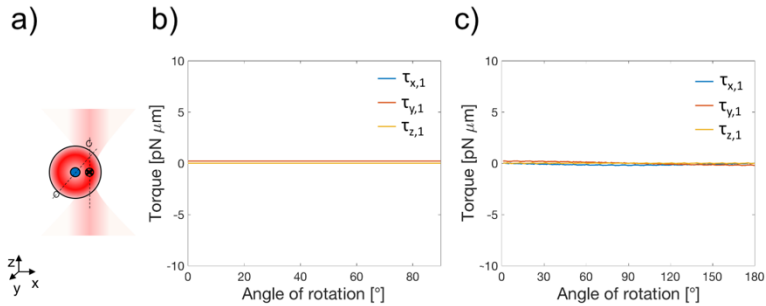

Figure 3.15. Optical torques acting on an RBC for cell rotation around the y- and z-direction. a) Schematic depiction of the rotation. b) Total τ as a function of the angle of rotation given in terms of the three-cartesian component. c) Rotational trap stiffness calculation.

Other two rotations are possible for an RBC trapped by a single beam as schematically depicted in Figure 3.15-a. The cell can rotate around an axis passing through the centre

of mass and parallel to the y-direction, or it can rotate around an axis passing through the trapping point and parallel to the z-direction Figure 3.15-a. For both kinds of rotation, no significant τ arise in any direction, Figure 3.15-b-c. Considering rotation around the y-axis, it is relatively easy to picture that the cell does rotate around its axis of symmetry, and thus no significant torques can arise, while for rotation around the cell does not change its position in respect to laser beam. Therefore, for a single-beam optical tweezer, the RBC is free to 'flap' around the z-axis.

Even though not specifically studied, the presence of the dimple is thought to have a minor effect on the optical torque. In fact, a healthy RBC behaves as one would expect from an ellipsoidal particle with the cell aligned with its major axis along the beams' propagation direction.

3.5.1.3. Optical stress distribution

In the previous sections I described the optical force and torques acting on the centre of mass of the RBC. However, as I introduced in chapter 2, the photon momentum is transferred to the particle at the particle surface, and this generates an optical stress on the microparticle. The optical stress is always orthogonal to the particle's surface and points outwards the object's surface.[15] If the micron-sized object is elastic enough the surface forces induce the object

deformation. In the present context, the forces distribution on the particle surface can be evaluated considering only the force component along the normal to the cell surface via the following equation:

$$\boldsymbol{F}_{ray} = \left[\frac{n_i P_i}{c}\,\hat{\boldsymbol{r}}_i - \frac{n_i P_r}{c}\,\hat{\boldsymbol{r}}_r - \frac{n_t P_t}{c}\,\hat{\boldsymbol{r}}_t\right]\cdot\hat{\boldsymbol{n}} \qquad 3.8$$

where each term of the eq. 3.8 is described in eq. 2.2, and $\hat{\boldsymbol{n}}$ is the unit normal vector to the RBC surface at the point of incidence. To calculate the force distribution generated by a SBOT, the RBC is place at the equilibrium position ($x_{eq,1}$, $y_{eq,1}$, $z_{eq,1}$), and the forces are calculated through eq. 3.8.

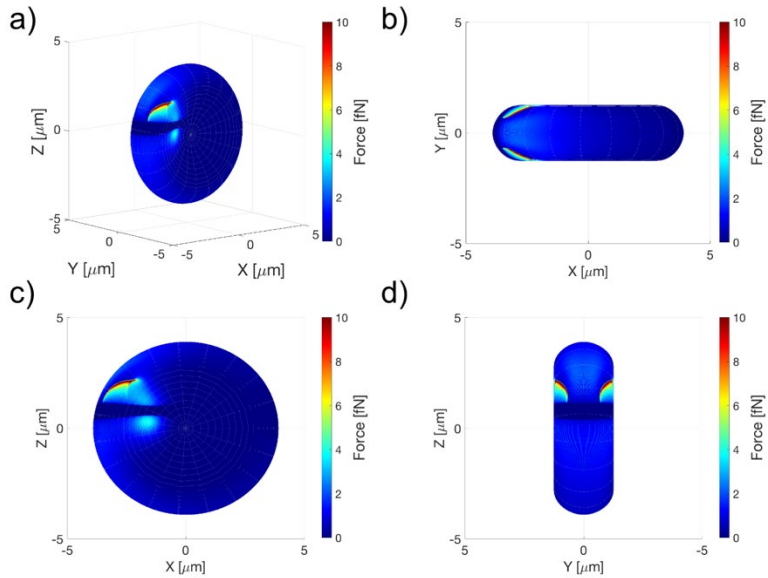

Figure 3.16. Forces distribution generated by a SBOT on the surface of a RBC (a), top-view (b), lateral view (c) and front-view (d). For simplicity the cell is centred on the origin.

As expected, the force distribution profile is completely asymmetrical in respect to the x-direction, Figure 3.16-b and c, but is symmetrical in respect to the y-axis, Figure 3.16-b and d. The force distribution profile shows two characteristic symmetric peaks on the upper portion of the cell, Figure 3.16-d. This peaks corresponds, approximately, to the position where the cell is trapped and are due to the combination of rays coming from the outermost part of the beam, and to rays coming from the centre of the beam. More importantly, the force distribution shows a peak also in the

vicinity of the dimple. This is particular important since the latter is the region of cell that influences most the ray path, and thus any significant deformation would be really important in determining the equilibrium configuration. Therefore, the present calculations could differ from experimental data since the cell deformation is not accounted for. However, if the deformation is considered, the ray tracing scheme adopted until now would fail, and a new (computationally expensive) approach needs to adopted (see chapter 7). Thus, for the remainder of the thesis the cell is always considered to be a rigid body.

3.5.2. Double-beam optical tweezers

In this section, I report the numerical investigation regarding the optical trapping of a red blood cell via a double-beam OT. The two beams' foci are positioned 5.06 μm apart along the x-axis, similarly to the experiments conducted by Agrawal and co-workers, and schematically depicted in Figure 3.17.[5] As for the single-beam OT, experiments have demonstrated that the cell reaches the equilibrium configuration in its 'folded' state, Figure 3.2. The force-displacements curves, and the spring constant, are calculated for displacements along each of the cartesian co-ordinates as depicted in Figure 3.17-a, while the optical

torques are analysed for rotations around the CM of the cell as depicted in Figure 3.17-b.

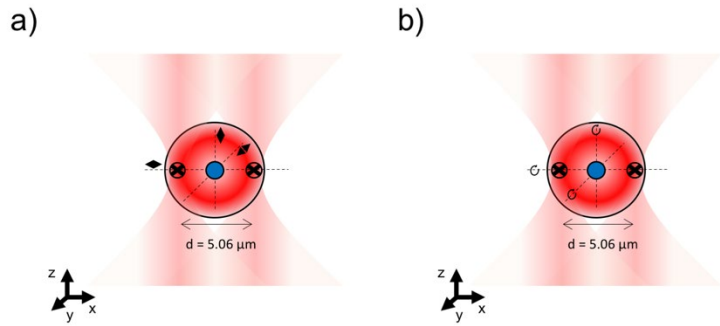

Figure 3.17. Schematic depiction of an RBC trapped by a double-beam optical tweezer. a) Direction along which the forces are calculated. b) Possible rotation of a trapped RBC around trap's centre.

Initially, I investigate the trapping mechanism along the z-axis constraining the cell plane in the x-z plane. In Figure 3.18-a are shown the results for the force-displacements along z-direction. $F_{z,2}(z)$ decreases linearly in the interval analysed and vanishes with negative slope at $z_{eq,2}$ = -0.23 µm suggesting the effective confinement along this direction. Following the same approach illustrated in the previous paragraph, I extrapolated the (power normalised) spring constant $k_{z,2}$ = 0.045 pN·µm^{-1}·mW^{-1}, insert Figure 3.18-a.

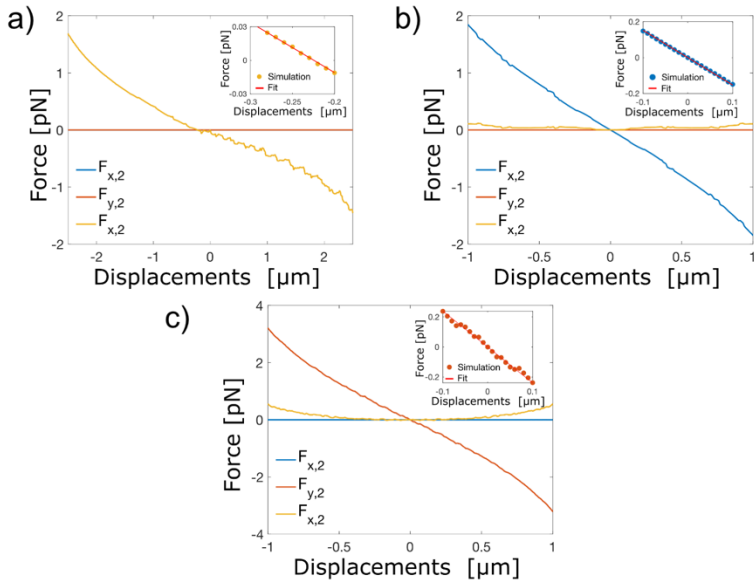

Figure 3.18. Force-displacements curves for an RBC trapped by a dual-beam optical tweezer for cell displacements along the z-direction (a), y-direction (b), and x-direction (c). The inserts show the linear fitting to the approximately linear part of the graph near the point of equilibrium.

Successively, the RBC is placed at $z_{eq,2}$ and is displaced along the x-direction calculating the optical forces after each step, Figure 3.18-b. Here it can be seen that $F_{x,2}(x)$ decreases linearly from 2 pN to -2 pN at 1 μm, and vanishes with negative slope at $x_{eq,2}$ = 0 μm, Figure 3.18-b. Fitting a line to the linear portion of the graph I obtained the spring constant $k_{x,2}$ = 1.528 pN·μm^{-1}·mW^{-1}, insert Figure 3.18-b.

Subsequently, the RBC is positioned at $x_{eq,2}$ and $z_{eq,2}$ and is therefore displaced along the y-direction. From Figure 3.18-c it can be seen that $F_{y,2}(y)$ vanishes with negative slope at $y_{eq,2}$ = 0 μm, and the (power normalized) spring constant is $k_{y,2}$ = 0.24 pN·μm^{-1}·mW^{-1}, insert Figure 3.18-c.

Compared to the single-beam case, the cell is confined at the centre of the trap in the x-y plane, and the values of the trap stiffnesses are doubled. However, the most intriguing difference is given by an additional degree of rotational confinement.

Figure 3.19 shows the torque-rotation curves for the three rotations schematically depicted in Figure 3.17-b. As expected, significant restoring torque arises for rotation about the x-axis ($k_{\alpha,2}$= 0.37 pN·μm·rad^{-1}·mW^{-1}) but not for rotation around the y-axis, Figure 3.19-a-b. However, if the cell is trapped by a double-beam OT a significant restoring torque ($k_{\gamma,2}$= 1.73 pN·μm·rad^{-1}·mW^{-1}) arises also when the RBC is rotated about the z-axis.

The numerical investigation shows how an additional degree of confinement arises for a double-beam optical tweezers compared to the single-beam case. The presented results suggest a complete three-dimensional confinement of the RBC with a cell confined in a plane containing the beams' foci and the optical axis. Moreover, the presented analysis finds good qualitative agreement with the experiments

conducted by Agrawal *et al.*[4,5] In fact, experiments shown that a healthy RBC is completely confined in a plane containing the beams' foci and the optical axis and it is not free to rotate around its centre of mass (except around the cell axis of symmetry). Here, I numerically investigated the origin of this confinement which can be correlated to the synergistic torque exerted by the two light beams. Also, compared to the single-beam case, the light's gradient alone is able to confine the RBC entirely, even in absence of the force of gravity.

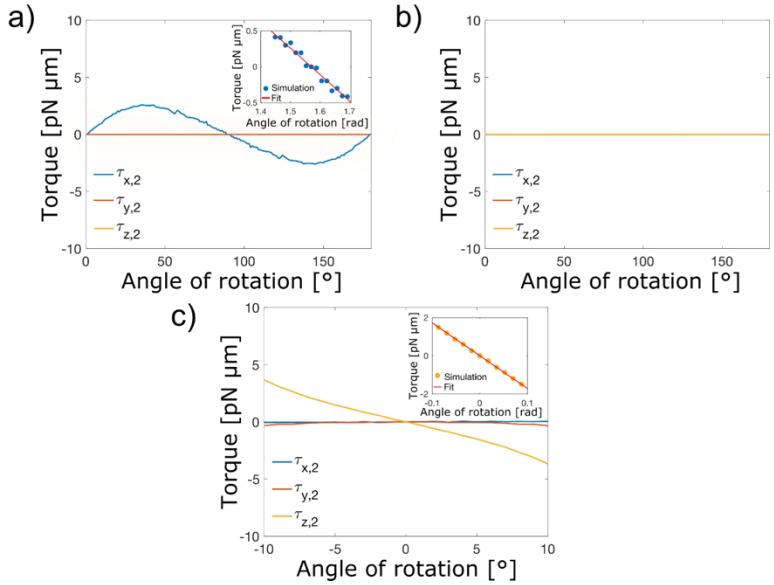

Figure 3.19. Torque-rotation curves for an RBC trapped by a dual-beam optical tweezer for a cell rotated around the x-axis (a), y-axis (b), and z-axis (c). The inserts show the linear fitting to the approximately linear part of the graph near the point of equilibrium.

3.5.3. Three and four beams optical tweezers

In this section I report the results of simulations performed for a three and four beams OT, and the equilibrium configuration is briefly discussed.

Figure 3.20 shows the configuration of a three-beams and four-beams optical tweezer. In these two alternative beam configurations, the foci of the beams are arranged in an equilateral triangle or in a square with the vertices on the thickest portion of the cell, red circle in Figure 3.20-a and -b.

Interestingly, in both cases, the RBC should find the equilibrium configuration when has its plane transverse to the optical axis, since the torques generated by the beams should balance out. Moreover, at the equilibrium configuration, the centre of mass of the cell should coincide with the origin of the Cartesian co-ordinates system in the x-y plane that is also the centre of the trap. However, because of the radiation pressure the centre of mass should be slightly shifted towards $+\hat{\boldsymbol{z}}$.

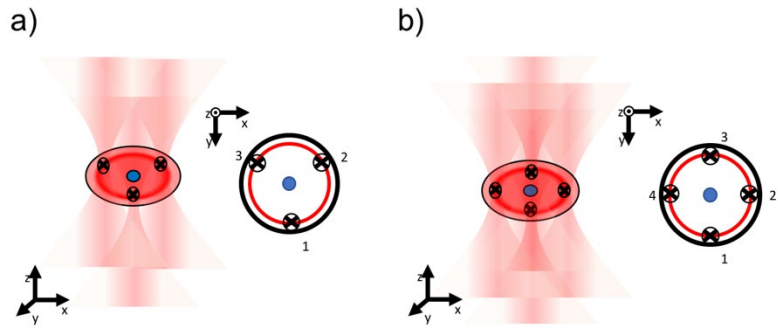

Figure 3.20. Configuration of a three-beams (a) and four-beams (b) optical tweezer. The two concentric circles represent the external diameter of the RBC (black line) and the diameter where the RBC is thickest (red line).

To verify the hypothesis, the same analysis proposed for a single-beam and double-beams OT are carried out again for the three-beams and four-beams case. The force-displacements curves are obtained for the cell in the configuration depicted in Figure 3.20-a and -b. The cell is displaced along each of the three Cartesian components, and the trap stiffnesses are extracted via the linear fit of the approximately linear portion of the graph.

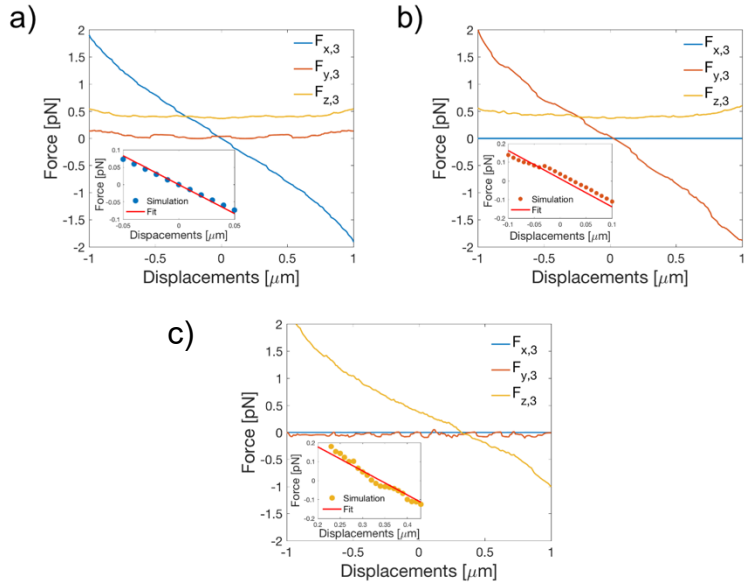

Figure 3.21. Optical trapping of a RBC in a triple-beam optical tweezer. Force-displacements curves for cell displacements along x- (a), y- (b) and z-direction (c). The inserts show the linear fit used for the extrapolation of the characteristic spring constant.

Once $x_{eq,3}$, $y_{eq,3}$ and $z_{eq,3}$ are obtained, the cell is rotated around an axis parallel to each of the Cartesian axes and passing through the centre of the trap, and the rotational trap stiffnesses are calculated as described previously. As in section 3.5.1 and 3.5.2, a constant force of gravity along the z-direction is always considered.

In Figure 3.21 and Figure 3.22 are shown the results of the calculation for a RBC optically confined by a triple-

beam optical tweezer. As expected, for this highly symmetric beams' configuration the cell finds an equilibrium position approximately at the origin of the x-y plane. However, since the light intensity gradient is not completely symmetric, the cell is slightly shifted along the y-direction ($y_{eq,3}$ = +0.025 μm). As a consequence of the scattering force the cell is pushed along the optical axis ($z_{eq,3}$ = +0.23 μm). The spring constants transverse to the optical axis ($k_{x,3}$ and $k_{y,3}$) are slightly bigger than $k_{z,3}$ as a consequence of the gradient in the light intensity.

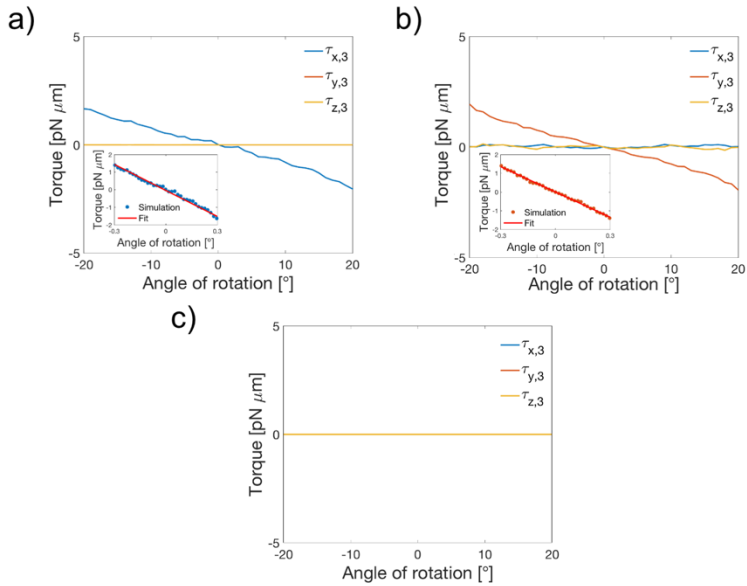

Figure 3.22. Torque-rotation curves for a RBC trapped by a triple-beam optical tweezer: rotation around the x-axis (a), y-axis (b), and z-axis (c).

The insets show the linear fitting to the approximately linear part of the graph near the point of equilibrium.

Rotationally, the cell finds an equilibrium orientation when the cell is in its 'flat' configuration which correspond to rotation of 0° around the x- and y-axis, and restoring torques are present for both type of rotation, but not for rotation around the z-axis, since for the latter the cell is spinning on its axis of symmetry, Figure 3.22-a-c. Therefore, with a triple-beam optical tweezer is possible to completely confine a RBC in its 'flat' configuration.

Figure 3.23 shows the force-displacements curves computed for a RBC optically confined by a four-beam optical tweezer, and in Table 3.1 are reported the values extracted from the computation. As expected, the equilibrium position is obtained for a cell centred at the origin of the x-y plane ($x_{eq,4}$ = $y_{eq,4}$ = 0 μm) and slightly shifted towards $+\hat{\boldsymbol{z}}$ ($z_{eq,4}$ = 0.35 μm). Compared to the three beams case, this shifting is a bit higher because of the effect of the fourth beam, which increases the scattering force along the z-direction. Not surprisingly, the spring constant along the direction transverse to the optical axis have the same value ($k_{x,4}$ = $k_{y,4}$) which is slightly higher that the value obtains along the z-direction.

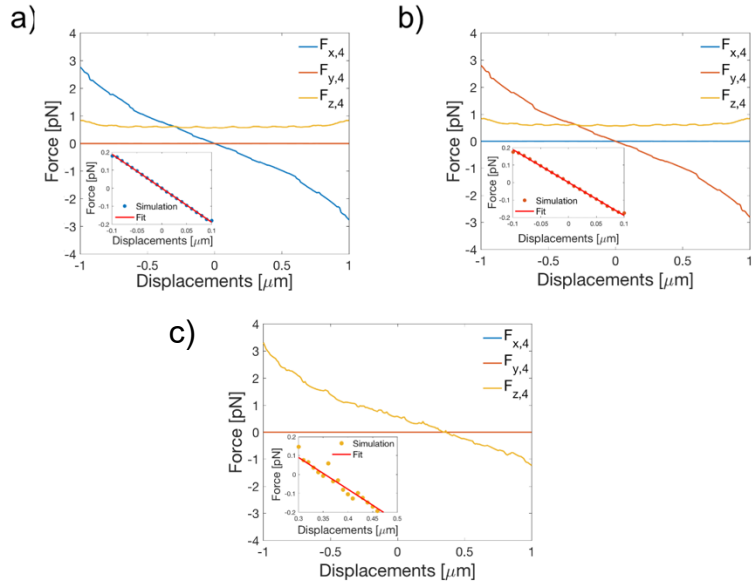

Figure 3.23. Optical trapping of a RBC in a four-beam optical tweezer. Force-displacements curves for cell displacements along x- (a), y- (b) and z-direction (c). The inserts show the linear fit used for the extrapolation of the characteristic spring constant.

The cell finds its orientational equilibrium when it is not rotated around either x- or y- (i.e. 'flat' configuration), and restoring torques are present for both rotation, suggesting an orientational confinement. For the same argument introduced for the three-beams OT, no torques are visible for rotation around the z-axis.

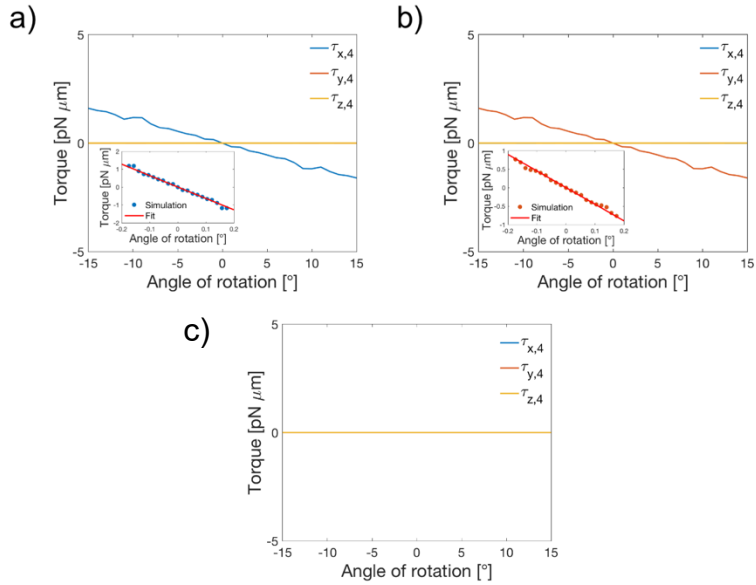

Figure 3.24. Rotational confinement for a RBC trapped by a four-beam optical tweezer: rotation around the x-axis (a), y-axis (b), and z-axis (c). The insets show the linear fitting to the approximately linear part of the graph near the point of equilibrium.

Experiments conducted by Rusciano and collaborators showed that a fourth-beams optical tweezers is able to confine a RBC in its flat configuration.[9] Here, my numerical investigation demonstrated how the synergistic effect of the fourth beams confine the RBC in its flat configuration as a consequence of the balancing of the optical torques generated by each beam. My results demonstrate to be in good qualitative agreement with the previously reported experiments. Compared to the triple-

beams optical tweezers, the trapping stiffnesses have higher values since an additional beam is used for trapping, Table 3.1.

	SBOT	DBOT	TBOT	FBOT
k_x (pN·μm^{-1}·mW^{-1})	0.17	1.53	0.11	0.09
k_y (pN·μm^{-1}·mW^{-1})	0.30	0.24	0.11	0.09
k_z (pN·μm^{-1}·mW^{-1})	0.04	0.045	0.10	0.08
k_α (pN·μm·rad^{-1}·mW^{-1})	0.22	0.37	0.33	0.32
k_β (pN·μm·rad^{-1}·mW^{-1})	0	0	0.31	0.33
k_γ (pN·μm·rad^{-1}·mW^{-1})	0	1.73	0	0

Table 3-1. Values of the trap stiffnesses and rotational trap stiffness for an RBC trapped by single- (SBOT), double- (DBOT), triple- (TBOT), and fourth-beams optical tweezers.

3.6. Chapter summary

In this chapter, I presented a theoretical investigation of the optical trapping of a healthy RBC in its biconcave conformation when trapped by a single- or multi-beams optical tweezer in the geometrical optics regime. The numerical study shed light on how the biconcave shape is essential to establish the rays' path, the optical forces and torques, and thus the equilibrium configuration of a healthy RBC. The methodology used to investigate the equilibrium configuration of a healthy RBC within an optical trap has been illustrated for a single-beam optical tweezer. Therefore, it has been numerically investigated the possibility to completely confine a RBC in space by means of a double-beam optical tweezer. It has also been shown that the addition of a third or fourth beams in highly symmetric arrangements impacts significantly the final equilibrium configuration of the RBC, confining the cell in its 'flat' configuration.

The presented analysis agrees well with experiments and can be adopted to investigate various parameters before performing experiments. Moreover, this approach can be directly applied to search for alternative RBC's equilibrium configuration by simply tuning the position of the beams forming the optical trap or to study the dynamics of a trapped RBC.

In the next Chapter I will present a study on the possibility to govern the position and orientation of a healthy RBC with a triple-beam optical tweezer.

3.7. Bibliography:

[1] R. Zhu, T. Avsievich, A. Popov, I. Meglinski, *Cells* **2020**, *9*, 545.

[2] J. P. Mills, L. Qie, M. Dao, C. T. Lim, S. Suresh, *Mech. Chem. Biosyst.* **2004**, *1*, 169.

[3] H. Basu, A. K. Dharmadhikari, J. A. Dharmadhikari, S. Sharma, D. Mathur, *Biophys. J.* **2011**, *101*, 1604.

[4] R. Agrawal, B. Ang, P. K. Balne, C. Richards, T. Smart, J. Cardoso, D. Shima, P. H. Jones, C. Pavesio, *Ocul. Immunol. Inflamm.* **2019**, *27*, 978.

[5] R. Agrawal, T. Smart, J. Nobre-Cardoso, C. Richards, R. Bhatnagar, A. Tufail, D. Shima, P. H. Jones, C. Pavesio, *Sci. Rep.* **2016**, *6*, 1.

[6] S. K. Mohanty, K. S. Mohanty, P. K. Gupta, *Opt. Express* **2005**, *13*, 4745.

[7] M. M. Brandão, A. Fontes, M. L. Barjas-Castro, L. C. Barbosa, F. F. Costa, C. L. Cesar, S. T. O. Saad, *Eur. J. Haematol.* **2003**, *70*, 207.

[8] G. B. Liao, P. B. Bareil, Y. Sheng, A. Chiou, *Opt. Express* **2008**, *16*, 1996.

[9] G. Rusciano, A. C. De Luca, G. Pesce, A. Sasso, *Sensors* **2008**, *8*, 7818.

[10] S. C. Grover, R. C. Gauthier, A. G. Skirtach, *Opt. Express* **2000**, *7*, 533.

[11] T. Avsievich, R. Zhu, A. Popov, A. Bykov, I. Meglinski, *Rev. Phys.* **2020**, *5*.

[12] G. B. Liao, Y. Q. Chen, P. B. Bareil, Y. Sheng, A. Chiou, M. S. Chang, *J. Biophotonics* **2014**, *7*, 782.

[13] P. B. Bareil, Y. Sheng, A. Chiou, *Photonics North 2006* **2006**, *6343*, 63430D.

[14] E. Evans, Y. C. Fung, *Microvasc. Res.* **1972**, *4*, 335.

[15] J. Guck, R. Ananthakrishnan, H. Mahmood, T. J. Moon, C. C. Cunningham, J. Käs, *Biophys. J.* **2001**, *81*, 767.

[16] G. S. Valchev, V. M. Vassilev, P. A. Djondjorov, *Bulg. Chem. Commun.* **2015**, *47*, 84.

[17] H. Funaki, *Jpn. J. Physiol.* **1955**, *5*, 81.

[18] P. W. Kuchel, E. D. Fackerell, *Bull. Math. Biol.* **1999**, *61*, 209.

[19] M. A. Yurkin, K. A. Semyanov, P. A. Tarasov, A. V. Chernyshev, A. G. Hoekstra, V. P. Maltsev, *Appl. Opt.* **2005**, *44*, 5249.

[20] A. S. Glassner, *An Introduction to Ray Tracing*; Glassner,.; Academic Press: London, 1989.

[21] A. Callegari, M. Mijalkov, A. B. Gököz, G. Volpe, *J. Opt. Soc. Am. B* **2015**, *32*, B6.

[22] A. Ashkin, *Proc. Natl. Acad. Sci. U. S. A.* **1997**, *94*, 4853.

[23] S. Rancourt-Grenier, M. Wei, J. Bai, A. Chiou, P. P.

Bareil, P. Duval, Y. Sheng, *Opt. Express* **2010**, *18*, 16029.

4. POSITION AND ORIENTATION CONTROL OF BICONCAVE RED BLOOD CELL IN OPTICAL TWEEZERS

In this chapter, I examine the possibility to govern the position and orientation of a red blood cell via a triple-beams optical tweezers. Here I apply the geometrical optics calculations introduced in chapter 3 to identify the final equilibrium configuration of a red blood cell via an iterative process. This methodology is demonstrated to be very effective when the equilibrium configuration of the cell is known from experimental evidence or if the configuration of the trap is simple. However, this approach fails when the trap increases in complexity and the equilibrium configuration of the cell is not known *a priori*. For this reason, I exploit a numerical scheme for the simulation of the Brownian motion of the optically trapped RBC to identify the final equilibrium configuration of the cell. Therefore, the Brownian dynamics simulations are used to investigate the extent of the governability of the RBC with a reconfigurable triple-beams optical trap.

4.1. Introduction

The refraction (bending) of incident light at a surface causes the transfer of recoil-momentum from the impinging photons to the object.[1] As first envisaged by A. Ashkin, these forces are significant enough to move, manipulate and confine micron-sized particles. In the very first experiments on optical manipulation, the researchers observed a spherical microparticle with a refractive index higher than those of the surrounding medium is simultaneously pushed along the optical axis and attracted towards the region of higher light intensity by a weakly diverging (in the sample) Gaussian laser beam. In the ray optics (RO) approximation, this observation can be interpreted in terms of the scattering force ($\boldsymbol{F}_s$) and the gradient force ($\boldsymbol{F}_g$); see chapter 2 for a detailed description.

In the first realisation of an optical trap, the authors made use of these two forces to optically confine a small dielectric particle. Indeed, $\boldsymbol{F}_s$ generated by two counter-propagating lasers beams are subtractive and cancel out at the point of symmetry of the two beams while $\boldsymbol{F}_g$ is always additive. These two forces act synergistically to confine the particle at the point of equilibrium.[2] Soon after, A. Ashkin *et al.* grasped that if a strong gradient is created in all the spatial dimensions through a high numerical aperture objective, $\boldsymbol{F}_g$

would be able to confine a dielectric micron-sized object in space close to the beam focus.[3]

In one of the first applications of OT in biology, the researchers were able to optically trap rod-like viruses and living bacteria.[4] Interestingly, the shape of the living cell deviated from that of a simple spherical particle. Indeed, as extensively discussed in chapters 2 and 3, when a light beam strikes a non-spherical object like an ellipsoid or a cylinder, significant optical torques (τ) arise, which tend to align the object with the optical axis. Shortly after, Ashkin and collaborators could stably trap and manipulate more complex organisms as the algae Spirogyra. More interestingly, the researchers could optically trap the biconcave disk-shaped human red blood cell (RBC), observing no appreciable damage if an infrared red light source were used for trapping.[5]

In the last couple of decades, the use of OT in red blood cell research has extended rapidly. It has been applied to investigate various biochemical and biophysical properties of the RBC.[6] As discussed in detail previously (see chapter 3), researchers exploited the indirect trapping (use of handles to manipulate the RBC) and the direct trapping where the illumination light is used to manipulate the cell. Interestingly, if directly trapped, a healthy biconcave RBC can assume two different and alternative orientations within the optical trap

depending on the number of beams used for trapping, as extensively discussed in chapter 3, Figure 4.1-a-b.

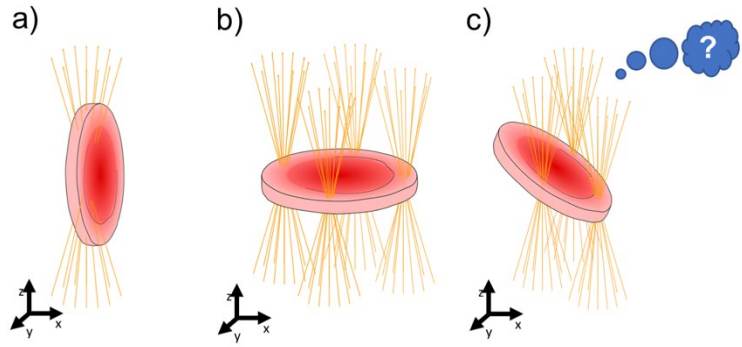

Figure 4.1. Schematic depiction of an RBC in its 'folded' configuration in a single-beam optical trap (a). (b) Illustration of an erythrocyte in a four-beam optical tweezer in its 'flat' configuration. (c) Schematic representation of the proposed alternative beam configuration useful for control the orientation of an RBC.

In a single-beam or a double-beam OT, the RBC is trapped on its thickest portion and the optical torque confines the cell to have its plane orientated parallel to the optical axis in the so-called 'folded' configuration (see chapter 3) Figure 4.1-a. In a double-beam OT set-up, the torques generated by the two beams act synergistically and confine the cell in the 'folded' configuration in a plane containing the beams' foci and the optical axis. On the contrary, if three or four beams arranged in very symmetric configurations are used, the torques generated by each beam cancel out, and the cell

finds its equilibrium when it has its plane orthogonal to the optical axis, referred to as 'flat' configuration (see chapter 4).

However, what happens if one breaks the symmetry in the configuration of the beams' foci?

In principle, it could be possible to identify particular intermediate beams' configuration between the double-beams trap and the triple-beams trap able to confine the cell in an intermediate equilibrium configuration between the 'flat' and the 'folded' one, Figure 4.1-c. Identifying a possible beams' arrangement that could finely tune and confine the orientation of an RBC is of practical importance. It could unlock the possibilities to carry out orientational dependent studies.

For these reasons, in this chapter, I report numerical experiments performed to identify a possible alternative equilibrium configuration for an RBC within a multi-beam optical trap.

4.2. Model

In the current model, a three-dimensional Cartesian co-ordinates system is considered. The laser beams propagate towards $+\hat{\boldsymbol{z}}$ and possess a Gaussian intensity distribution. In agreement with the vast majority of experiments and to match the light source present in our laboratory (Nd:YAG laser), the wavelength of the light beam is chosen to be 1.064 μm. The

beam waist at the back aperture of the objective is 50 μm, the numerical aperture (NA) of the objective is 1.3, and the back aperture is 9.78 μm, such that the incoming beam overfills it. The power of each beam is always 5 mW. The beams' power is maintained in the mW range for reasons reported in section 3.1.

The RBC is considered to be immersed in a water-based medium with homogeneous refractive index ($n_1 = 1.33$), temperature (T = 298 K), and dynamic viscosity (η = 0.001 Pa·s). Note that T is not the physiological temperature but the temperature at which the experiments are performed. The RBC is always considered a rigid body (not deforming in response to the optical pressure), and filled by a non-absorbing medium with isotropic physical properties (n_2 =1.38, ρ_{cell} =1.11 g/cm^3). The RBC is always in its healthy biconcave disk conformation, and the parameters describing the RBC disk are those extensively described and used in section 3.1.

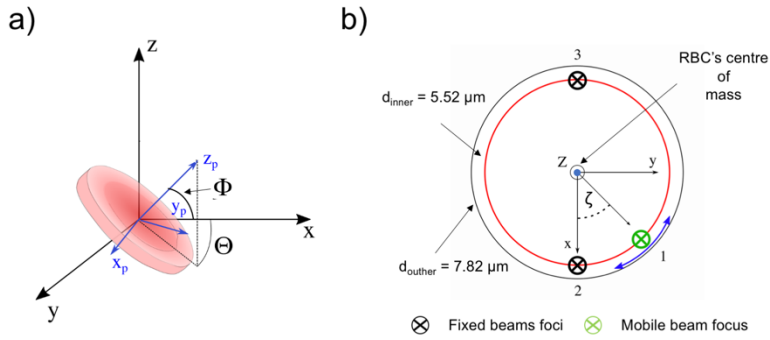

Figure 4.2. a) Laboratory and particle reference frame used in the current chapter. b) Schematic depiction of the triple-beams optical trap and the polar co-ordinates system used to identify the position of beam 1.

In addition to the laboratory reference frame (Σ_l), a second Cartesian frame of reference centred on the centre of mass of the RBC is defined: the particle reference frame (Σ_p), Figure 4.2-a. Σ_p always encodes the position and orientation of the particle. The polar orientation of the RBC is always given by the angle Φ and the azimuthal orientation by the angle Θ, as shown in Figure 4.2-a. If Φ = 90°, the cell is in its 'flat' configuration whilst for Φ = 0°, the cell is in its 'folded' configuration. On the other hand, when the cell is oriented towards $+\hat{y}$, $\Theta = 90°$, while $\Theta = -90°$ when the cell is oriented towards $-\hat{y}$. In the remainder of this chapter, Φ is always comprised in between [0°,90°], while θ is comprised in between [-180°;180°].

Only the first two scattering events (reflection and refraction) are considered since the fraction of power reflected for biological samples is very low (< 0.001), because of low refractive index contrast with the surroundings.[7] Since the characteristic diameter of an RBC (7.92 μm) is bigger than the wavelength used for the calculations, the geometrical optics approximation is completely fulfilled, and the optical forces and torques can be calculated with GO following the scheme reported in chapter 3.

In this study, the triple-beams optical tweezer is composed by three identical and tightly focused laser beams. Two beams (beam 2 and 3) are always arranged along the x-axis as in a double-beams optical tweezer. They are positioned in a diametrically opposite location on the thickest portion of the cell as shown in Figure 4.2-b. A third beam (beam 1) can be translated over the thickest portion of the cell and is used to counteract τ_x generated by the beams 2 and 3. For simplicity, the position of beam 1 is described by a polar co-ordinates system in the x-y plane. Therefore, the location of beam 1 is defined by a single angle (ζ), and the distance from the origin is fixed and equal to the radius of the thickest portion of the cell (2.76 μm), Figure 4.2-b.

4.3. Numerical computation

4.3.1. Static equilibrium searching

As introduced previously, a possible beams' configuration for a triple-beam optical tweezer that can confine an RBC in defined orientation must be sought between the triple-beam optical tweezer and a double-beam optical tweezer.

However, for asymmetric beams configurations, and in the absence of experimental evidence, it's not trivial to predict the final equilibrium configuration *a priori*. For this reason, initially, I organise the three beams as an isosceles triangle similarly to the triple-beams trap already analysed in chapter 3. Beam 1 is positioned at ζ = 90°, while beam 2 and 3 are positioned along the x-axis, as schematically depicted in Figure 4.3. With this configuration, the torques generated by beam 2 and 3 should be counteracted, at least to some extent, by beam 1. If this is true, the cell should be confined in an intermediate orientation between the 'flat' and the 'folded' one. In particular, the orientation of the cell plane (Θ and Φ) should be directly dictated by the specific angular position of beam 1. In addition, the presence (and the location) of beam 1 creates an asymmetry in the gradient force, and so the equilibrium position of the RBC is expected to be shifted towards beam 1. Conversely, the three beams

will act synergistically along the optical axis pushing the cell towards $+\hat{z}$.

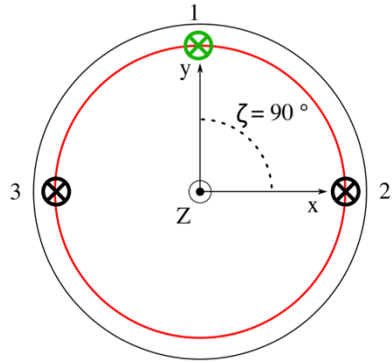

Figure 4.3. Schematic depiction of the triple beam optical tweezer used in the first set of numerical experiments. Beams 2 and 3 are positioned in a diametrically opposite position along the x-axis, while beam 1 is positioned at ζ = 90°.

The equilibrium configuration of an RBC trapped by a triple-beam OT with the aforementioned configuration is initially investigated with the same scheme adopted in chapter 3. Each possible cell translation and rotation is analysed independently and successively. This method is named static equilibrium searching (SES) in the remainder of the thesis.

Initially, I speculate that the RBC at the equilibrium configuration should be nearly 'flat' with the current beams' configuration. Therefore, I start to displace the cell along the

x-direction, keeping all other degrees of freedom fixed (y = z = 0 μm, Φ=90° and Θ=0°).

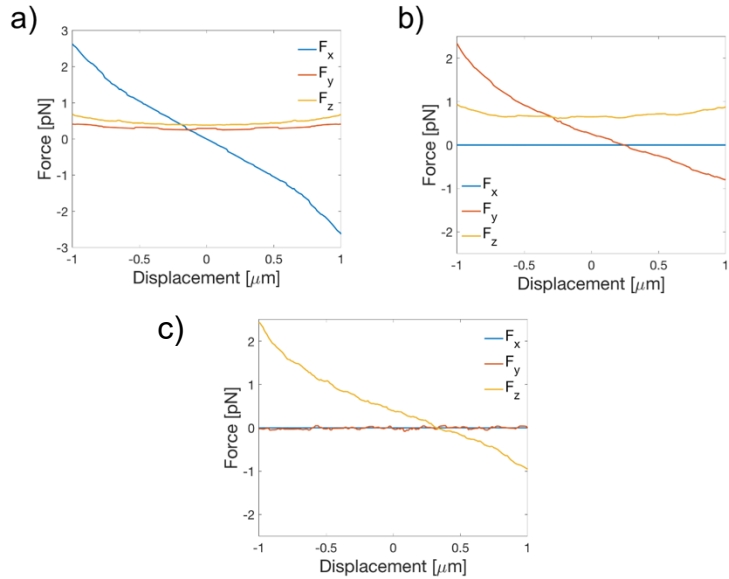

Figure 4.4. Force-displacements curves for cell displacements along the x-direction (a), y-direction (b) and the z-direction (c)

Figure 4.4-a shows the force-displacements curve along the x-direction. Here $F_x(x)$ decreases linearly over the entire displacements interval and clearly shows a spring-like behaviour for x_{eq} = 0 μm, suggesting the cell confinement along this direction. The power normalised trap stiffness is k_x~0.14 pN·μm^{-1}·mW^{-1}. However, forces are present along the transverse directions ($F_y(x)$≠0 and $F_z(x)$≠0). $F_z(x)$ can be easily associated with the scattering forces generated by the

three beams. On the contrary, $F_y(x)$ is due to the gradient component of the optical force generated by the asymmetric light distribution, suggesting that the cell is drawn towards beam 1.

Successively, the cell is placed at x_{eq} (with z = 0, Φ = 90° and Θ = 0°) and the force-displacements curve is calculated for the cell's displacements along the y-direction, Figure 4.4-b. The RBC trapping along this direction is demonstrated by the form of $F_y(y)$ which vanishes with negative slope at y_{eq} = +0.252 μm and the force constant is k_y~0.068 pN·μm^{-1}·mW^{-1}. On the contrary, $F_x(y)$ is always 0, implying that the cell is located at the equilibrium position along the x-direction. $F_z(y)$ is always positive, and again the scattering force is responsible for this trend.

Lastly, using x_{eq} and y_{eq}, the force-displacements curve for displacements along the z-axis is calculated, Figure 4.4-c. Here it can be seen that the cell experiences a restoring force along the z-direction that pushes back the cell at z_{eq} = +0.325 μm. By the linear fit of the approximately linear portion of the graph, the power normalised trap stiffness is k_z~0.08 pN·μm^{-1}·mW^{-1}.

To better comprehend the optical forces generated by the current beams' configuration in the direction transverse to the optical axis, a force-field is simulated in an x-y plane

placed at z_{eq} = +0.325 μm, Figure 4.5. The force map suggests that the equilibrium position is on the x-axis but slightly shifted towards +$\hat{y}$. The black arrows show that the optical forces are always directed towards the equilibrium position, suggesting an effective optical trapping of the RBC.

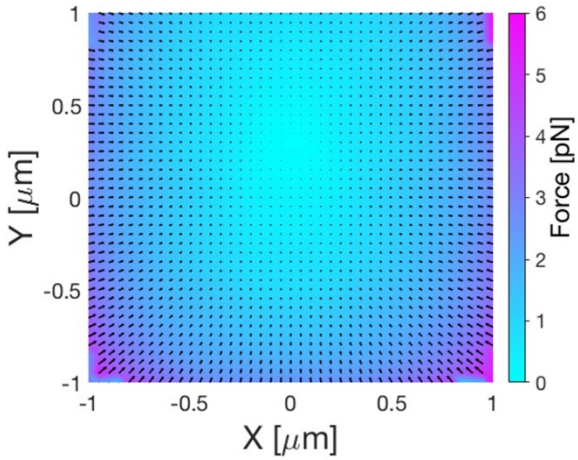

Figure 4.5. Force-field map in an x-y plane placed at z = z_{eq} = +0.325 μm. The black arrows indicate the forces' direction that points towards the equilibrium position located at x_{eq}=0 and y_{eq}=+0.253 μm. The colour map shows the magnitude of the force.

Subsequently, I analyse the orientational confinement of the RBC. Figure 4.6 shows the optical torques acting on the RBC trapped by three beams arranged as depicted in Figure 4.3 as a function of the angle of rotation around the x-axis (α), y-axis (β) and z-axis (γ), in -a, -b and -c respectively.

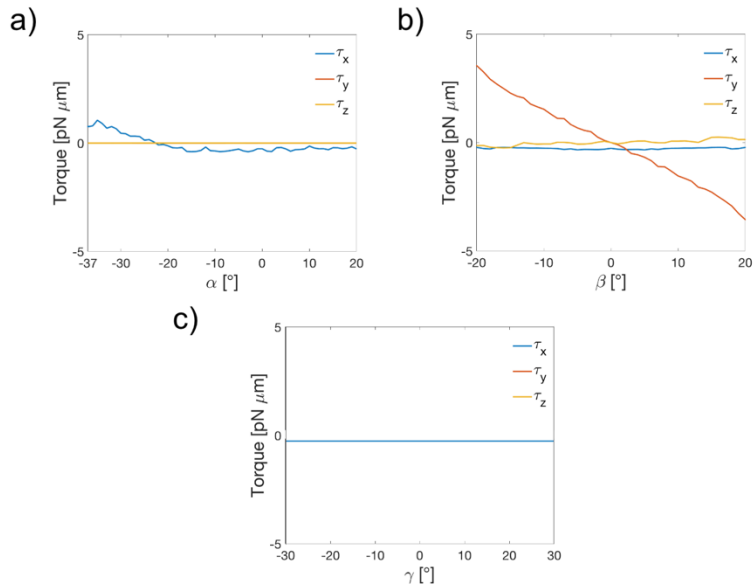

Figure 4.6. Optical torques acting on the cell for rotation around x-direction (a), y-direction (b) and z-direction (c), for the beams' configuration shown in Figure 4.3.

Initially, the cell is placed at x_{eq}, y_{eq}, z_{eq} and then is rotated from the flat configuration (α = 0°) with steps of 1° around an axis passing through the centre of the cell and parallel to the x-axis, Figure 4.6-a. Here it can be seen that no torque component acts along the y- and z-direction ($\tau_y(\alpha)$ = $\tau_z(\alpha)$ = 0). On the contrary, $\tau_x(\alpha)$ shows a spring-like behaviour when α = -22° (k_α~0.233 pN·μm·rad^{-1}·mW^{-1}), which corresponds to Θ=90° and Φ=68°. Importantly, the cell is tilted in the same direction of beam 1, and this suggests

that beam 1 can be used to tilt the cell along a specific direction.

Figure 4.6-b shows the torques for rotation around the y-axis. Here $\tau_y(\beta)$ shows a clear spring-like behaviour when β=0° ('flat' configuration), suggesting the effective orientational trapping of the RBC, and a torque constant k_β~0.585 pN·μm·rad^{-1}·mW^{-1}. On the contrary, no optical torques arise for cell rotation around the z-direction, Figure 4.6-c. Therefore, an RBC is spatially and rotationally confined within a triple-beam OT with the current beams' arrangement with the equilibrium configuration shown in Figure 4.7-a-c.

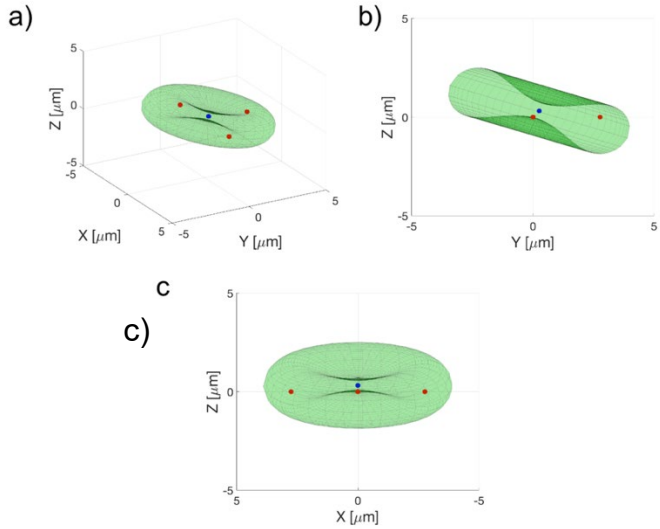

Figure 4.7. a) 3D rendering of the equilibrium configuration of an RBC optically trapped by three focused laser beams arranged as depicted in Figure 4.3, and projection on the y-z plane (b) and x-z plane (c). The blue

dot represents the centre of mass of the cell, while the red dots indicate the foci of the three beams.

Intuitively, by placing beam 1 in a diametrically opposite position ($\zeta = 270°$), the equilibrium configuration of the RBC should be reversed (shifted towards -$\hat{y}$ and tilted toward the same direction).

Figure 4.8-a shows the configuration of the beams under consideration. By performing the same investigation made previously in this paragraph for the new beams' configuration emerges that the force-displacements curve along the x- and z −direction do not change. On the contrary, y_{eq} is shifted at y_{eq} = -0.252 μm. Another exciting variation in respect to the previous case is observed for the rotation around x. The rotational equilibrium is found for a cell tilted at α = 22° ($\Theta = 270°$, $\Phi = 68°$), and thus the RBC is tilted towards beam 1, Figure 4.8-c. On the other hand, none of the remaining possible rotations shows any variation in respect to the previous case. Thus, if beam 1 is positioned at ζ = 270°, the equilibrium configuration is reached for a cell shifted and tilted in exactly the opposite direction in respect to the previous case, Figure 4.8-d-e-f. The values extrapolated from the previous simulation are reported in Table 4.1 for a direct comparison.

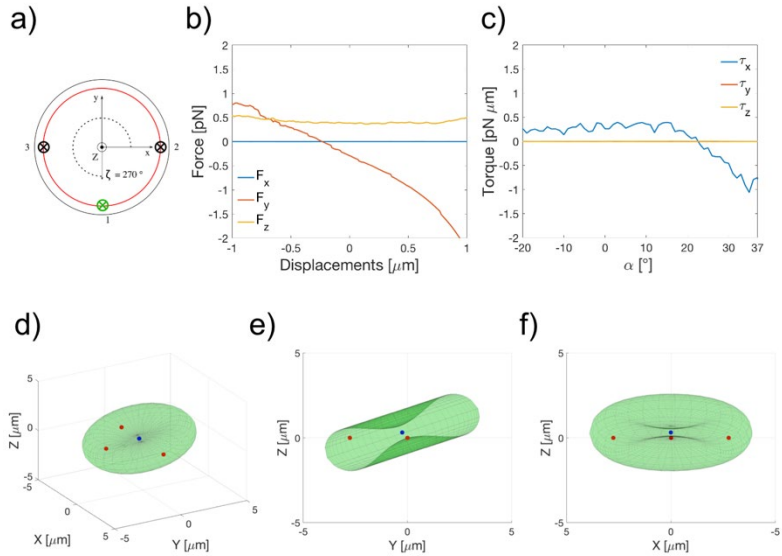

Figure 4.8. Equilibrium configuration for the alternative beams' configuration. a) Beam 1 is positioned in a position diametrically opposite to that represented in Figure 4.3. b) Force-displacements curve for a cell translated along the y-direction with the beam configuration presented in (a). c) Optical torque-rotation for rotation around the x-axis and the beams' configuration presented in (a). d-e-f) Equilibrium configuration of the RBC with the arrangement of the beam is shown in (a).

Following the same reasoning of the above analysis, it seems possible to control the RBC orientation by simply placing beam 1 in any other angular position along the red circle that defines the diameter where the RBC is thickest. If this is true, the RBC can be deliberately oriented and tilted along each possible ζ, or at least in some intervals of ζ.

Figure 4.9-a shows a third possible beams' configuration, and in Figure 4.9-b and -c are shown the force-displacements curves for cell translation along the x- and y-direction, respectively. It is immediately evident that the beams' configuration strongly influences the optical forces and, therefore, the equilibrium point. However, following the investigation's scheme adopted so far, it is not trivial to identify an equilibrium position along the x- and y-direction.

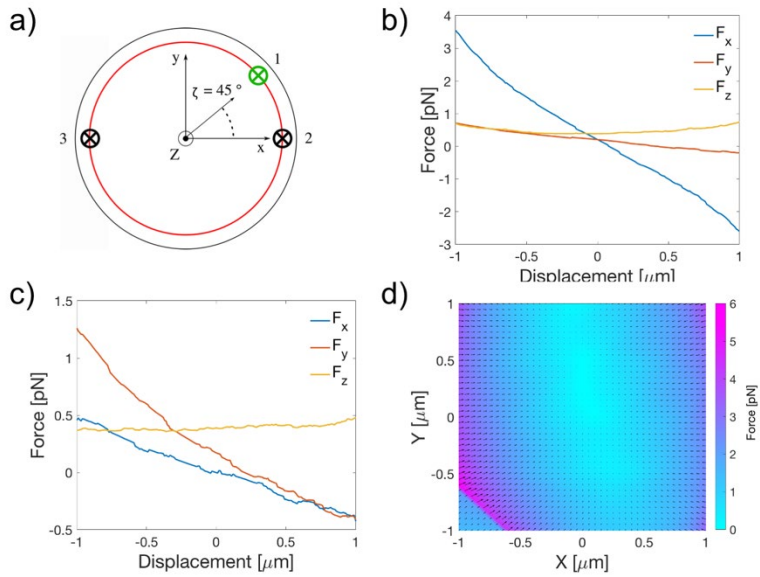

Figure 4.9. a) Alternative beam configuration, and the force-displacements curve along x-direction (b) and y-direction (c). d) Force-map for an RBC on the x-y plane for the configuration of the beams shown in (a).

The identification of the equilibrium via SES would require several reiterations along each direction, resulting in a very

complicated and time-consuming task, if possible at all. This issue is even more clearly visualised by a force map on the x-y plane, Figure 4.9-d. Here it can be seen that the light gradient creates a very complex force-field, and non-negligible optical forces act simultaneously along the x- *and* y-direction for a specific cell location. A possible solution is to simulate the RBC dynamics within the force field generated by the three beams until the RBC configuration stabilises at a precise location and orientation. With such an approach, it is possible to overcome the limits posed by the static equilibrium searching since the RBC equilibrium position and orientation do not have to be searched iteratively. Therefore any possible position of beam 1 (any ζ) can be analysed.

	ζ_{90}	ζ_{270}
x_{eq} (μm)	0	0
y_{eq} (μm)	0.252	-0.252
z_{eq} (μm)	0.325	0.325
k_x (pN·μm^{-1}·mW^{-1})	0.140	0.140
k_y(pN·μm^{-1}·mW^{-1})	0.068	0.068
k_z(pN·μm^{-1}·mW^{-1})	0.080	0.080
α_{eq} (°)	-22	22

$\boldsymbol{\beta_{eq}}$ (°)	0	0
$\boldsymbol{\gamma_{eq}}$ (°)	0	0
$\boldsymbol{k_{\alpha}}$ (pN·µm·rad^{-1}·mW^{-1})	0.233	0.233
$\boldsymbol{k_{\beta}}$ (pN·µm·rad^{-1}·mW^{-1})	0.585	0.585
$\boldsymbol{k_{\gamma}}$ (pN·µm·rad^{-1}·mW^{-1})	0	0

Table 4-1. Equilibrium position and orientation and trap stiffnesses for the beams' configuration ζ_{90} and ζ_{270}.

4.3.2. Dynamic equilibrium searching

In Chapter 2, I introduced how it is possible to simulate the Brownian dynamics of a spherical particle when confined by an optical tweezer. Conversely to spherical particles, non-spherical micron-sized objects undergoes coupled roto-translation while optically trapped.[8,9] For this reason, the theory used in the simulation must be modified to account for this coupling. In the next section, I detail the theory useful for simulating the Brownian motion of a non-spherical particle in a force field.

4.3.2.1. Brownian motion of non-spherical particles in a force field

4.3.2.1.1. Diffusion tensor

The erratic Brownian motion of a non-spherical particle is influenced by the fluid's resistance, the thermal noise, and the external deterministic forces exerted by the optical trap.[9,10] Importantly, for a non-spherical object, a single scalar diffusion coefficient is not enough to describe the statistics of the random motion. It is indeed necessary a 6 x 6 diffusion tensor ($\boldsymbol{D}$), which depends on the particle shape and orientation:

$$\boldsymbol{D} = \begin{bmatrix} \boldsymbol{D}_{tt} & \boldsymbol{D}_{tr} \\ \boldsymbol{D}_{rt} & \boldsymbol{D}_{rr} \end{bmatrix} \qquad 4.1$$

where $\boldsymbol{D_{tt}}$, $\boldsymbol{D_{rr}}$ and $\boldsymbol{D_{rt}} = \boldsymbol{D_{tr}}^{\boldsymbol{T}}$ are 3 x 3 blocks and the subscripts '*r*' and '*t*' refer to the particle's rotational and translational degree of freedom, respectively. In each 3 x 3 block, the diagonal terms indicate the diffusion coefficients along a specific direction, while the off-diagonal terms indicate the cross-diffusional terms (i.e. coupled motion).

Although analytical expression for $\boldsymbol{D}$ exists for simple shapes, like spherical particle, ellipsoid or cylinder, the RBC morphology is more complex and require numerical methods for the determination of $\boldsymbol{D}$. In the present work, I used the

bead model technique developed by De La Torre *et al.*, exploiting the widely used software winHYDRO++.[11,12] In the bead model, a series of spheres are used to approximate the size and the total volume of the RBC. The computer program then uses the model geometry to calculates the hydrodynamic resistance of the particle of interest, where the translational, rotational, and the coupled terms (roto-translation) are encoded in 6 x 6 friction tensor ($\boldsymbol{\Xi}$):[13]

$$\boldsymbol{\Xi} = \begin{bmatrix} \boldsymbol{\Xi}_{tt} & \boldsymbol{\Xi}_{tr} \\ \boldsymbol{\Xi}_{rt} & \boldsymbol{\Xi}_{rr} \end{bmatrix} \qquad 4.2$$

where $\boldsymbol{\Xi_{tt}}$, $\boldsymbol{\Xi_{rr}}$ and $\boldsymbol{\Xi_{rt}} = \boldsymbol{\Xi_{tr}}^{\boldsymbol{T}}$ are 3 x 3 blocks and the subscripts '*r*' and '*t*' refer to the particle's rotational and translational degree of freedom, respectively. Given additional information about the solvent physical properties (e.g. fluid viscosity, and the temperature) the software obtains the diffusion tensor $\boldsymbol{D}$ via the generalised Einstein relationship:[13]

$$\boldsymbol{D} = k_b T \boldsymbol{\Xi}^{-1} \qquad 4.3$$

where k_b is the Boltzmann constant, and T is the temperature of the system.

In the present study, the bead model is constructed in a strict sense, where the volume of the RBC is filled with

spheres of equal sizes. On the one hand, many spheres of very small diameters can be used to approximate the shape of the RBC, but this has a high computational cost. Still, the results of the computation are not significantly more accurate. On the other hand, a smaller number of spheres with a larger diameter can approximate the RBC's volume, with a smaller computational cost but with a significant decrement in the approximation of the friction tensor. In the present work, the optimal parameters are obtained if 657 spheres with a radius of 0.25 μm are used, Figure 4.10.

In the present case, the centre of diffusion of the particle coincides with the centre of mass of the particle, and the numerical output for the diffusion tensor reads:

$$\mathbf{D}_{tt} = \begin{bmatrix} 7.427 \times 10^{-14} & -4.383 \times 10^{-20} & 6.234 \times 10^{-21} \\ 5.933 \times .10^{-21} & 7.427 \times 10^{-14} & 5.991 \times 10^{-21} \\ -8.744 \times 10^{-20} & -5.425 \times 10^{-19} & 6.283 \times 10^{-14} \end{bmatrix} 4.4$$

$\mathbf{D}_{\mathrm{rt}}$=

$$\mathbf{D}_{\mathrm{tr}}{}^{\mathrm{T}} = \begin{bmatrix} -6.178 \times 10^{-15} & -2.520 \times 10^{-15} & -1.748 \times 10^{-15} \\ -2.520 \times 10^{-15} & 8.853 \times 10^{-16} & -2.724 \times 10^{-15} \\ -1.748 \times 10^{-15} & -2.724 \times 10^{-15} & -2.199 \times 10^{-16} \end{bmatrix} 4.5$$

$$\mathbf{D}_{\mathrm{rr}} = \begin{bmatrix} 4.041 \times 10^{-3} & 3.627 \times 10^{-11} & 1.056 \times 10^{-10} \\ 1.043 \times 10^{-9} & 4.041 \times 10^{-3} & -7.846 \times 10^{-10} \\ 1.018 \times 10^{-10} & 3.169 \times 10^{-10} & 3.362 \times 10^{-3} \end{bmatrix} 4.6$$

where the units are $m^2 \cdot s^{-1}$, $rad \cdot m \cdot s^{-1}$, and $rad^2 \cdot s^{-1}$ respectively.

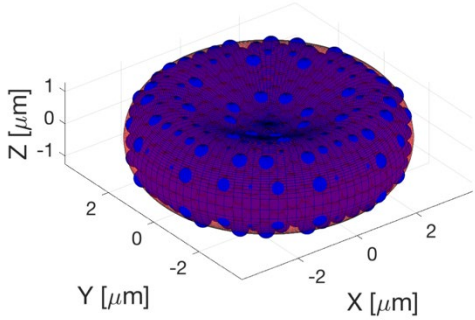

Figure 4.10. Bead model for the RBC useful to calculate the diffusion tensor $\boldsymbol{D}$ winHYDRO++.

The diagonal terms of $\boldsymbol{D}_{tt}$ give the diffusion coefficient along a specific direction (i.e. x, y, z) and are several order of magnitude larger than the off-diagonal terms that provide the cross-diffusional terms. Similarly, the terms along the diagonal of $\boldsymbol{D}_{rr}$ encode for the rotational diffusion coefficients around a specific axis (i.e. x, y, z), and even in this case, these are several order of magnitude larger than the coupled terms.

4.3.2.1.2. Brownian motion in a force field

In this section, I describe the finite difference scheme used for the simulation of the dynamics of the RBC, which is based on the works of M. X. Fernandes and collaborators.[9] Two reference frames are defined: a particle reference frame Σ_p, which origin coincides with particle's centre of mass (CM)

and the centre of diffusion (CD), and a laboratory reference frame Σ_l that is centred in (0,0,0) and which axes are oriented along $\hat{\boldsymbol{x}}$, $\hat{\boldsymbol{y}}$ and $\hat{\boldsymbol{z}}$, Figure 4.2-a. At time t, the RBC's CD is located at $\boldsymbol{r}_{CD}(t) = [x_{CD}(t), y_{CD}(t), z_{CD}(t)]$. The cell orientation is described by the direction cosines $\alpha_1(t)$, $\beta_1(t)$ and $\gamma_1(t)$ defined with respect to the particle unit vector $\hat{\boldsymbol{x}}_p(t) = \left[\hat{x}_{p,x}(t), \hat{x}_{p,y}(t), \hat{x}_{p,z}(t)\right]$, $\hat{\boldsymbol{y}}_p(t) = \left[\hat{y}_{p,x}(t), \hat{y}_{p,y}(t), \hat{y}_{p,z}(t)\right]$, $\hat{\boldsymbol{z}}_p(t) = \left[\hat{z}_{p,x}(t), \hat{z}_{p,y}(t), \hat{z}_{p,z}(t)\right]$, Figure 4.2-a. $\boldsymbol{D}$ is obtained in the particle reference frame, that is centred at $\boldsymbol{r}_{CD}(t)$ and the axes are oriented along $\hat{\boldsymbol{x}}_p$, $\hat{\boldsymbol{y}}_p$ and $\hat{\boldsymbol{z}}_p$.

To simulate the free diffusion of an arbitrarily shaped particle from time *t* to the time step *t*+Δt, initially, one has to calculate the increment of the particle position and orientation in $\Sigma_p(t)$:[9]

$$\begin{bmatrix} \Delta x_p \\ \Delta y_p \\ \Delta z_p \\ \Delta \alpha_p \\ \Delta \beta_p \\ \Delta \gamma_p \end{bmatrix} = \sqrt{2\Delta t} \begin{bmatrix} w_x \\ w_y \\ w_z \\ w_\alpha \\ w_\beta \\ w_\gamma \end{bmatrix} \qquad 4.7$$

where $\left[w_x, w_y, w_z, w_\alpha, w_\beta, w_\gamma\right]^T$ are random numbers obtained from a multivariate normal distribution with zero mean and covariance $\boldsymbol{D}$. Successively, the increments of the particle position calculated in Σ_p has to be transformed to Σ_l. This

transformation, rotation around CD, is given by the transformation matrix:

$$\boldsymbol{M}_{\Sigma_p \to \Sigma_l}(t) = \begin{bmatrix} \hat{x}_{p,x} & \hat{y}_{p,x} & \hat{z}_{p,x} \\ \hat{x}_{p,y} & \hat{y}_{p,y} & \hat{z}_{p,y} \\ \hat{x}_{p,z} & \hat{y}_{p,z} & \hat{z}_{p,z} \end{bmatrix}. \quad 4.8$$

Therefore, the finite difference equation to update the particle position in Σ_l is:

$$\begin{bmatrix} x_{CM}(t+\Delta t) \\ y_{CM}(t+\Delta t) \\ z_{CM}(t+\Delta t) \end{bmatrix} = \begin{bmatrix} x_{CM}(t) \\ y_{CM}(t) \\ z_{CM}(t) \end{bmatrix} + \boldsymbol{M}_{\Sigma_p \to \Sigma_l}(t) \begin{bmatrix} \Delta x_p \\ \Delta y_p \\ \Delta z_p \end{bmatrix}. \quad 4.9$$

Once the new particle position is calculated, one has to update the particle orientation from $\Sigma_p(t)$ to $\Sigma_l(t)$, which is effectively a rotation of the particle unit vectors. This rotation is expressed in Σ_p by the rotation matrix:

$$\boldsymbol{R}_p(\Delta\alpha_p, \Delta\beta_p, \Delta\gamma_p) = \boldsymbol{R}_{p,x}(\Delta\alpha_p)\boldsymbol{R}_{p.y}(\Delta\beta_p)\boldsymbol{R}_{p,z}(\Delta\gamma_p) \quad 4.10$$

where:

$$\boldsymbol{R}_{p,x}(\Delta\alpha_p) = \begin{bmatrix} 1 & 0 & 0 \\ 0 & \cos(\Delta\alpha_p) & -\sin(\Delta\alpha_p) \\ 0 & \sin(\Delta\alpha_p) & \cos(\Delta\alpha_p) \end{bmatrix}$$

$$\boldsymbol{R}_{p,y}(\Delta\beta_p) = \begin{bmatrix} cos(\Delta\beta_p) & 0 & sin(\Delta\beta_p) \\ 0 & 1 & 0 \\ -sin(\Delta\beta_p) & 0 & cos(\Delta\beta_p) \end{bmatrix} \qquad 4.11$$

$$\boldsymbol{R}_{p,z}(\Delta\gamma_p) = \begin{bmatrix} \cos(\Delta\gamma_p) & -\sin(\Delta\gamma_p) & 0 \\ \sin(\Delta\gamma_p) & \cos(\Delta\gamma_p) & 0 \\ 0 & 0 & 1 \end{bmatrix}.$$

Transforming this rotation matrix to Σ_l, we obtain the unit vectors representing the orientation of the particle at the end of the time step:

$$\left[\hat{\boldsymbol{x}}_p(t+\Delta t), \hat{\boldsymbol{y}}_p(t+\Delta t), \hat{\boldsymbol{z}}_p(t+\Delta t)\right] = \left[\hat{\boldsymbol{x}}_p(t), \hat{\boldsymbol{y}}_p(t), \hat{\boldsymbol{z}}_p(t)\right]\boldsymbol{R}_p(\Delta\alpha_p, \Delta\beta_p, \Delta\gamma_p). \qquad 4.12$$

As the last step, the rotation matrix has to be updated:

$$\boldsymbol{M}_{\Sigma_p\to\Sigma_l}(t+\Delta t) = \boldsymbol{M}_{\Sigma_p\to\Sigma_l}(t)\boldsymbol{R}_p(\Delta\alpha_p, \Delta\beta_p, \Delta\gamma_p). \qquad 4.13$$

However, in the current situation, we must also account for the optical forces ($\boldsymbol{F}$) and torques ($\boldsymbol{\tau}$) exerted by the triple-beams optical trap on the centre of mass of the RBC. Therefore, taking into account $\boldsymbol{F}$ and $\boldsymbol{\tau}$, the increments of the particle orientation and position in Σ_p are:

$$\begin{bmatrix} \Delta x_p \\ \Delta y_p \\ \Delta z_p \\ \Delta \alpha_p \\ \Delta \beta_p \\ \Delta \gamma_p \end{bmatrix} = \frac{\boldsymbol{D}}{k_B T} \Delta t \begin{bmatrix} F_{x,p} \\ F_{y,p} \\ F_{z,p} \\ \tau_{x,p} \\ \tau_{y,p} \\ \tau_{z,p} \end{bmatrix} + \sqrt{2\Delta t} \begin{bmatrix} w_x \\ w_y \\ w_z \\ w_\alpha \\ w_\beta \\ w_\gamma \end{bmatrix} \qquad 4.14$$

which then need to be transformed back into Σ_l. However, $\boldsymbol{F}$ and $\boldsymbol{\tau}$ are calculated in Σ_l, and therefore they must be transformed to Σ_p via the rotation matrix $\boldsymbol{M}_{\Sigma_p \to \Sigma_l}{}^T$.

The present finite difference scheme is combined with the code to calculate the optical forces and torques acting on the RBC (see chapter 4). It is then integrated with the computer software Optical Tweezer in Geometrical Optics (OTGO)[14] to perform the numerical simulation.

4.3.2.2. Numerical computation

The particle dynamics is simulated for the beams' parameters reported in section 4.2 and using a time step (Δt) of 0.001 s. In every simulation, the cell is initially positioned in its 'flat' configuration ($\Phi = 90°$ and Θ = 0°) and centred in (0,0,0), since the final configuration is not known *a priori*. The final position and orientation are given as the average position and orientation ± the standard deviation of the last second of the simulation.

Even if not extensively analysed, I estimate Δt from the trap constants calculated in chapter 3, and from the diffusion properties of a healthy RBC. The typical time scale on which the restoring force acts is given by $\omega_{OT} = \gamma/k$, while the momentum relaxation time is given by $\omega_m = m/\gamma$. As extensively discussed in chapter 2, Δt must fall in between these two characteristic time scales ($\omega_{OT} \gg \Delta t \gg \omega_m$) to assure numerical stability. From the diffusion tensor $\boldsymbol{D}$, one can extract the diffusion properties of the RBC along a specific direction (D_i), then through the fluctuation dissipation theorem one can obtain γ_i. For example, for the x-direction one obtains $\gamma_x = k_b T/D_x \sim 5 \cdot 10^{-8}$ kg·s-1. Therefore, considering a $k_x \sim 1.6$ pN·μm^{-1}, one obtains $\omega_{OT} \sim 3 \cdot 10^{-2}$ s. On the other hand, given a mass of ~1·10^{-11} kg for a typical healthy RBC, one obtain $\omega_m \sim 4 \cdot 10^{-4}$ s. A similar estimation can be made for the other directions, and contemplating the magnitude of the other terms in $\boldsymbol{D}$, a Δt=0.001 s should assure numerical stability.

The time evolution of the RBC's position is followed storing the co-ordinates of the RBC's CM in Σ_l after each time step, while the orientation of the cell is recorded as the polar (Φ) and the azimuthal orientation (θ) encoded by $\hat{\boldsymbol{z}}_p$, Figure 4.2-a. With these two angles, and the position of the centre of mass of the cell, the position and orientation of the RBC are entirely defined. Initially, I do not consider the possible

cell's spinning about $\hat{\boldsymbol{z}}_{p,z}$ even though the cell could spin around its axis of symmetry ($\hat{\boldsymbol{z}}_{p,z}$) when beam 1 is close enough to beam 2 or 3, Figure 4.2-a and -b.

As a first numerical experiment, I perform the numerical simulation for the beams' configuration shown in Figure 4.3 to compare the output of the dynamic simulation with the results obtained with the SES.

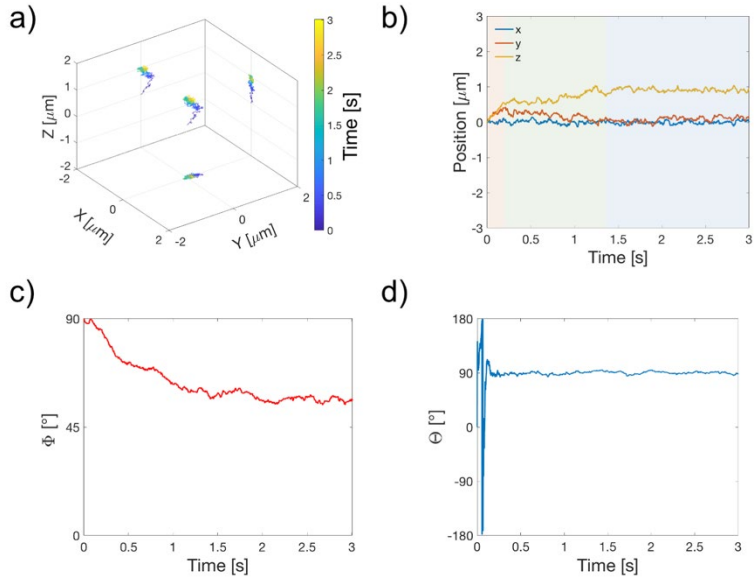

Figure 4.11. a) 3D trajectories of the RBC CM as a function of time, and b) each Cartesian co-ordinates as a function of the simulation time. c) Polar and azimuthal (d) orientation of the RBC as a function of time.

Figure 4.11-a shows the three-dimensional trajectories of the centre of mass of the RBC trapped by a

triple-beams optical trap, while each Cartesian co-ordinate is plotted as a function of the simulation time in Figure 4.11-b. As soon as the light beams are turned on (t = 0 s), the cell starts to migrate towards +$\hat{\boldsymbol{z}}$ guided by $\boldsymbol{F_s}$. Simultaneously, the cell starts to re-orient itself within the optical trap, Figure 4.11-c and -d. This re-orientation is accompanied by a motion towards +$\hat{\boldsymbol{y}}$ under the pulling action of $\boldsymbol{F_g}$. Conversely, the RBC does not undergo substantial motion along the x-direction over the entire simulation time, and this is completely expected, Figure 4.11-a and -b.

Interestingly, the orientational dynamics seems to have a two-time scale. Θ seems to stabilise within 0.25 s along the same direction of the beam 1 (Θ = 90.355° ± 1.603°), but it requires ~1.5 s to stabilise along the final polar orientation (Φ = 56.379° ± 0.974°), Figure 4.11-c and -d. After the initial transient period, the cell stabilises at its final translational and rotational equilibrium within 2 s.

In Table 4-1 are summarised the values of the equilibrium position and orientation of the RBC extracted from the static equilibrium searching and the dynamic equilibrium searching. Overall, the values are in good agreement. The equilibrium is for a cell slightly shifted towards +$\hat{\boldsymbol{y}}$ and +$\hat{\boldsymbol{z}}$, while x_{eq} is zero in both cases. For what concern the rotational equilibrium, the cell is slightly tilted towards beam 1.

Nevertheless, from a closer inspection, some differences arise, precisely for Φ, z_{eq} and y_{eq}. These differences are due to the essentially different methods to identify the equilibrium position. In theory, both methods should converge to the same equilibrium values. However, the static method analyses one co-ordinate at a time, leaving all other degrees of freedom with a predetermined and fixed value during the investigation. Therefore, one would need to iterate a certain number of times the entire procedure before reaching the final equilibrium configuration. This reiteration process could be really laborious or practically impossible when the final equilibrium configuration is not known *a priori*, as for the beams' configuration shown in Figure 4.9-a. On the contrary, the dynamic method is faster (~3-4 hours) and can explore simultaneously every degree of freedom until the particle reaches the final equilibrium configuration.

Degree of freedom	Static searching	Dynamic searching
x	0 μm	0.001 ± 0.047 μm
y	0.252 μm	0.112 ± 0.051 μm
z	0.326 μm	0.901 ± 0.043 μm
Φ	68. 010°	56.379° ± 0.974°
θ	90.000°	90°±0.135°

Table 4-2. Comparison of the equilibrium position and orientation obtained with the static equilibrium searching and the dynamic equilibrium searching.

As a further proof of the current dynamic searching method, I also carry out the dynamic searching for the alternative beams' configuration shown in Figure 4.8-a.

In Figure 4.12 are directly compared the simulations results for beam 1 located at $\zeta = 90°$ and $\zeta = 270°$, which corresponds to the beam configuration used for the static equilibrium searching shown in section 4.3.1. In the two conditions beam 1 is placed in diametrically opposite position along the y-axis while beam 2 and 3 are placed on the x-axis, Figure 4.12-a.

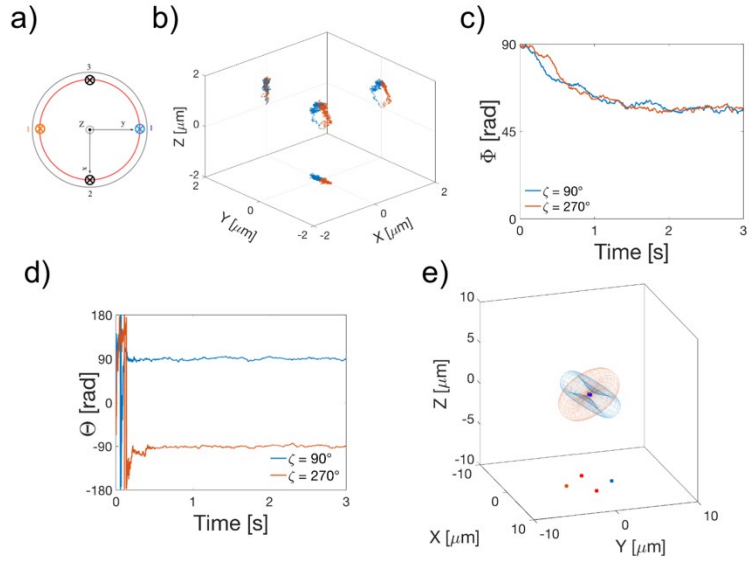

Figure 4.12. a) Schematic illustration of the alternative beams' configuration investigated via the dynamic equilibrium searching. b) 3D trajectories of the RBC's CM for the beams' configuration shown in (a). c, d) Polar and azimuthal orientation of the RBC as a function of time for the

beams' configuration shown in (a). e) 3D representation of the equilibrium configuration of the RBC obtained with the dynamics equilibrium searching for the beams' configuration shown in (a). The small dot represents the location of the beams' foci.

Figure 4.12-b shows the three-dimensional trajectories of the centre of mass of the cell for the two cases. In both cases, the cell starts to rapidly migrate in the direction of beam 1 while translating towards $+\hat{\boldsymbol{z}}$ because of $\boldsymbol{F_s}$. Conversely, the trajectories fluctuate around 0 μm along the x-direction. Importantly, at equilibrium, the cell is just slightly shifted along the y-direction according to the position of beam 1, Figure 4.12-b.

Independently from the position of beam 1, the cell finds its rotational equilibrium when the plane is rotated of about 56° around the x-axis, Figure 4.12-c. However, in the two cases, the cell is tilted in the opposite direction, Figure 4.12-d and e. Here can be seen the different effects of the position of beam 1 on the cell tilting. If beam 1 is positioned in two diametrically opposite directions along the y-axis, the cell orients itself with the very same polar angle but along the opposite direction.

It appears, therefore, to be possible to control the orientation and the position of the cell by varying the angular position of beam 1. From symmetry arguments, the effect of different locations of beam 1 can be understood restricting ζ

in the interval $[0°, 90°]$, Figure 4.13-a. Moreover, since I am particularly interested in configurations alternative to the 'flat' or 'folded' one (or to a transition between the two), it is also possible to exclude every position of beam 1 that is too close to beam 2, which should induce a folded configuration. Thus, the position of beam 1 can be restricted to $15° \leq \zeta \leq 90°$.

To analyse the effect of the position of beam 1 on the RBC's configuration, I sample ζ every 15°. For each angular position of beam 1, I carried out the dynamics equilibrium searching.

Figure 4.13-b shows the 3D trajectories of the RBC's CM obtained from the simulations carried out for different ζ. From the trajectories, it is evident that the position of beam 1 influences the equilibrium position of the RBC. In particular, it seems clear that if beam 1 is close to beam 2 ($\zeta = 15 - 30°$), z_{eq}~ 0 μm. I anticipate that for $\zeta \leq 30°$, the cell is in its 'folded' configuration. Moreover, it is also possible to appreciate that for $\zeta = 15°$, the cell centre of mass seems to be slightly shifted towards -$\hat{\boldsymbol{x}}$. Not surprisingly, both effects are expected, and they are due to a combination of the light intensity distribution and the cell configuration within the trap. In fact, when the cell is in its 'folded' position, the cell's plane is parallel to the direction of propagation of the light beam. In this condition, more light rays strike the biggest faces of the RBC, increasing significantly $\boldsymbol{F}_g$. Simultaneously, $\boldsymbol{F}_s$

decreases appreciably because of the smaller geometrical cross-section of the cell (see chapter 3). However, if ζ increases, this effect is less pronounced since the light rays strike the cell less symmetrically, and for ζ = 30°, z_{eq}~0.5 μm. On the other hand, the shifting along the x-direction is due to the strong gradient in the light intensity along $\hat{\boldsymbol{x}}$, and thus to the pulling effect of $\boldsymbol{F}_g$. Conversely, for the remaining beams' configurations, the effect on the centre of mass of the particle is less pronounced, and all the simulations converge to approximately the same three-dimensional position.

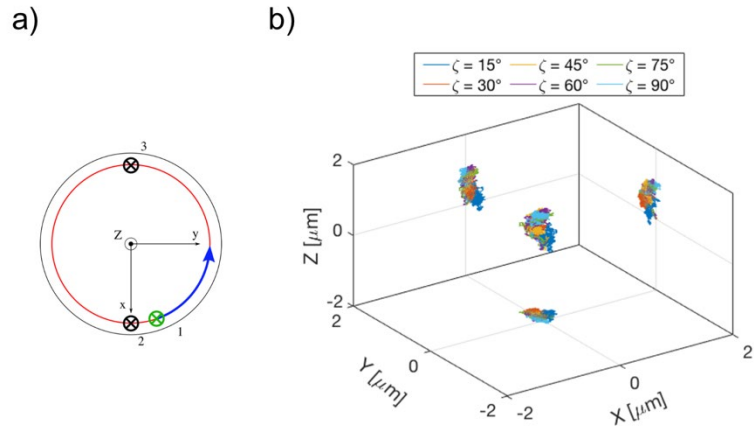

Figure 4.13. a) Schematic depiction of the beams' configuration for variable position of beam 1. b) 3D trajectories obtained from the simulations for different ζ.

Much more interesting is the analysis of the rotational equilibrium. In Figure 4.14-a are shown the polar orientation

(Φ) of the cell as a function of the simulation time for different locations of beam 1 (i.e. various ζ). Here, it is clearly evident that beam 1 strongly influences the final polar orientation of the cell. In every configuration tested, beam 1 induces a clockwise cell rotation around the x-axis, Figure 4.14-c. In particular, as beam 1 is closer to beam 2, the cell tilts more and more until it reaches the 'folded' configuration ($\Phi = 0°$). Analysing the final orientation of the cell in more detail, it is possible to discriminate between three different regions. When beam 1 is in the proximity of beam 2, $\zeta \leq 30°$, the cell is in the 'folded' configuration. If $30° < \zeta < 75°$, the RBC's tilting seems to vary linearly with ζ, from a 'folded-like' configuration to 'flat-like' configuration. The last region is for $\zeta \geq 75°$, where the cell tilting cannot be decreased further, Figure 4.14-a.

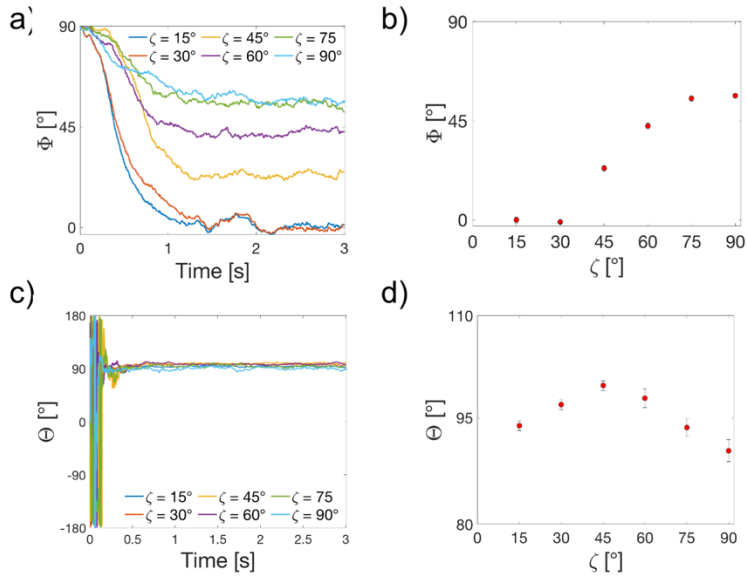

Figure 4.14. a) Polar orientation of the RBC as a function of the simulation time, and average polar orientation of the cell in the last second of simulation (b). c) Azimuthal direction of the cell as a function of time and average azimuthal orientation for the last second of simulation (d). The error bar represents the standard deviation.

To appreciate more this behaviour, I extract the average value of the cell orientation and position and plot them as a function of ζ, Figure 4.14-b. Here the three regions are particularly evident. An initial plateau for $\zeta \leq 30°$, a linear increase for $30° \leq \zeta \leq 75°$ and final plateau for $\zeta > 75°$. Moreover, from Figure 4.14-b is also evident that in every condition, the cell tilts clockwise around the x-axis (towards beam 1). It is also interesting to note the minor effect that the

position of beam 1 has on Θ. In particular, for $\zeta = 45°$ is possible to obtain the highest cell's tilting around the *z*-axis. For every other ζ, the tilting of the RBC around the z-direction decreases towards $\Theta = 90°$.

In Figure 4.15 are depicted the final equilibrium configuration of the RBC in respect to beam 1 position, and the arrows indicate the relation between the cell configuration and the position of beam 1. Here is clearly visible how beam 1 strongly influences the cell tilting over a wide range of possible orientations.

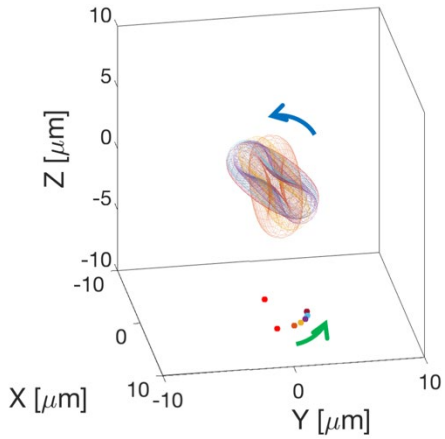

Figure 4.15. Final equilibrium configuration of the RBC for different positions of beam 1. The red dots indicate the projection on the x-y plane of the position of the focal points of beam 2 and beam 3. The coloured dots indicate the position of beam 1. The green arrow shows how beam 1 is translated, while the blue arrow indicates how the cell tilts in response to the position of beam 1.

4.4. Chapter summary

In this chapter, I investigated how a triple-beam optical tweezer can be used to control the orientation and the position of a healthy RBC in its biconcave disk conformation. I used two different approaches for the final equilibrium configuration searching. The static equilibrium searching demonstrated an excellent method to investigate the trapping mechanism if the equilibrium configuration of the cell is known *a priori* or if the trap configuration assumes a simple geometrical configuration. In fact, with few reiterations of such a method, the final equilibrium configuration can be easily identified. However, as the trap configuration increases in complexity, the static equilibrium searching becomes too laborious and could fail to identify the final configuration of the cell. For highly complex traps' configuration, simulating the non-spherical particles' Brownian dynamics was an essential step. The introduction of dynamic equilibrium searching makes possible to identify the final equilibrium position and orientation even in highly complex light distribution patterns.

In conclusion, I theoretically demonstrated the possibility to fine control the position and orientation of a healthy RBC in its biconcave disk conformation using reconfigurable triple-beam optical tweezers. Moreover, the

introduction of a dynamic equilibrium searching method paves the way for experimentalists to verify various hypotheses on the possibility to control the configuration of an RBC for orientational dependent studies.

It must be made it clear that the presented work is purely numerical and that during experiments some differences could arise. Firstly, the red blood cell is approximate as a rigid body which in real world is clearly not. Nevertheless the cell deforms in response to optical pressure, it is unlikely that the deformation induced by low lasers' powers (< 10 mW) could be so consistent to prevent the optical trapping completely. More significant in terms of trapping could be a cell damaged induced by a prolonged trapping with high lasers' power (tens or hundreds of mW). Secondly, the entire set of numerical experiment are tuned on specific RBC morphological properties as discussed extensively in chapter 3. These parameters can be tweaked to accommodate specific conditions. For example, the morphology of the cell can be adjusted to describe the swelling state of a RBC according to the osmolarity of the solution. However, if this is the case the trap architecture needs to be changed accordingly. Additionally, this numerical experiment does not consider anyhow a morphological change in the RBC outline due to a pathological RBC condition. In third place, any trap imperfection (e.g. beam

aberrations) that can be encountered experimentally is not considered. The presence of imperfections would limit the applicability should you attempt trapping in vivo, for example. Therefore, an experimental validation is strictly necessary to confirm the possibility to govern the orientation and the position of the RBC.

4.5. Bibliography

[1] P. H. Jones, O. M. Maragò, G. Volpe, In *Optical Tweezers Principles and applications*; Cambridge University Press: Cambridge, 2015; pp. 19–41.

[2] A. Ashkin, *Phys. Rev. Lett.* **1970**, *24*, 156.

[3] A. Ashkin, J. M. Dziedzic, J. E. Bjorkholm, S. Chu, *Opt. Lett.* **1986**, *11*, 196.

[4] A. Ashkin, J. M. Dziedzic, *Science (80-.).* **1987**, *235*, 1517.

[5] A. Ashkin, J. M. Dziedzic, T. Yamane, *Nature* **1987**, *330*, 769.

[6] T. Avsievich, R. Zhu, A. Popov, A. Bykov, I. Meglinski, *Rev. Phys.* **2020**, *5*.

[7] J. Guck, R. Ananthakrishnan, H. Mahmood, T. J. Moon, C. C. Cunningham, J. Käs, *Biophys. J.* **2001**, *81*, 767.

[8] B. Roy, A. Mondal, S. K. Bera, A. Banerjee, *Soft Matter* **2016**, *12*, 5077.

[9] M. X. Fernandes, J. G. De la Torre, *Biophys. J.* **2002**, *83*, 3039.

[10] P. H. Jones, O. M. Maragò, G. Volpe, In *Optical tweezers principles and applications*; 2015; pp. 188–218.

[11] J. Garcia de la Torre, S. Navarro, M. C. Lopez

Martinez, F. G. Diaz, J. J. Lopez Cascales, *Biophys. J.* **1994**, *67*, 530.

[12] J. G. De La Torre, G. Del Rio Echenique, A. Ortega, *J. Phys. Chem. B* **2007**, *111*, 955.

[13] B. Carrasco, J. G. De La Torre, *Biophys. J.* **1999**, *76*, 3044.

[14] A. Callegari, M. Mijalkov, A. B. Gököz, G. Volpe, *J. Opt. Soc. Am. B* **2015**, *32*, B6.

5. LIGHT-SHEET TWEEZER FOR OPTICAL TRAPPING AND ROTATION OF HEALTHY RED BLOOD CELLS IN THE BICONCAVE DISK CONFORMATION

In this Chapter, I present a theoretical investigation on the possibility of optically trap a healthy erythrocyte with a line tweezer. This section is motivated by a suggestion for using a line optical trap for trapping RBCs for interrogation as they flow through a microfluidic device. A line tweezer should allows the same orientational confinement that ones can obtain with a double-beam optical tweezers, but using only a single beam thanks to the addition of a single and simple optical element (i.e. cylindrical lens).

5.1. Introduction

In 1970 Arthur Askhin first demonstrated how to manipulate micron-sized latex spheres suspended in water through optical pressure.[1] Following the first demonstration of optical trapping, he applied single-beam optical tweezers (see chapter 2 for a detailed description) to manipulate biological particles as bacteria and red blood cells.[2,3]

The basic principles of optical tweezers hang on to the fact that light carries momentum, which can be harvested to manipulate microscopic dielectric particles in solution. A stable optical trapping can be reached when the net force exerted on the particle by the illuminating light is balanced. In its conventional set-up, the optical tweezer uses spherical optics, which produces a point focus. This gives rise to a well-defined point trap where a laser beam, with a Gaussian intensity distribution, is focused to a diffraction-limited spot through a high numerical aperture objective[4], Figure 5.1-a. In this condition, a gradient in the light intensity distribution is created along each spatial direction, and the gradient force ($\mathbf{F}_g$) confines the microparticle in the proximity of the beam focus. The trapping mechanism is considerably different if a Gaussian beam is focused over a line (line-traps) rather than a single point.

In one of the first implementations of line-traps researchers proposed the use of a rectangular aperture that blocks the light beam exiting the laser resonator selectively.[5] However, this methodology presents technical difficulties and a significant loss of the initial laser power (greater than 50%). Others have formed line tweezers by rapidly scanning a point like optical trap,[6,7] or holography.[8] Interestingly, Dasgupta and collaborators exploit a simple set-up initially used for fluorescence microscopy,[9] the well-known light-sheet

fluorescence microscopy, to produce a line-trap.[10] Importantly, compared to other methodologies, the proposed set-up require only a single cylindrical lens to create the line-trap.

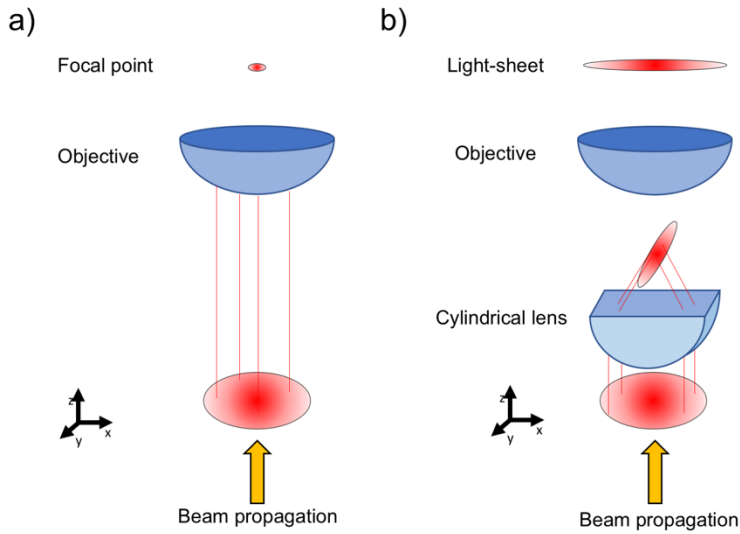

Figure 5.1. Schematic diagram of a single-beam optical tweezer (a), and a light-sheet optical tweezer (b).

Line-traps are well understood in rectangular co-ordinates systems.[11] The diffraction-limited light 'line' is taken along the xz-plane with the x-axis and the z-axis as the light 'line' axis and the beam propagation direction. Initially, the incoming beam is focused by the cylindrical lens along a line on the y-axis. The objective lens is placed at the focus of the cylindrical lens. The field at the back aperture of the

objective lens undergoes a Fourier transform, forming a diffraction-limited line along the x-axis at its focus, Figure 5.1-b. In this condition, a strong light intensity gradient is present only along two directions ($\hat{\mathbf{y}}$ and $\hat{\mathbf{z}}$). Therefore, a particle is completely free to move around the direction over which the incoming beam is focused (i.e. $\hat{\mathbf{x}}$) as long as it is smaller than the extent of the line along x-direction.

Objects that deviates from the simple spherical shape, like ellipsoid or cylinder, tend to align with the beam propagation direction because of the optical torque generated by the incoming beam (see chapter 2). This is the case for biological particles like healthy red blood cells (RBCs) trapped by a single- or double-beam optical tweezer (see chapter 3). In line-tweezer, the same remains true. This behaviour can be exploited further to achieve a controlled rotation of the object around the optical axis. The microparticles' rotation can be achieved by rotating the cylindrical lens around the optical axis, as initially demonstrated in [10]. Dasgupta and collaborators could rotate biological entities freely suspended in a water-based medium, or even subcellular organelles within living cells, with a speed up to 9 rad/s without damaging the trapped object. More interestingly, the researchers were also able to rotate aggregates of healthy and unhealthy RBC at a speed of 3 rad/s.

Even though some examples of optical trapping with line tweezers have been produced, to the best of my knowledge, none of them analyses the optical trapping of an RBC with a line-tweezer theoretically. Moreover, a theoretical investigation can be used to shed light on the complete confinement of RBCs with a line-tweezers. For this reason, in the remainder of this chapter, I theoretically investigate the RBC optical trapping with a line-tweezer.

5.2. Model

In the current chapter, a three-dimensional cartesian co-ordinates system is considered, and a single Gaussian laser beam propagates towards $+\hat{z}$. The wavelength of the light beam is chosen to be 1.064 μm in agreement with the vast majority of experiments and with the light source present in our laboratory (Nd:YAG laser). To reproduce the line-tweezer, the Gaussian laser beam (100 μm beam waist) is decomposed into a bundle of light rays with appropriate intensity and direction. The light rays are then focalised along the x-axis, as shown in Figure 5.2-a and -b. The focal length of the cylindrical lens is 10 μm, while the power is always 5 mW for the reasons reported in the previous chapter.

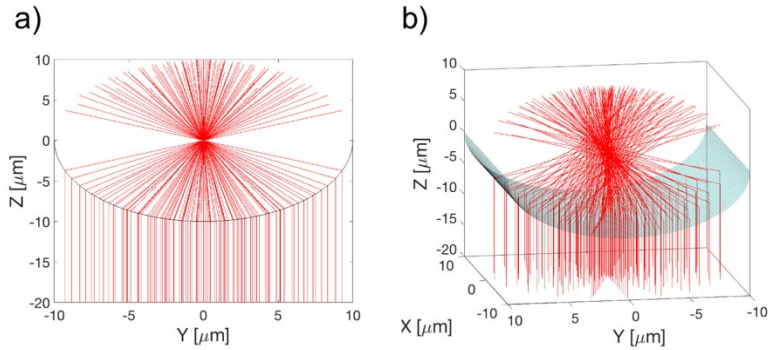

Figure 5.2. Decomposition of the Gaussian laser beam into a bundle of light rays focalised over the x-axis. a) lateral view and b) perspective view.

As in the previous chapters, the RBC is considered immersed in a water-based medium ($n_1 = 1.33$), and filled by a non-absorbing medium with isotropic physical properties (index of refraction n_2 = 1.38, and density ρ = 1.11 g/cm^3). Since the cell density is higher than the density of the surrounding fluid, a constant force ($\boldsymbol{F_b}$ = -0.1 pN) acting along the z-axis is always considered, as explained in chapter 3. The RBC is always considered a rigid body (i.e. not deforming in response to the optical pressure), and the cell-medium interface is modelled as a single net line. The RBC is always in its healthy biconcave disk conformation, and the parameters describing the RBC disk are those extensively described and used in chapter 3. In addition to the laboratory reference frame (Σ_l), I define a second cartesian frame of reference centred on the centre of mass of the RBC, particle

reference frame (Σ_p) according to what is reported in chapter 4.

For biological samples, the fraction of power that is reflected after a scattering event is very low (< 0.001),[12] and therefore to a good approximation I can consider only the first two scattering events.

In these conditions, the geometrical optics approximation is completely fulfilled, hence, the optical forces and torques can be calculated with GO following the scheme reported in chapter 3 and in [13].

5.3. Numerical computation

5.3.1. Infinite light-sheet width

In this section, I report the numerical analysis for a line-tweezer in which the beam is focalised over a line whose length (100 μm) is much bigger than the typical size of an RBC (7.82 μm). This is particularly important since a strong gradient in the light intensity is obtained only along the y- and z-direction, so the cell is completely free to move along the x-direction. In analogy with the static equilibrium searching analysis carried out in the previous chapters, I start the numerical investigation by displacing the RBC along each degree of freedom (translational and rotational) at a time while keeping the other fixed. Initially, the cell is maintained

in its 'folded' configuration (i.e. cell plane parallel to the xz-plane in the laboratory reference frame) and centred at the origin of the xy-plane while displaced along the z-direction with steps of 0.01 μm.

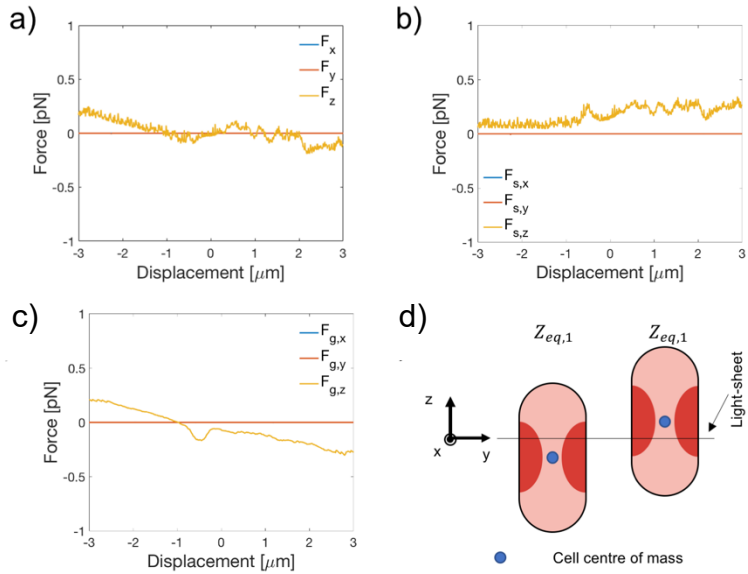

Figure 5.3. a) Force-displacements curve along the z-direction, and force's decomposition in scattering and gradient component (b) and (c) respectively. d) Schematic depiction of the possible equilibrium position of an RBC along the beam propagation direction.

Figure 5.3.-a shows the force-displacements curve for an RBC displaced along the z-direction as a function of the cell displacements in terms of the cartesian components. As expected, no optical forces are present along the x- and y-axis. On the contrary, a net (inhomogeneous) optical forces

component is visible along the z-direction. $F_z(z)$ initially decreases linearly vanishing with negative slopes at approximately -1 μm, suggesting a stable optical trapping. On the contrary, the RBC is repelled away from the origin, Figure 5.3.-a. Interestingly, a second stable trapping position seems to be present at approximately +1 μm. This can be understood by observing that a healthy RBC is a biconcave disk. In fact, the RBC can be trapped in two almost symmetrical equilibrium positions in respect to xy-plane where the deepest portion of the dimple is completely above or below this plane, Figure 5.3.-a and -d. As discussed in chapter 3, the presence of the central dimple plays a pivotal role in determining the rays' path and, ultimately, the optical forces. If the centre of the cell is close to the origin, a consistent portion of light rays undergoes to total internal reflection on the interior of the dimple, increasing $\boldsymbol{F_s}$, while $\boldsymbol{F_g}$ remains essentially unaltered, Figure 5.3.-b and c. The balance between $\boldsymbol{F_s}$, $\boldsymbol{F_g}$ and $\boldsymbol{F_b}$ dictates the two symmetrical equilibrium positions along the z-direction. However, the high irregularities of the force-displacements curve renders problematic the trap stiffness estimation with the methodology used in the previous chapter (linear fitting).

Successively, the cell is placed at z_{eq} = -1 μm and y = 0 μm, and the force-displacements curve is simulated for cell translation along the x-direction, Figure 5.4-a. As

expected, no forces arise along this direction since no strong light intensity gradient are present. However, for very big displacement, comparable to the size of the line along the x-direction, $F_x(x)$ would be visible. Therefore, for the present analysis I will set x_{eq} = 0 μm. Later in the text, I will discuss how confining the size of the 'light line' to approximately the cell diameter results in a clear confinement along the x-direction.

Having verified that no restoring forces act along the x-direction, the cell is placed at x_{eq} and z_{eq} = -1 μm, and the force-displacements curve is calculated for the y-direction. As expected, no optical forces act along the x-direction, and only small z-component of force are present for relatively large displacement along the y-direction. On the other hand, $F_y(y)$ vanishes with negative slope at y_{eq} = 0 μm, suggesting the presence of stable equilibrium position, Figure 5.4-b.

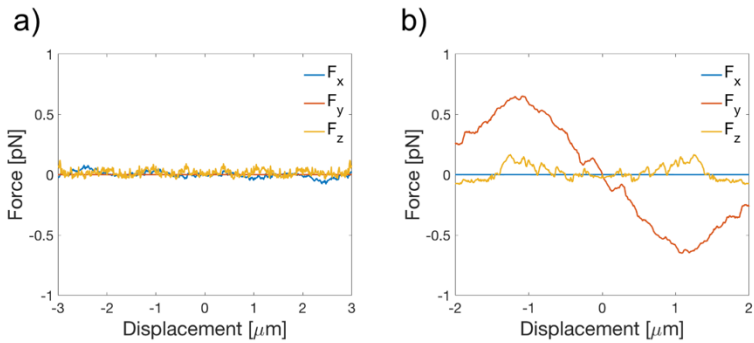

Figure 5.4. Force-displacements curve along the x- and y-direction, (a) and (b) respectively.

Once the equilibrium position is thoroughly analysed, I turn my attention to the rotational confinement. As introduced in chapter 3, non-spherical objects align with the optical axis when optically trapped because of the optical torques (τ). For a trapped object, these torques must be restoring to keep the cell in a defined orientation. In the present situation, the RBC's plane must be parallel to the optical axis, and the cell's plane must contain the light-sheet.

Initially, I analysed the torque-rotations curve for RBC rotation around the x-axis (α). The cell is placed at x_{eq}, y_{eq} and z_{eq} = -1 μm, and is rotated with angular steps of 1°. The optical torques acting on the cell are calculated after each angular displacement. Figure 5.5-a shows $\tau(\alpha)$, where α = 90° corresponds to a cell in its 'folded' configuration with its plane comprised in the xz-plane. Here it can be seen that a

$\tau_x(\alpha)$ vanishes with negative slope at α_{eq} = 90°, suggesting that a stable equilibrium configuration is present for an RBC in its 'folded' configuration. On the other hand, an unstable equilibrium is visible for a cell in its 'flat' configuration, that is, for a cell that has its plane parallel to xy-plane.

Not surprisingly, if the cell is rotated around an axis passing through the centre of mass and parallel to the y-axis no torque are present, Figure 5.5-b. This can be understood by the fact that the cell is rotating around its axis of symmetry.

Lastly, I analyse the torque-rotations curve for cell rotation around the z-axis (angle γ) while keeping the cell at equilibrium position (x_{eq}, y_{eq}, z_{eq} = -1 μm, and α_{eq} = 90°) configuration. Here 0° rotation corresponds to a configuration where the RBC has its plane parallel to the xz-plane. From Figure 5.5-c, it can be seen that $\tau_z(\gamma)$ vanishes with a negative slope for γ_{eq} = 0° suggesting an effective rotational confinement. This is particularly interesting if compared to the single-beam optical tweezers case, where the cell is completely free to 'flap' around the z-axis (see chapter 4).

Therefore, from this initial analysis for the simplest possible case (i.e. infinite light-sheet width), it is clear that the line-trap can easily confine the asymmetrical object in a specific equilibrium configuration.

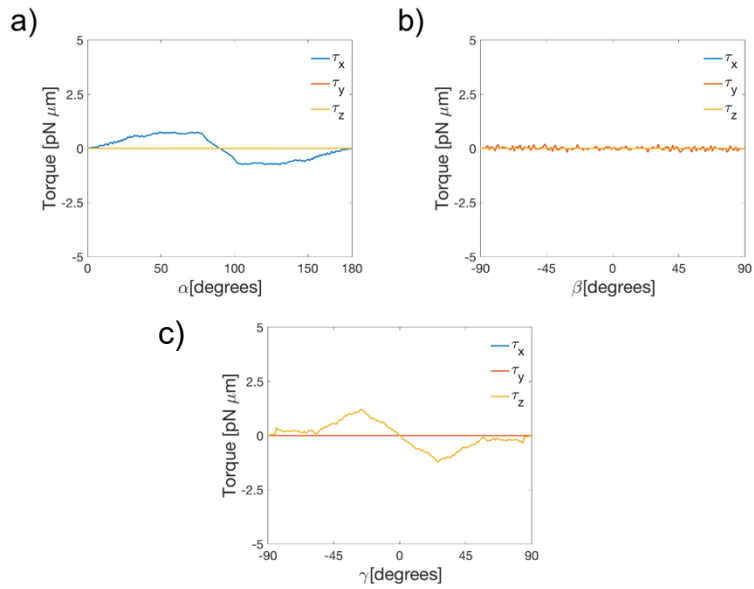

Figure 5.5. Torques-rotation curves for cell rotation around the $x-$, $y-$, z-direction, (a), (b), and (c), respectively.

5.3.2. Finite light-sheet width

Until now, I have always considered a simple case where the size of the light-sheet is much bigger than the cell diameter, and therefore the cell does not experience a strong light gradient along the x-direction. This reflects on an absence of a restoring force along the direction over which the beam is focused. However, decreasing the light-sheet extent along the x-direction would also create a strong light gradient in the direction along which the light is focused. One

may think to simply reduce the beam waist of the incoming beam to match the diameter of the cell or to block the light selectively with a circular aperture of the same size as the cell diameter (i.e. 7.82 µm). However, the high rays' convergence needed for a stable axial trapping is completely lost with these approaches. An alternatives solution to this issue is to modify the shape of the incoming beam by using a second cylindrical lens. Doing so, the beam is made elliptical at the second cylindrical lens and is then focalised by the objective lens as schematically depicted in Figure 5.6-a and b. At the objective lens, the focusing of an elliptical beam guarantees the high rays' convergence along one direction necessary for a stable axial trapping. Moreover, by tuning the distance between the two cylindrical lenses (telescope), the length of the light sheet can be controlled so that the RBC can be completely confined.

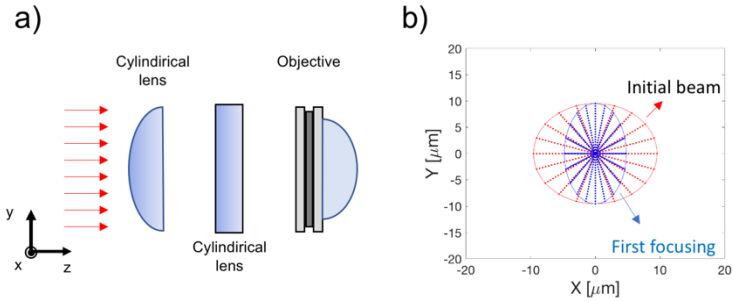

Figure 5.6. Schematic depiction of the optical set-up used in the numerical experiments. Two cylindrical lenses are used to shape the incoming beam

before the objective lens. b) Rays starting point (red) and elliptical beam (blue) focused by the objective lens.

To evaluate the effect of the light-sheet width along the x-direction, I choose four different sizes for the light-sheet. These correspond to a beam width that coincides to the thickest portion of the cell 5.52 μm, Figure 5.7-a, to an intermediate width between the thickest part of the cell and the cell diameter 6.67 μm, Figure 5.7-b, to a width equal to cell diameter 7.82 μm, Figure 5.7-c, and to a width slightly higher than the cell diameter 8.97 μm, Figure 5.7-d.

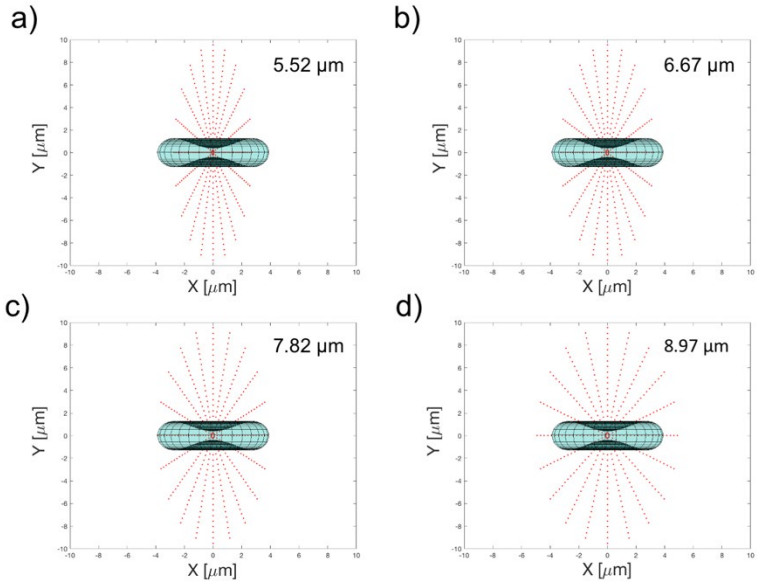

Figure 5.7. Projection of the starting point of the light rays for different beam sizes. a) The beam semi-axis is 5.52 μm, in (b) is 6.67 μm, in (c) 7.82 μm and in (d) is 8.97 μm.

In all the cases investigated, the high light convergence needed for a stable axial trapping is assured. This can be appreciated by observing the ray-tracing performed in the different condition, Figure 5.8-a-d.

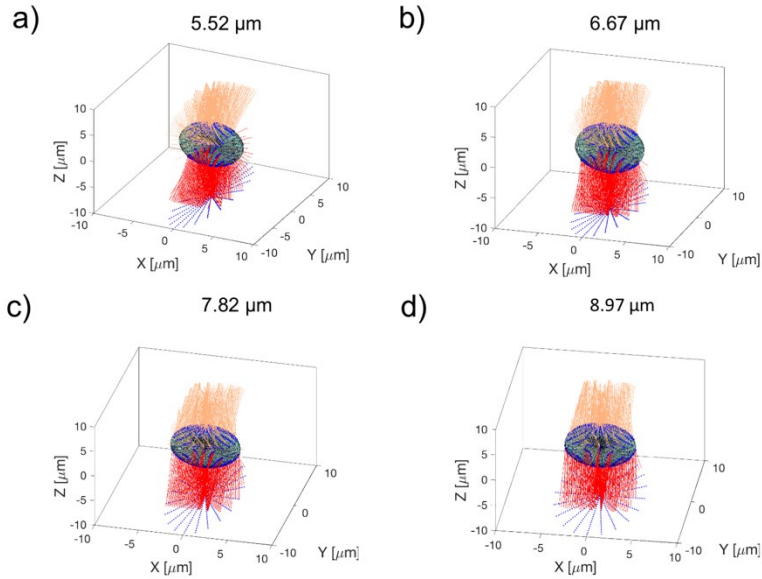

Figure 5.8. Ray traces for beams of different sizes. Only the light rays that interact with the cell are shown in (d).

Figure 5.9-a shows the force-displacements curves as a function of the cell displacements along the x-direction for different light-sheet widths while the cell is kept in its 'folded' configuration at y = z = 0 µm. Note that only the x-component of the force is shown. Here it can be seen that as the size of the light-sheet is decreased, the force traces

vanish with a negative slope at x_{eq} = 0 μm. Importantly, this suggests that a restoring force is also introduced along the x-direction, and therefore the cell can be completely confined via a light-sheet tweezers. To compare the trapping strength in the different conditions, I use the trap stiffness (k_x); see chapter 2 and 3 for a detailed description. For each force-displacement curve, k_x is extrapolated with a linear fit of the approximately linear region of the plot and is plotted as a function of the light-sheet width, Figure 5.9-b. As the light-sheet width increases, k_x increases accordingly, until it reaches a maximum value of approximately 0.12 pN·μm^{-1}·mW^{-1} when the light-sheet width matches the cell's diameter (7.82 μm) and then decreases if the light-sheet width is increased further. This behaviour can be explained considering that the cell is subjected to the highest light gradient when the beam size equals the RBC diameter.

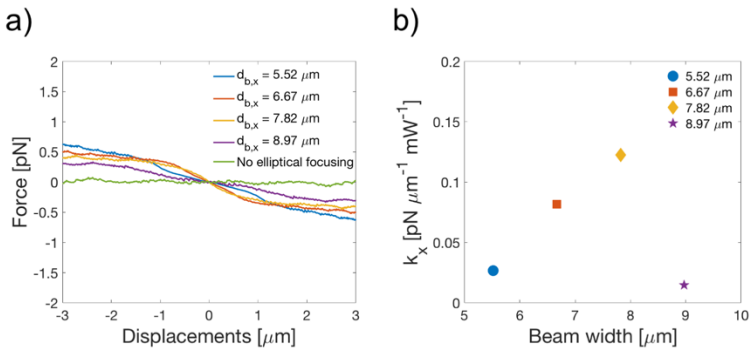

Figure 5.9. a) $F_x(x)$ for different light-sheet widths. b) k_x for different light-sheet widths. k_x is estimated fitting a line to the linear portion of the plot in (a).

Successively, I investigate the effect of varying the beam size for cell displacements along the y-direction. The cell is placed at x_{eq} = 0 μm and kept in its 'folded' configuration while displaced along the y-direction. In Figure 5.10-a are shown $F_y(y)$ as a function of the cell's displacements along the y-direction. In every case $F_y(y)$ vanish with negative slope at y_{eq} = 0 μm, suggesting the presence of a restoring force along this direction. However, compared to the x-direction, it is evident that the aspect ratio of the trapping beam has a minor effect on $F_y(y)$, and only for significant cell displacements (>0.5 μm) some differences appear. In fact, the large positive and negative peaks are much less pronounced when the beam is not elliptical because only a fraction of the total beam power hits the cell.

However, for small displacement (<0.1 μm), the disparities are much less pronounced, and there are no differences between the different conditions (insert Figure 5.10-a). As before, the trap stiffnesses (k_y) are used to discern between the different conditions, Figure 5.10-b. k_y reaches a maximum value of approximately 0.4 pN·μm^{-1}·mW^{-1} when the size of the incoming beam is intermediate between the diameter of the maximum thickness and the cell's outer diameter. However, the values of k_y are relatively constant compared to k_x.

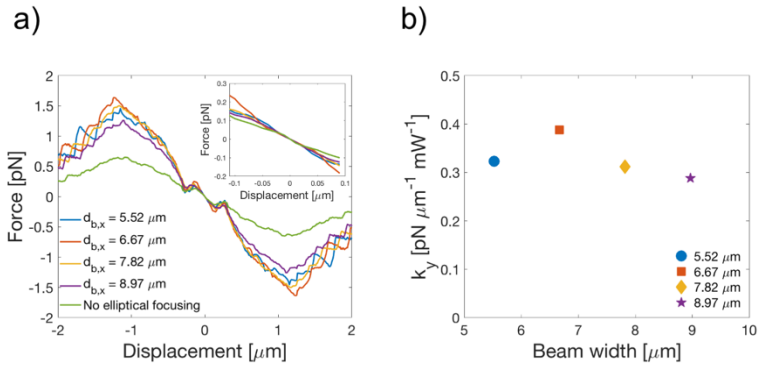

Figure 5.10. a) $F_y(y)$ for different light-sheet size. b) k_y for different light-sheet size. k_x is estimated fitting a line to the linear portion of the plot in (a).

Lastly, I simulate the force-displacements curve for displacements along the z-direction. The RBC is placed in the 'folded' configuration at x_{eq} and y_{eq} and the cell is translated along the z-direction, while the cell's plane is

constrained in the xz-plane. Figure 5.11 shows $F_z(z)$ as a function of the cell displacements from the origin for different light-sheet widths. Even if the general trend of the force traces agrees with the one obtained for an infinite line, it is visible that as the beam size increases, the negative z_{eq} seems to shift towards 0, passing from z_{eq} = -1.505 μm for a light-sheet width of 5.52 μm to z_{eq} = -0.943 μm for a light-sheet width of 8.97 μm.

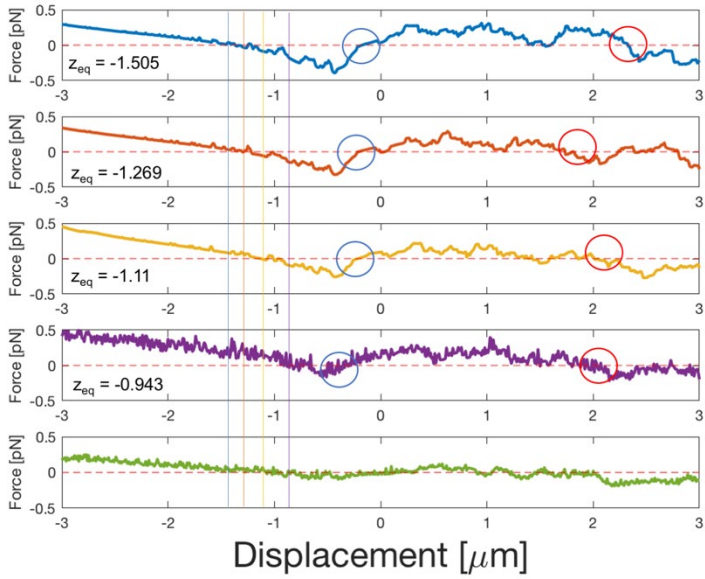

Figure 5.11. $F_z(z)$ for different light-sheet widths. The vertical line and the red circles represent the two points of equilibrium for the RBC. The blue circle show the point of unstable equilibrium close to the origin of the Cartesian co-ordinates system.

Moreover, even the inhomogeneities of the force traces seem to increase as the beam size increases. Two factors can be accounted for the different locations of -z_{eq} and for the irregularities in the force traces. On the one hand, as the light-sheet width increases, the fraction beam power that strikes the cell in a specific location change accordingly. This modifies how the total optical forces are subdivided between $\boldsymbol{F}_s$ and $\boldsymbol{F}_g$ (see chapter 3 for a detailed description), and therefore the location of the z_{eq} observed. On the other hand, the finite number of light rays could enhance this effect further because the light rays with the highest power are likely to strike the central dimple generating force spikes in $\boldsymbol{F}_s$, Figure 5.12-a and b.

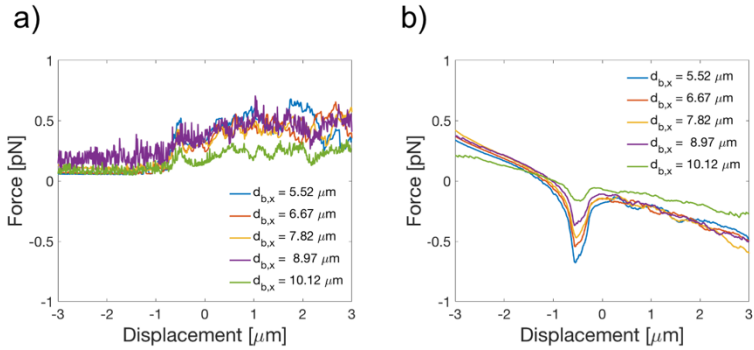

Figure 5.12. Scattering (a) and gradient (b) component of $F_z(z)$ for different light-sheet widths.

However, the positive z_{eq} seem to be less affected by the light-sheet width, red circle in Figure 5.11. The RBC is

always repelled away from the origin because of its biconcave disk conformation, blue circle in Figure 5.11. Even though the force traces clearly suggest the ability of the light-sheets to optically confine the RBC, the extrapolation of the trap stiffness is not possible via a linear fitting because of the high irregularities of the force-displacements curves.

Once the equilibrium position is fully characterised, I analyse the rotational equilibrium. Similarly to the infinite line case, I explore the cell rotation around the x-axis (angle of rotation α). The RBC is placed at the respective x_{eq}, y_{eq} and -z_{eq} in its 'folded' configuration with its plane parallel to the xz-plane. The cell is rotated with angular steps of 1°, and the optical torques acting on the RBC are calculated after each angular step.

In Figure 5.13-a are shown $\tau_x(\alpha)$ for different light-sheet widths. Here at 0° and 180°, the cell is in the 'flat' configuration, while at 90°, the cell is in the 'folded' configuration. All $\tau_x(\alpha)$ vanish with negative slope at α_{eq} = 90°, suggesting that the cell is rotationally confined in its 'folded' configuration. Moreover, it is also evident that $\tau_x(\alpha)$ show higher peaks when the beam is focused over a shorter line. This is expected since the light intensity is concentrated in a smaller region, but it preserves the size along the transverse direction. As done previously for the spatial confinement, I characterise the traps strength by means of

the spring constant (k_α), which slowly decreases from its highest values for the shorter light-sheet width, Figure 5.13-a.

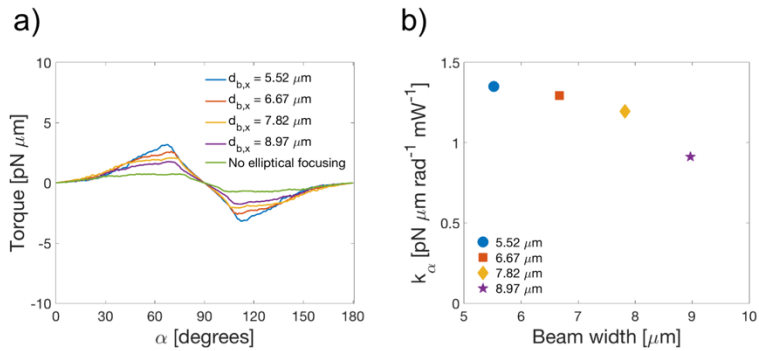

Figure 5.13. x component of the torque-rotations curve for cell rotation around the x-axis, and (b), k_α for different light-sheet widths.

Successively, I place the cell at the equilibrium positions (both positional and rotational), and I rotate the cell around the y-axis while calculating the optical torques. Not surprisingly, the cell does not experience any optical torque since it is rotating around its axis of symmetry.

Lastly, to verify the last degree of confinement, the cell is placed at the equilibrium positions and is rotated from the rotational equilibrium around the z-axis (angle of rotation γ). In Figure 5.14-a are shown $\tau_z(\gamma)$. Here it can be seen that all the $\tau_z(\gamma)$ vanish with negative slopes for γ_{eq} = 0°, that is, for a cell whose plane is parallel to the xz-plane and contains the optical axis, suggesting a rotational confinement even for

this kind of rotation. The $\tau_z(\gamma)$ peaks are of higher magnitude when the light-sheet width is comparable to the cell diameter (7.82 μm), and they decrease if the beam width is increased or decreased. This is completely expected. In fact, when the light rays (and thus the beam's power) are distributed over the entire cell surface, they can exert the highest τ since the total initial power is incident over the entire cell. On the contrary, if the line width is bigger than the size of the cell, some rays do not strike the cell and part of the initial beam's power is lost, and thus the torques are smaller. On the other hand, if the beam is smaller than the diameter of the cell, the rays impinge on the cell closer to the centre of mass and thus τ decreases even if the beam power is concentrated in a smaller region. For these reasons, the highest trap stiffnesses (k_γ) for this rotational motion are reached when the light-sheet has the same size of the cell diameter.

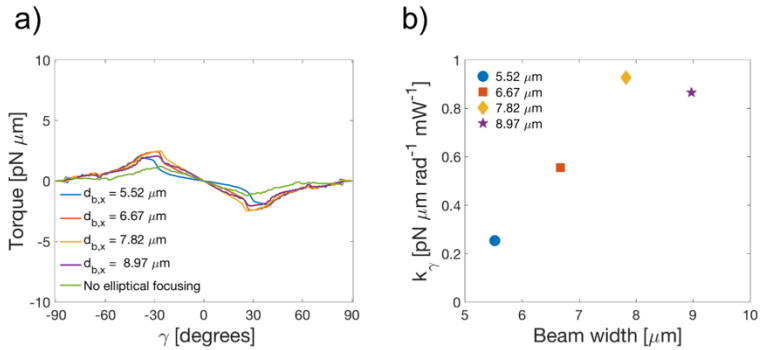

Figure 5.14. Z-component of torque-rotation curves for cell rotation around the z-axis (a), and the respective trap stiffness (k_γ) (b)

Comparing the results obtained for the light-sheet optical tweezers with those obtained for a single-beam optical tweezers, some differences arise. Compared to the single-beam case, a light-sheet optical tweezer can fully spatially confine the RBC only if the light-sheet width is controlled. Moreover, a light-sheet optical tweezer can rotationally confine the cell in the xz-plane, results that can only be obtained with a double-beam optical tweezers in the case of the widely used point trap.

The possibility to rotationally confine an RBC on a specific plane, thanks to its non-spherical shape, open up the prospect to obtain a controlled cell rotation by rotating the light-sheet as initially pointed out by Dasgupta *et al.*[10] In particular, a cell rotation can be obtained by the contemporary rotation of the two cylindrical lenses around the optical axis. If the two lenses are rotated simultaneously, the light-sheet rotates accordingly, and so the cell is confined in the plane containing the optical axis and the light-sheet 'line'. For this reason, as the last numerical experiment, I numerically analyse the possibility to rotate a single RBC suspended in a biological medium via a light-sheet optical tweezer.

In the following simulation, the width of the light-sheet is chosen to be 7.82 μm since it has been shown that maximise k_γ and therefore, the confinement in the trapping

plane should be the highest. The simulation of the dynamic of the trapped cell follows the numerical scheme introduced in chapter 4, while the parameters regarding the physical system are those reported previously. To simulate the rotation of the two cylindrical lenses, the light-sheet is rotated with a step gradient of 1° every 0.1 s around the optical axis, from 0° up to 90°. A step gradient is chosen to agree with possible future experiments. In fact, with this simple set-up, the cell rotation can be achieved via the synchronous rotation of the two cylindrical lenses by a stepper motor. Although the light-sheet could be rotated at different speeds, the RBC encounters the viscous drag of the fluids. Therefore, a higher rate of rotation would result in significant delays in the response of the cell.

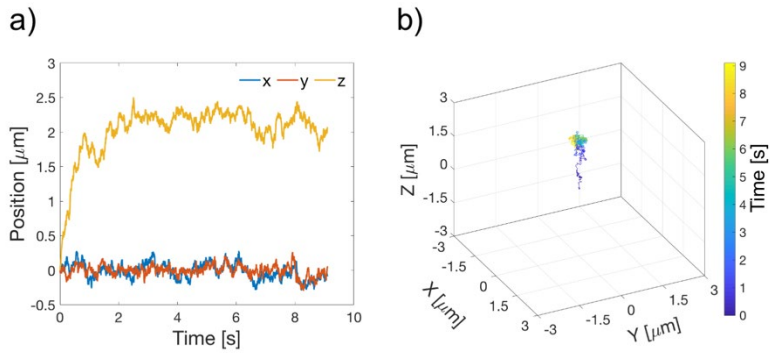

Figure 5.15. Position of the centre of mass of the cell as a function of the simulation time in terms of the Cartesian co-ordinates (a) and 3D trajectory (b).

The cell is initially placed at the centre of the co-ordinates system in its 'folded' configuration with the plane parallel to the xz-plane. At t = 0 s, the light beam is turned on and the position and orientation of the RBC is recorded via the cell's centre of mass co-ordinates and with the angle θ and ϕ defined in chapter 4.

Figure 5.15-a shows the position of the centre of mass of the cell as a function of the simulation time. Here it can be seen that the cell immediately migrates to $+z_{eq}$ = +2 μm where it stabilises, while the cell remains confined at the centre of the trap (i.e. the origin of the Cartesian co-ordinates system) in xy-plane. These findings agree well with the equilibrium position found with the static equilibrium searching analysed previously. Simultaneously to these translations, the cell, confined in its 'folded' configuration, also starts to rotate around the optical axis following the rotation of the light-sheet with an average angular velocity of approximately 0.2 rad/s for a beam power of 5 mW, Figure 5.16-a. Moreover, comparing the trajectories of the centre of mass of the cell with its orientation, it can be seen that the rotation of the light-sheet does not influence the position of the cell, and the cell is constantly trapped at the equilibrium position, Figure 5.15 and Figure 5.16.

Even if the angular velocity reported for this numerical experiment is ~10 times smaller than the values obtained

from Dasgupta and collaborators (1-10 rad/s),[10] the values are in good agreement. In fact, the authors used a beam power in the order of tens of mW while I am using just few mW. Since the torque is directly proportional to the beam's power, an increase in the beam's power would result in a higher torque able to counteract the viscous torque and thus in a relatively higher angular velocity. However, for a very elastic object like an RBC, a higher beam's power would induce a significant deformation of the trapped object, resulting in considerable errors in the calculation.

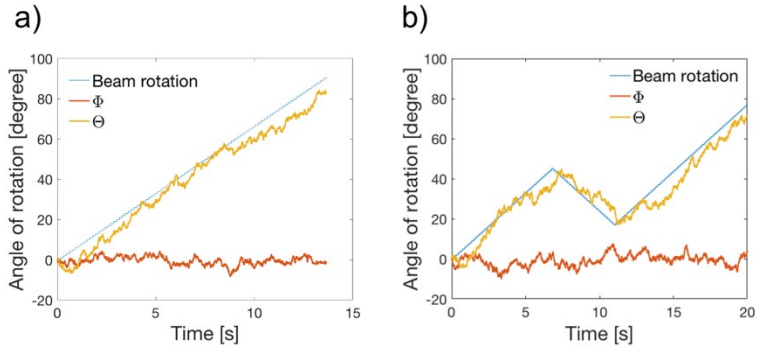

Figure 5.16. Orientation of the cell as a function of the simulation time (a). In (b) is shown as is possible to control the rotation of the cell inverting the direction of rotation of the light-sheet.

Lastly, I also evaluate the possibility of re-orientating the cell around the optical axis by simply inverting the direction of rotation of the light-sheet as shown in Figure 5.16-b. Here it can be seen that the cell can be deliberately

re-oriented around the optical axis by simply changing the direction of rotation of the light-sheet.

5.4. Conclusion

In this chapter, I reported a numerical investigation of the optical trapping of healthy RBC with a light-sheet optical tweezer. Initially, I demonstrated the possibility to optically confine an RBC with a light-sheet of infinite width within a specific plane defined by the optical axis and the direction over which the beam is focused. Successively, I showed the ability of a light-sheet optical tweezer to entirely confine the healthy RBC, both spatially and rotationally. Interestingly, a complete confinement can be obtained if the light-sheet width is controlled, and the highest trapping strength was obtained for a light-sheet width comparable to the cell diameter. Since a light-sheet tweezer can confine the RBC in a specific plane, the rotation of the light-sheet can be used to direct the re-orientation of the cell via the simple light-sheet rotation.

In conclusion, the presented analysis is in good agreement with experiments and paves the way for possible future experiments in which the re-orientation of a single RBC cell must be controlled and kept constant, as for example, within a fluid flow.

5.5. Bibliography

[1] A. Ashkin, *Phys. Rev. Lett.* **1970**, *24*, 156.

[2] A. Ashkin, J. M. Dziedzic, *Science (80-.).* **1987**, *235*, 1517.

[3] A. Ashkin, J. M. Dziedzic, T. Yamane, *Nature* **1987**, *330*, 769.

[4] A. Ashkin, J. M. Dziedzic, J. E. Bjorkholm, S. Chu, *Opt. Angular Momentum* **1986**, *11*, 288.

[5] S. Sato, M. Ishigure, H. Inaba, *Electron. Lett.* **1991**, *27*, 1831.

[6] L. P. Faucheux, G. Stolovitzky, A. Libchaber, *Phys. Rev. E - Stat. Nonlinear, Soft Matter Phys.* **1995**, *51*.

[7] W. B. Rogers, J. C. Crocker, *Rev. Sci. Instrum.* **2014**, *85*.

[8] Y. Roichman, D. G. Grier, *Opt. Lett.* **2006**, *31*, 1675.

[9] A. H. VOIE, D. H. BURNS, F. A. SPELMAN, *J. Microsc.* **1993**, *170*, 229.

[10] R. Dasgupta, S. K. Mohanty, P. K. Gupta, *Biotechnol. Lett.* **2003**, *25*, 1625.

[11] P. P. Mondal, A. Singh, P. Joshi, J. Basumatary, N. Baro, *bioRxivxiv* **2021**, 1.

[12] J. Guck, R. Ananthakrishnan, H. Mahmood, T. J. Moon, C. C. Cunningham, J. Käs, *Biophys. J.* **2001**, *81*, 767.

[13] P. H. Jones, O. M. Maragò, G. Volpe, In *Optical Tweezers Principles and applications*; Cambridge University Press: Cambridge, 2015; pp. 19–41.

6. MACHINE LEARNING FOR THE SIMULATION OF OPTICALLY TRAPPED ERYTHROCYTES.

Geometrical optics (GO) calculations for particle with complex shape are intrinsically slow. This can be a major drawback when one intends to simulate the Brownian dynamics of an optically trapped particle. Indeed, Brownian dynamics simulations often requires a recursive calculation of optical forces and torques to simulate the time evolution of the particle trajectories. Thus, simulating for long time, or for multiple repetitions becomes rapidly computationally prohibitive. In this chapter, I describe a study done in collaboration with Nano-Soft Lab at CNR in Messina, Italy. We employ an artificial neural network (NN) to predict the optical forces and torques acting on a healthy red blood cell faster and with higher accuracy compared to GO. The NN prediction are then used within the numerical scheme introduced in chapter 4 in simulating the Brownian dynamics of a red blood cell trapped in double-beam optical tweezers, observing a decrease in computation time of two order of magnitude.

Here, I performed the geometrical optics calculation and the simulation of the dynamic of the trapped cell while

David Bronte Ciriza, PhD student from Nano-soft lab, set up and trained the neural network.

6.1. Introduction

Soon after their introduction in the late 1980s,[1] optical tweezers (OT) were immediately applied to trap and manipulate viruses, bacteria, eukaryotic living cells, and cells' organelles.[2,3] The nature of biological samples make them particularly susceptible to photodamage, and infrared light with a wavelength in the second biological window (i.e. around 1064 nm), demonstrated significant reduction in photodamage when dealing with biological samples, and therefore is generally preferred for biological experiments.[4]

In the last couple of decades, OT has been widely applied in red blood cell research to investigate biochemical and biophysical properties of both healthy and unhealthy erythrocytes.[5] Healthy red blood cells (RBC) have a biconcave disk conformation with a diameter of 7-8 μm, a thickness of 0.5-1.5 μm in the middle and 2-3 μm in the periphery.[6] In studying these systems, numerical simulations are frequently used to plan and interpret experiments. According to the size parameter ($\xi = (2\pi a n_m / \lambda_0) \approx 80$), the geometrical optics approximation (GO) is usually the preferred method for modelling the beam-cell interaction (as we have seen in previous chapters).[7–9]

However, even though GO simplifies the theoretical treatment considerably compared to a full wave optical approach,[10] it still requires to ray trace every single light ray with a high computational cost. In relatively simple applications, these computations can be parallelised, or an interpolation-based approach can decrease the overall simulation time. Nevertheless, simulating the Brownian dynamics requires a sequential forces and torques calculation, and often for complex particles' shapes, these computations are prohibitive.[11]

Machine learning (ML) is emerging across research fields for its ability to make predictions for given inputs very efficiently without being explicitly programmed to do so. ML is based on algorithms that learn autonomously through a set of training data and build a model through experience.[12] A specific approach of ML is based on artificial neural networks (NN). A NN is a network or a circuit of artificial neurons or nodes that mimics the biological counterpart. Artificial NNs are structured in an input layer, a hidden layer, and an output layer. The connections between neurons are modelled as weights between nodes. A positive weight reflects an excitatory connection, while negative values mean inhibitory connections. By means of training data, the neurons learn (establishing specific connections) to map specific inputs to

specific outputs, similarly to the learning process of the human brain.[13]

Recently, ML has been applied to OT research. For example, Wang *et al*. used ML to classify RBC of different species via the Raman fingerprint of haemoglobin.[14] Researchers also applied NN to predict optical forces acting on spherical particles with greater accuracy than the phenomenological approach in significantly less time than exact methods.[15] Here, we use GO to calculate the optical forces and torques generated by a single-beam optical tweezer on a healthy RBC. The data points are then used to train a NN, which is then employed in simulating the Brownian dynamics of an optically trapped RBC in a double-beam optical tweezer.

6.2. Model and GO calculations

The GO calculation used as training data are generated considering a single-beam optical tweezer. The calculations are carried out with the methodology introduced in chapter 3, except that the number of total optical rays is decreased to $4 \cdot 10^2$ (20·20 light rays). The DBOT used for comparison to the NN prediction is simulated according to what is reported in chapter 3. The RBC position and orientation are defined as the co-ordinates of the centre of

mass of the cell ($x,\ y,\ z$), and the azimuthal (θ) and polar (ϕ) angles in respect to the fixed reference frame.

The Brownian dynamics simulations of the trapped RBC are carried out accordingly to the numerical scheme introduced in chapter 4, and the solution properties are T = 293 K and η = 0.001 Pa·s. If the NN is used to predict the optical forces and torques, the outputs of the NN are substituted to the GO calculation in eq. 4.9.

6.3. Neural network structure and training

Deep Neural Networks are one of the most basic deep learning structures. Recently, Convolutional Neural Networks (CNN) are becoming a basic tool for image analysis or Graph Neural Networks are pushing the boundaries of knowledge regarding the structure of proteins or molecules. However, our problem is simpler than that. For a given point in the space of parameters, we want to know the forces and the torques associated to it. This constitutes a basic regression problem, where deep neural networks still provide the best compromise between efficiency and simplicity.

Here, the neural network (NN) architecture is composed of one input layer with 6 neurons ($x, y, z, \cos(\theta), \sin(\theta), \varphi$), one output layer with 6 neurons ($F_x, F_y, F_z, T_x, T_y, T_z$), and 7 hidden layers in between with 256 neurons each, Figure 6.1.

The total number of parameters of the model is around $4 \cdot 10^5$. We have data for the optical forces and torques at $4 \cdot 10^6$ different points in the 5D space of parameters $(x, y, z, \theta, \varphi)$. 90% of these data points are used as training data set while the remaining 10% is kept as testing data set to evaluate the accuracy of the NN.

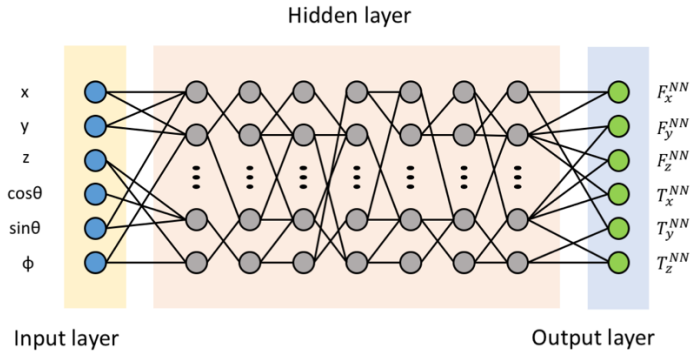

Figure 6.1. Schematic depiction of the artificial neural network used in this study.

The training data are generated via GO calculation made in OTGO as explained in chapter 3.[16] The cell is placed in uniformly distributed positions comprised in a cube of side 8 μm centred at the origin of the Cartesian coordinates system (i.e. $-4\ \mu\text{m} \leq x \leq 4\ \mu\text{m}$, $-4\ \mu\text{m} \leq y \leq 4\ \mu\text{m}$ and $-4\ \mu\text{m} \leq z \leq 4\ \mu\text{m}$). Simultaneously, to account for the possible different orientation of the RBC within the trap, the cell is uniformly and randomly oriented in an interval for $-\pi \leq$

$\theta \leq \pi$ and $0 \leq \phi \leq \pi/2$. The training data are generated for the simplest case of a single-beam optical tweezer.

The NN is trained in Python using Keras (version 2.2.4-tf).[17] The training of the NN is divided into 5 different steps. The data pre-processing and the model definition, which are done only once, the loading of the data, the training step, and performance evaluation, that are carried out iteratively. The training data, generated as previously described, contains data in different units and scales. While the position scale is in the order of ~10^{-6} m, the forces are on the range of ~10^{-12} N, and the torques around ~10^{-18} N·m. To achieve an efficient training of the NN, we need to apply a pre-processing step where the variables must be rescaled around unity and the "θ" angle, that ranges from -π and π, is expressed in terms of sines and cosines to avoid inconsistencies around 2π. Shuffling the data and dividing them into a validating and training set are the final step of the pre-processing. In our situation, the training data set contains $5.4 \cdot 10^6$ points while $6 \cdot 10^5$ points are reserved for the testing data set. In this work, we employ fully connected NNs where each neuron is activated by a sigmoidal function. Defining the model implies choosing the number of layers and the number of neurons per layer. We found that the architecture previously described consisting of 7 hidden layers provides the best results (in terms of accuracy, training time, and

speed). A more careful selection of these parameters might help to improve the performance. In an optimisation stage, we train different networks slightly changing the model parameters (different layers, different number of neurons…) and we keep the one that provides the best results (trial error). It is important to keep in mind that while one could think that a more complex structure would provide better results, this is not our case. Geometrical optics calculations introduced artifacts that we want to avoid learning. If our structure is perfect and the training is perfect, we would learn the artifacts too!

The iterative part of the training starts by loading a subset of the training data and applying the training step where the NN weights are optimised to minimise the loss function. We used the mean squared error as the loss function and the Keras implementation of the Adam optimiser.[17] Once the weights of the NN have been updated, the training data is erased from the RAM memory, and a new subset of the training data is loaded before repeating the same process. The strategy of dividing the training set into smaller subsets (instead of loading all at once) allows to use big training sets independently of the RAM memory. Once the training dataset is fully explored through all the subsets, the error between the NN calculation and the validating dataset (defined as the mean square difference) is

computed. The iterative step is repeated until this error stops decreasing. The training of the NN is done in a GPU type NVIDIA GeForce RTX 2060 with 16 GB of memory. The processor of the computer is an Intel Core i7-10700, and it has 16 GB of RAM.

6.4. Results

To evaluate the effectiveness of our approach, we initiate by testing the ability of the NN to predict the forces and torques acting on an RBC in a single-beam optical tweezer (SBOT). We commence by predicting the forces and torques at $1 \cdot 10^5$ unseen random positions and orientations. We then compare the NN prediction with GO calculation carried out at the same location and orientation ($1.6 \cdot 10^3$ rays, 40x40 light rays). The 2D density plots shown in Figure 6.2-a and -b gives us a picture of the goodness of the NN in predicting the optical forces (regression coefficient 0.998, R^2=0.996) and torques (regression coefficient 0.999, R^2=0.996), respectively. Indeed, the NN is trained with a data set produced with GO calculation made with a total of $4 \cdot 10^2$ rays, and thus less accurate in respect to the test data, and this makes us speculate that the NN can predict the forces and torques with higher accuracy in respect to the training data. We further compare the NN predictions with the GO calculation to test our hypothesis. Figure 6.2-c shows the

normalised root mean squared error (NRMSE) between the NN prediction and the GO calculation made with up to a total of $4.9 \cdot 10^3$ light rays. Here it is visible that the NRMSE between F_{tot}^{NN}-F_{tot}^{GO}, and τ_{tot}^{NN}-τ_{tot}^{GO}, decrease as the number of light rays increases. Moreover, when compared through the Euclidean similarity, the forces and torques calculated with $4.9 \cdot 10^3$ optical rays result more similar to the NN output than to the forces obtained with a total of $4 \cdot 10^2$ light rays. Thus, it is safe to say that the NN can increase the accuracy of the force/torque prediction compared to the GO calculation.

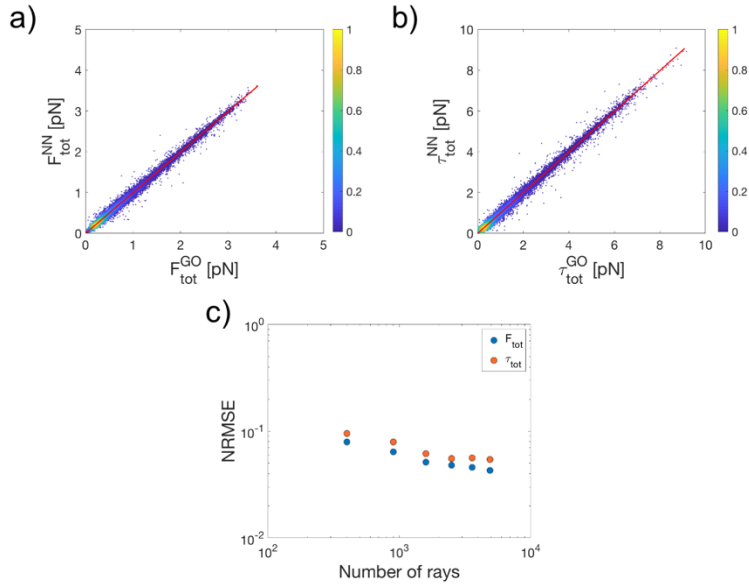

Figure 6.2. (a) Density plots comparing the magnitude of the total force predicted with NN (F_{tot}^{NN}) with those calculated with the GO method (F_{tot}^{GO}). (b) Density plot comparing the magnitude of the total torques predicted with the NN (τ_{tot}^{NN}) with the torque obtained with the GO method (τ_{tot}^{NN}). In red

are shown the regression lines. (c) Log-Log plot of the normalised mean squared error between F_{tot}^{NN}-F_{tot}^{GO}, and τ_{tot}^{NN}-τ_{tot}^{GO} as a function of the number of rays used in the GO calculation.

Since the NN is trained for a SBOT, one may think it can predict the optical forces and torques only for a SBOT. However, the NN can be used multiple times to simulate multi-beam optical tweezers. In fact, the NN can predict the forces generated by a single beam on different cell's locations, and then the total force acting on the centre of mass of the cell is calculated as the vector sum of each contribution. For a DBOT, since the two beams are focalised along the x-direction 5.06 μm apart, the input for the x-direction must be changed accordingly, while the other degrees of freedom are unchanged (i.e. $x_1 = x_{C.M.} + 2.53\ \mu\text{m}$, $x_2 = x_{C.M.} - 2.53\ \mu\text{m}$, $y_1 = y_2 = y_{C.M.}$ and $z_1 = z_2 = z_{C.M.}$, $\theta_1 = \theta_2 = \theta$, $\phi = \phi_2 = \phi$).

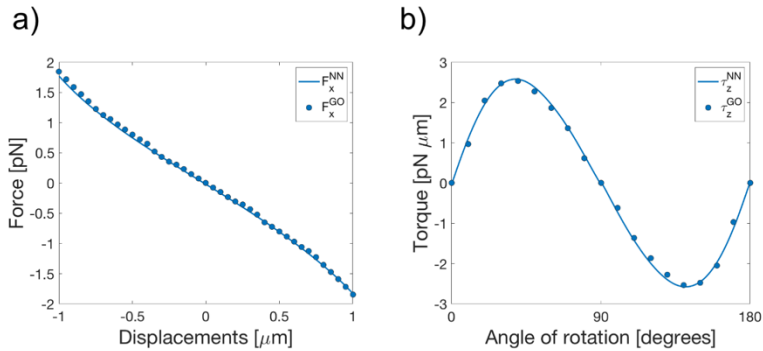

Figure 6.3. Comparison between GO calculation and NN prediction for the force-displacements curve for a DBOT along the x-direction (a) and torque-rotation curve for rotation around the x-axis (b).

Figure 6.3-a shows $F_x(x)$ simulated via GO and predicted with the NN for a cell in its 'folded' configuration (i.e. cell plane parallel to the optical axis) for a DBOT. Similarly, we also compare the ability of the NN to predict optical torques in the case of a DBOT, and as a representative example, we show $\tau_x(\alpha)$ (i.e. rotation around x-axis). In both cases, the predictions (solid line) agree well with the GO method (dots), demonstrating the possibility to use the NN for multi-beam optical traps. Therefore, we can securely conclude that a similar approach could be extended to predict forces and torques generated by a triple- and fourth-beam OT, situations in which the GO calculation are considerably slower given the very high number of light rays.

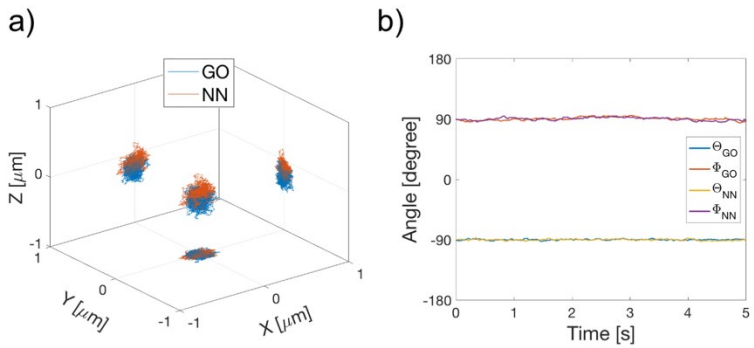

Figure 6.4. Brownian dynamics of an RBC in a force field: 3D-trajectories of the cell's centre of mass (a) and cell orientation (b). In every plot, the results obtained with the GO calculation are directly compared with those obtained with the predictions of the NN.

Successively, we investigate the cell's dynamics within a DBOT using both the NN and the GO. Figure 6.4-a shows the 3D trajectories of the centre of mass of the cell for a total simulation time of 5 s, while in Figure 6.4-b are shown the azimuthal (θ) and polar orientation (ϕ) of the cell as a function of the simulation time. By extracting the average values for each degree of freedom, it is possible to compare the final equilibrium configuration not only between the NN and GO but also with the static equilibrium searching (SES) of chapter 3. Indeed, the average values obtained with the predictions of the NN and GO methods agree well and are also in good agreement with the values obtained with SES, Table 6.1. Moreover, the most significant advantage of using the NN is a consistent decrement in the simulation time. Here

the time needed to simulate $5 \cdot 10^3$ time steps with a NN is approximately $8 \cdot 10^1$ s while the GO method requires approximately $8.5 \cdot 10^3$ s (*i.e.* a 100 times decrease). Since the NN shows a higher computational efficiency, hereafter, we make use of the NN prediction to simulate the Brownian dynamics for $2 \cdot 10^4$ steps with time increment Δt = 0.001 s.

	SES	**GO**	**NN**
$x_{2,eq}$ (μm)	0	0.013 ± 0.051	0.005 ± 0.051
$y_{2,eq}$ (μm)	0	0.004 ± 0.053	-0.001 ± 0.042
$z_{2,eq}$ (μm)	-0.232	-0.204 ± 0.083	-0.181 ± 0.082
$\phi_{2,eq}$ (°)	90	90 ± 0.022	90 ± 0.039
$\theta_{2,eq}$ (°)	-90	-90 ± 0.029	-90 ± 0.018

Table 6-1. Equilibrium position and orientation for an RBC in a double-beam optical tweezer as found with static equilibrium searching (SES), with geometrical optics (GO) and with neural networks (NN). For GO and NN are reported the average ± the standard deviation.

In chapter 2, I introduced a methodology to extract the trap stiffnesses by analysing the particle trajectories for a spherical particle. Here, we adopt a similar method that considers also the particle orientations. The diffusion tensor ($\boldsymbol{D}$) for a healthy RBC reads:

$$\boldsymbol{D}_{tt} = \begin{bmatrix} 7.427 \times 10^{-14} & -4.383 \times 10^{-20} & 6.234 \times 10^{-21} \\ 5.933 \times .10^{-21} & 7.427 \times 10^{-14} & 5.991 \times 10^{-21} \\ -8.744 \times 10^{-20} & -5.425 \times 10^{-19} & 6.283 \times 10^{-14} \end{bmatrix} 4.4$$

$\boldsymbol{D}_{rt}$=

$$\boldsymbol{D}_{tr}{}^{T} = \begin{bmatrix} -6.178 \times 10^{-15} & -2.520 \times 10^{-15} & -1.748 \times 10^{-15} \\ -2.520 \times 10^{-15} & 8.853 \times 10^{-16} & -2.724 \times 10^{-15} \\ -1.748 \times 10^{-15} & -2.724 \times 10^{-15} & -2.199 \times 10^{-16} \end{bmatrix} 4.5$$

$$\boldsymbol{D}_{rr} = \begin{bmatrix} 4.041 \times 10^{-3} & 3.627 \times 10^{-11} & 1.056 \times 10^{-10} \\ 1.043 \times 10^{-9} & 4.041 \times 10^{-3} & -7.846 \times 10^{-10} \\ 1.018 \times 10^{-10} & 3.169 \times 10^{-10} & 3.362 \times 10^{-3} \end{bmatrix} 4.6$$

$\boldsymbol{D}$ does not show any strong translation-rotation coupling; therefore, we do not expect to find any strong correlation in the cell's motion intrinsically due to the RBC's hydrodynamics. Within this framework, we initially assume the stiffness matrix to be diagonal, and we analyse the Brownian dynamics via a set of uncoupled Langevin's equations:[18]

$$\frac{dX_i(t)}{dt} = -\omega_i X_i(t) + \xi_i(t); i = x, y, z \qquad 6.1$$

$$\frac{d\phi(t)}{dt} = -\Omega_\phi \phi(t) + \xi_\phi(t) \qquad 6.2$$

$$\frac{d\theta(t)}{dt} = -\Omega_\theta \theta(t) + \xi_\theta(t) \qquad 6.3$$

where X_i, ϕ and θ are the stochastic variables associated with the position and angular coordinates, $\xi_i(t)$ are the random noise sources with zero mean and variance $\langle \xi_i(t)\xi_i(t+\tau)\rangle = 2D\delta(\tau)$, while $\omega_i = D_i k_i / k_b T$, $\Omega_\phi = D_\phi k_\phi / k_b T$, and $\Omega_\theta = D_\theta k_\theta / k_b T$ are the relaxation frequencies related to the forces and torque constants, and D_i are the diffusion tensor components.

We now evaluate the auto-correlation function (ACF) of the particle centre of mass trajectories and angular fluctuation. ACF for a non-spherical particle gives insight on the force and torque constants.[18,19] $C_{xx}(\tau)$ and $C_{zz}(\tau)$ decay as a single exponential with characteristic decay frequencies $\omega_x = 28\ s^{-1}$ and $\omega_z = 6.4\ s^{-1}$, Figure 6.5-a and -c, respectively. Somewhat unexpectedly, $C_{yy}(\tau)$ is well fitted with a double exponential with characteristic frequencies $\omega_{y,1} = 42\ s^{-1}$ and $\omega_{y,2} = 2.7\ s^{-1}$, Figure 6.5-b. For the latter, the fast decay rate is associated with the translation, while the slower decay can be related to rotation around the x-axis (ϕ in this context) induced by a motion along the y-direction, Figure 6.6-c. This would suggest that the coupling is probably due to a cross term in the stiffness matrix, and thus to the optical trap itself, and not to the cell's hydrodynamics.

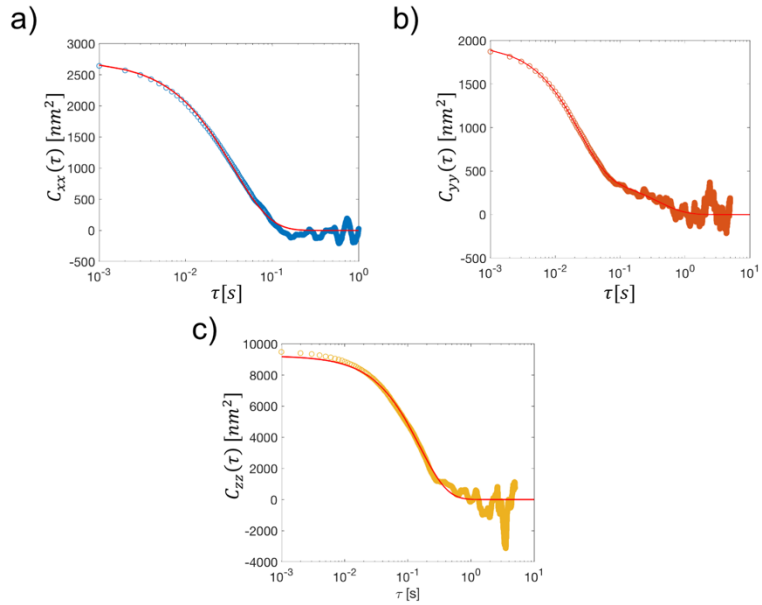

Figure 6.5. Translational autocorrelation function for the x-direction (a), y-direction (b), and z-direction (c).

Averaging over multiple repetitions, it is possible to obtain the average values and the standard deviation for the force constants ($k_{2,x} = \omega_x k_b T/D_{xx} = 0.166 \pm 0.024$ pN·μm^{-1}·mW^{-1}, $k_{2,y} = \omega_{y,1} k_b T/D_{zz} = 0.218 \pm 0.025$ pN·μm^{-1}·mW^{-1}, $k_{2,z} = \omega_z k_b T/D_{yy} = 0.005 \pm 0.001$pN·μm^{-1}·mW^{-1}), which values are in excellent agreement with those obtained with SES (see chapter 3), Table 6.2. Similarly to the translational motion, we calculate $C_{\phi\phi}(\tau)$ and $C_{\theta\theta}(\tau)$, Figure 6.6-a and -b. $C_{\phi\phi}(\tau)$ and $C_{\theta\theta}(\tau)$ decay as a single exponential and the respective trap constant are: $k_\phi = \omega_\phi k_b T/D_{\alpha\alpha} = 0.352 \pm$

0.096 pN·μm·rad^{-1}·mW^{-1} and $k_\theta = \omega_\theta k_b T / D_{\beta\beta} = 1.587 \pm 0.382$ pN·μm·rad^{-1}·mW^{-1} which agrees well with the values obtained in chapter 3, Table 6.2.

	SES	**NN**
$k_{x,2}$ (pN·μm^{-1}·mW^{-1})	0.153	0.166 ± 0.024
$k_{y,2}$ (pN·μm^{-1}·mW^{-1})	0.240	0.218 ± 0.025
$k_{z,2}$ (pN·μm^{-1}·mW^{-1})	0.005	0.005 ± 0.001
$k_{\phi,2}$ (pN·μm·rad^{-1}·mW^{-1})	0.370	0.352 ± 0.096
$k_{\theta,2}$ (pN·μm·rad^{-1}·mW^{-1})	1.730	1.587 ± 0.382

Table 6-2. Values of the trap stiffnesses obtained with static equilibrium searching (SES), and via the Brownian dynamics simulation made (NN). $k_{\phi,2}$ and $k_{\theta,2}$ corresponds to $k_{\alpha,2}$ and $k_{\gamma,2}$ of chapter 3.

Figure 6.6-c shows the correlation between the rotation around the x-axis (ϕ) and the motion along the y-direction. Here it can be seen a moderate negative correlation (Pearson's correlation coefficient -0.4085) which suggests that the RBC rotates as it moves away from $y_{eq,2}$, and undergoes to an "oscillating" motion about the equilibrium configuration where it is stably confined. As previously pointed out, this negative correlation is due to the presence of cross-term in the stiffness matrix. Figure 6.6-c shows the torque along the x-direction as a function of the of the displacement along the y-direction. Here it can be seen

an instable equilibrium position that induces the "oscillating" motion of the cell.

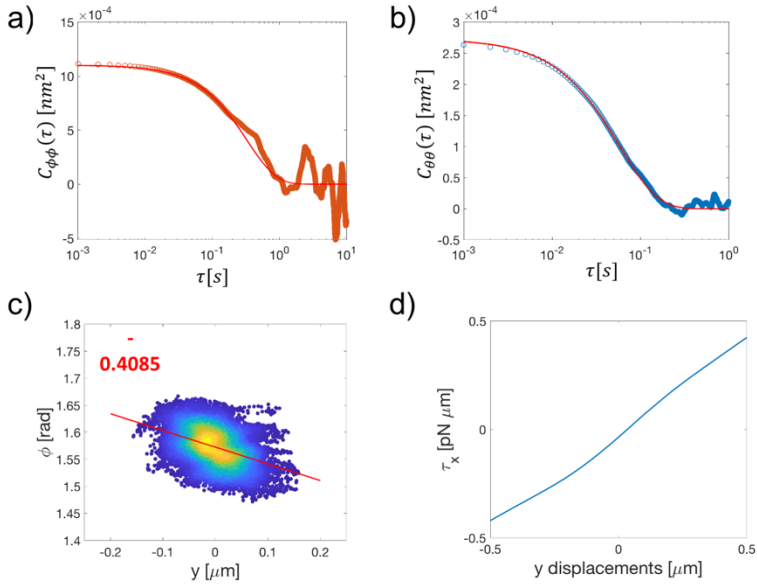

Figure 6.6. a) $C_{\phi\phi}(\tau)$, $C_{\theta\theta}(\tau)$ (b), and y-ϕ density plot (c), while in (d) is shown $\tau_x(y)$. The Pearson's correlation coefficient is reported in red in (c).

6.5. Chapter summary

In this chapter, it has been introduced a preliminary study carried out in collaboration with Nano-Soft Lab at CNR in Messina, Italy. In this work, we trained and used an artificial neural network (NN) to predict the optical forces and torques generated by a single-beam optical tweezer on a healthy red blood cell (RBC). The neural network demonstrates to predict the optical forces and torques with higher accuracy than geometrical optics calculation in significantly shorter computation time. Moreover, the as trained NN can be applied to a more complex case where multiple-beams are responsible for the trapping of the RBC. Thanks to the higher computational efficiency, the NN is used to simulate the Brownian dynamic of a trapped RBC in a double-beam optical tweezer for a significant longer simulation time. Lastly, the results of the simulation are used to extract the trap constants that characterise the optical trap via the auto-correlation method with a good agreement with the static method introduced in chapter 3.

ML can be easily extended to predict forces and torques acting on pathological RBC conformation where the GO are intrinsically slower. In the next, and final chapter, I will introduce a methodology to calculate optical forces and torques on a pathological RBC morphology (e.g. sickle cell)

where an analytical definition of the cell surface is not available.

6.6. Bibliography

[1] A. Ashkin, J. M. Dziedzic, J. E. Bjorkholm, S. Chu, *Opt. Angular Momentum* **1986**, *11*, 288.

[2] A. Ashkin, J. M. Dziedzic, *Science (80-.).* **1987**, *235*, 1517.

[3] A. Ashkin, J. M. Dziedzic, T. Yamane, *Nature* **1987**, *330*, 769.

[4] A. Blázquez-Castro, *Micromachines* **2019**, *10*, 1.

[5] T. Avsievich, R. Zhu, A. Popov, A. Bykov, I. Meglinski, *Rev. Phys.* **2020**, *5*.

[6] E. Evans, Y. C. Fung, *Microvasc. Res.* **1972**, *4*, 335.

[7] S. C. Grover, R. C. Gauthier, A. G. Skirtach, *Opt. Express* **2000**, *7*, 533.

[8] G. B. Liao, Y. Q. Chen, P. B. Bareil, Y. Sheng, A. Chiou, M. S. Chang, *J. Biophotonics* **2014**, *7*, 782.

[9] G.-B. Liao, P. B. Bareil, Y. Sheng, A. Chiou, *Opt. Express* **2008**, *16*, 1996.

[10] P. H. Jones, O. M. Maragò, G. Volpe, In *Optical Tweezers Principles and applications*; Cambridge University Press: Cambridge, 2015; pp. 19–41.

[11] A. A. M. Bui, A. B. Stilgoe, I. C. D. Lenton, L. J. Gibson, A. V. Kashchuk, S. Zhang, H. Rubinsztein-Dunlop, T. A. Nieminen, *J. Quant. Spectrosc. Radiat. Transf.* **2017**, *195*, 66.

[12] P. Kim, *MATLAB Deep Learning*; 1st ed.; Apress, 2017.

[13] J. J. Hopfield, *Proc. Natl. Acad. Sci. U. S. A.* **1982**, *79*, 2554.

[14] Z. Wang, Y. Liu, L. Weilai, F. Yu Vincent, Z. Zhou, *Biomed. Opt. Express* **2021**, *12*, 7568.

[15] I. C. D. Lenton, G. Volpe, A. B. Stilgoe, T. A. Nieminen, H. Rubinsztein-Dunlop, *Mach. Learn. Sci. Technol.* **2020**, *1*, 045009.

[16] A. Callegari, M. Mijalkov, A. B. Gököz, G. Volpe, *J. Opt. Soc. Am. B* **2015**, *32*, B6.

[17] F. Chollet *et al.* (**2015**), Keras (https://keras.io)

[18] O. M. Maragó, F. Bonaccorso, R. Saija, G. Privitera, P. G. Gucciardi, M. A. Iatì, G. Calogero, P. H. Jones, F. Borghese, P. Denti, V. Nicolosi, A. C. Ferrari, *ACS Nano* **2010**, *4*, 7515.

[19] P. H. Jones, F. Palmisano, F. Bonaccorso, P. G. Gucciardi, G. Calogero, A. C. Ferrari, O. M. Maragó, *ACS Nano* **2009**, *3*, 3077.

7. THEORETICAL INVESTIGATION OF OPTICAL TRAPPING OF A SICKLE CELL WITH A DOUBLE BEAM OPTICAL TWEEZER.

In this chapter, I report a preliminary study on the theoretical investigation of the optical trapping of sickle cells, a pathological morphology of red blood cells. Unlike healthy erythrocytes, the symmetry of a sickle cell is greatly reduced from a morphological point of view, and thus a simple mathematical description is not available in performing ray-tracing. For this reason, I introduce a new ray-tracing approach which needs only a points cloud definition for the particle's surface. This new approach is used to investigate a possible equilibrium configuration of the optically trapped cell within a double-beam optical tweezers through the dynamic equilibrium searching.

7.1. Introduction

Sickle cell anaemia is an hereditary genetic disorder that affects the molecular structure of Haemoglobin (Hb). In patients affected by sickle cell anaemia the alteration of the Hb molecular structure is due to a change in a single amino

acid in the Hb β-chain (sHb).[1,2] In subjects affected by sickle cell disease, at low oxygen level sHb shows low solubility and tend to aggregate and polymerize[3] causing morphological changes in the conformation of the healthy RBC.[4] sHb concentration and deoxygenation rate strongly influence the polymerization process inducing a variety of cell deformations and associated morphologies.[5] The morphological changes due to sHb polymerization also affects the cells' mechanical properties, including the cell membrane elasticity.[6,7] These biomechanical alteration can lead to vessel occlusion, tissue damage, organ failure, and in the most severe case even death.[8]

Optical Tweezers (OT) are an useful tool able to confine and manipulate micron-sized particles with a refractive index higher than that of the surrounding medium.[9] So far OT have been widely apply to investigate various biochemical and biophysical properties of RBC.[10] Among other applications, researchers have used OT to sense the membrane elasticity of healthy and unhealthy RBC. In this type of applications, OT have been used to trap and stretch RBC as explained in chapter 3.[11,12]

The RBC elongation has been successfully used in our laboratory to evaluate the RBC's deformability of healthy patients and patients affected by type 2 diabetes.[13] Such an approach could be easily extended to measure the extent of

membrane elasticity of erythrocytes affected by the sickle disease (sRBC). For this reason, in this last chapter, I report a preliminary work on the theoretical investigation of optical trapping of red blood cell with a pathological morphology (i.e. Sickle Cell).

7.2. Mathematical description of sickle cells

Healthy red blood cells possess a biconcave disk shape and are quite elastic allowing them to deform to pass through capillaries.[14] In patients affected by the sickle cell disease, low oxygen concentration fosters red blood cell sickling and the decrease of the cell's elasticity. Sickled cells fail to return to normal shape when normal oxygen tension is restored. Sickled cells can assume a variety of different shape but the best know are that of a sickle or the letter “C”.[4] Figure 7.1-a shows scanning electron microscope micrograph of a sickle cell and a healthy RBC. Compared to a healthy RBC, a sickle cell presents an elongated shape, and the symmetry of the object is greatly reduced.

To describe the sickle cell morphology, one has to define two surfaces of the cell as suggested by Lei *et al*.[16] In this mathematical description the upper and the lower

surfaces can be described by a polynomial function that reads:

$$f(x,y) = \alpha_0 + \alpha_1 x^2 + \alpha_2 y^2 + \alpha_3 x^4 + \alpha_4 y^4 + \alpha_5 x^2 y^2 \quad 7.1$$

where α_0, α_1,…,α_5 are fitting coefficients determined by the specific shape of the cell. The boundaries of the cell on the x-y plane are defined as:

$$\left(\frac{x}{b_1}\right)^p + \left(\frac{y}{b_2}\right)^p = 1 \quad 7.2$$

where b_1, b_2 and p vary for different cell morphology. For a sickle cell b_1 = 5.80, b_2 = 3.05 and p = 1.54, while the values of the coefficients α_0, α_1,…,α_5 for the upper and lower halves of the cell are reported in Table 7.1. In Figure 7.1-b is shown a 3D rendering of the cell surface obtained via eq. 7.1 with the parameters reported in Table 7.1.

	α_0	α_1	α_2	α_3	α_4	α_5
S^l	-0.81	-0.11	-6.78×10^{-3}	2.12×10^{-2}	2.01×10^{-2}	2.84×10^{-2}
S^u	1.36	-0.04	0.31	-1.69×10^{-3}	-3.60×10^{-2}	-2.77×10^{-2}

Table 7-1. Fitting parameters for the lower (S^l) and upper (S^u) surface of the sickle cell.

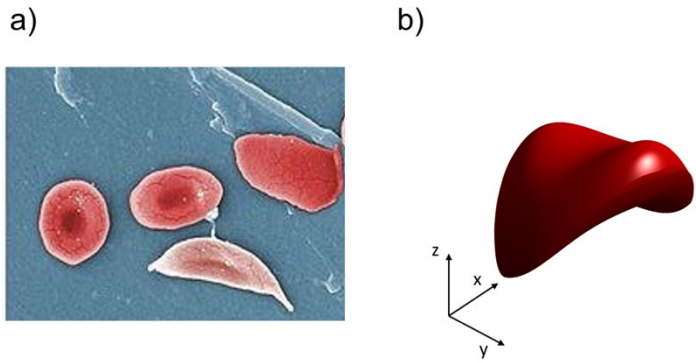

Figure 7.1. Scanning electron micrograph of healthy and sickled erythrocyte (a). Image adapted from [15]. 3D rendering of the sickle cell morphology generated through eq. 7.1.

7.3. Ray tracing methods

Unlike a healthy RBC, the symmetry of the sickled cell is much reduced, and the mathematical description relies on describing the upper and lower surfaces separately. For this reason, alternative strategies to perform the ray trace and extract the point of intersection with an optical ray, and the unit normal vector at the point of intersection are required. A possible solution requires the subdivision of the cell's surface in triangular meshes which are then intersected with the incoming light rays.[17] The surface meshing can be obtained by a points cloud describing the cell surface via the MatLab function alphaShape, Figure 7.2-a. Once the surface is subdivided in a set of triangles, one has to calculate the

intersection points between the light ray and the cell surface (*i.e.* set of triangles). Several algorithms able to perform this task have been developed, but the Möller–Trumbore ray-triangle intersection algorithm is one of the fastest.[18] This algorithm is implemented in the MatLab function TriangleRayIntersection developed by Jarek Tuszynski.[19]

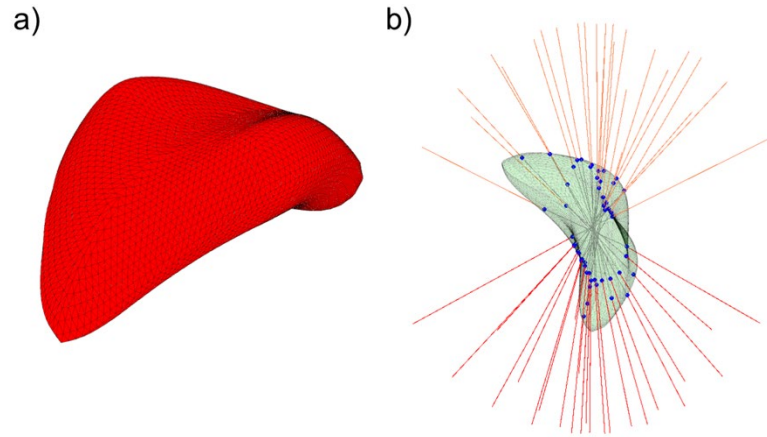

Figure 7.2. a) Surface triangulation for a sickle cell (with surface described by Eq. 7.1), and ray trace for 25 optical ray (b). In red the incoming ray, in grey the ray travelling within the cell and in orange the exiting ray. In blue are visualised the points of intersections.

Moreover, the unit normal vector can be readily calculated via the cross product between the edges of the triangle within which the ray intersects the cell's surface. This code is coupled with optical tweezers in geometrical optics (OTGO) program writing a new object.[20] Importantly, this

new object is able to perform ray optics calculations for every particle which surface is not analytically defined (*e.g.* points cloud generated for the two portion of the sickle cell). As an example, in Figure 7.2-b is shown a ray trace for a sickle cell in a single-beam optical tweezer.

7.4. Code testing

To verify the calculations made with the new algorithm, I compare the output of the standard OTGO code with the newly written code for a simple geometrical shape like a sphere for which the standard OTGO object uses an analytical definition. For this initial tests, I consider a single-beam optical tweezers (SBOT) centred in (0, 0, 0), the wavelength of the incoming beam is λ = 1.064 μm, and the beam power is 5 mW. The particle diameter is 3 μm, the refractive index of the particle is 1.38 while those of the surrounding medium is 1.33.

Figure 7.3-a shows the force-displacements curves obtained with the new object for particle displacements along the x-direction. As expected, $F_x(x)$ decreases linearly and vanishes with negative slope at x_{eq} = 0 μm, while $F_y(x)$ and $F_z(x)$ fluctuate around 0. In Figure 7.3-b and -c are shown the direct comparisons between the calculations made with the standard OTGO object and the new code for $F_x(x)$ and $F_z(z)$, respectively. Here, it is clearly evident that the numerical

results obtained with the new algorithm are in complete agreement with those obtained with the standard OTGO object.

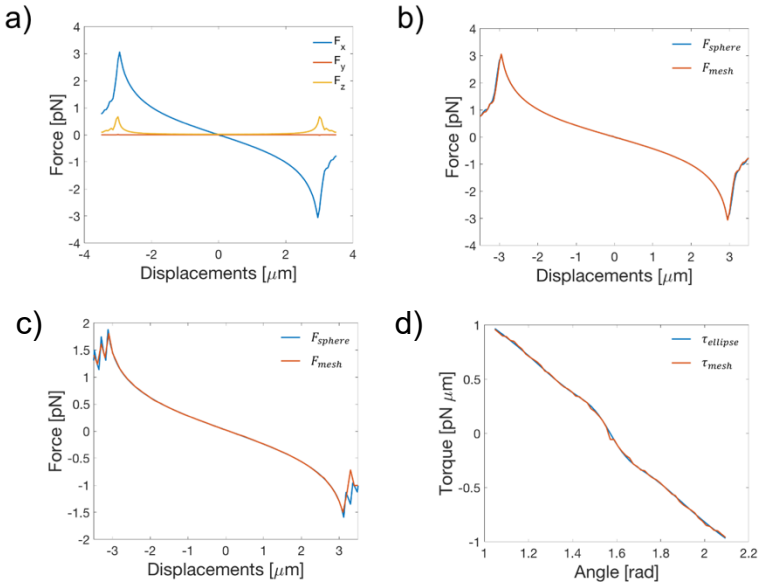

Figure 7.3. a) Force-displacements curve along the x-direction for a spherical particle calculated with the new algorithm in terms of the Cartesian components. Comparison for $F_x(x)$ and $F_z(z)$ for the new code (numerical) and the standard OTGO object (analytical) in (b) and (c), respectively. (d) Optical torque acting on an ellipsoid for rotation around the x-axis calculated with the standard OTGO object (analytical) and with the new code (numerical).

Lastly, since the most general cases involve non-spherical particles, I tested also the ability of the new object to calculate the optical torque (τ) generated by a SBOT. For this test, I used an ellipsoid (semi axes: a = 4 μm, b = 4 μm,

c = 1 μm). In a SBOT the ellipsoidal particle experiences a torque that confines the major axis of ellipsoid on the optical axis and a restoring torque must be clearly visible for this rotation. Figure 7.3-d shows the direct comparison of the optical torque calculated with the standard OTGO object (sphere or ellipse) with that obtained with the new code (mesh). Here, it is possible to appreciate that the numerical results are essentially overlapped, confirming the ability of the new code to calculate the optical force and torque correctly.

It must be mentioned that the number of meshes is a critical parameter. In fact, if the number of meshes is not sufficiently high, the precision of the calculations decreases considerably leading to numerical errors. On the other hand, a very high number of meshes would increase the calculation precision but the computation time becomes considerably longer making it unpractical for some applications. Therefore, the right trade-off between computation time and precision of the calculations must be adapted to the specific task (e.g. static equilibrium searching or dynamic equilibrium searching). The right trade-off between the number of meshes and the computations accuracy could be explored by evaluating the convergence of the new algorithm towards the standard OTGO method used for this calculation. To test this, one can calculate the optical forces and torques acting on an

ellipsoid with the aforementioned properties at $1 \cdot 10^3$ random location and orientation with the new object (keeping the number of light ray fixed). Then, the total optical forces and torques at each location and orientation can be directly compared to the results obtained through the standard OTGO object for an ellipsoid at the same location and orientation. This can be repeated for ellipsoids approximated with an increasing number of triangular meshes. For example, if the surface of the ellipsoid is subdivided into 92 triangular meshes one obtains a NMSE in respect to standard method of $\sim 8 \cdot 10^{-2}$ (and $\sim 4 \cdot 10^{-1}$ for the optical torques). On the other hand, if one uses 1740 triangular meshes to approximate the surface of the object one obtains a NMSE of $\sim 2 \cdot 10^{-3}$ (and $\sim 3 \cdot 10^{-2}$ for the optical torques). However, the computation time increases from $\sim 3 \cdot 10^2$ s to $\sim 9 \cdot 10^2$ s when the number of meshes is increased ~20 times.

7.5. Dynamic equilibrium searching

As mentioned previously, the shape of sickle cell is highly complex, and the equilibrium configuration of the cell within a double-beam optical tweezers is not *a priori* obvious. For this reason, I follow the approach adopted in chapter 4 and I use the dynamic equilibrium searching to obtain a possible equilibrium configuration for the sickle cell.

The parameters describing the incoming beams, the solution, the cell physical properties and the simulation parameters are unchanged in respect to those reported in chapter 3 for a double-beam optical tweezer, with the exception that the distance between the two beams' foci, here, is 9 μm. With this separation, the two beams' foci fall within the cell's tips, avoiding any interaction with the central portion of the cell. Yet, the numerical scheme to simulate the particle's dynamic in a force-field is unchanged and follows what reported in chapter 4.

As previously, the numerical investigation starts by calculating the diffusion the tensor ($\boldsymbol{D}$) for the particle under investigation via winHYDRO++.[21] In calculating $\boldsymbol{D}$, the sickle cell is oriented with its major axis along the x-direction as schematically depicted in Figure 7.1-b. In the current case $\boldsymbol{D}$ reads:

$$\boldsymbol{D}_{tt} = \begin{bmatrix} 7.116 \times 10^{-14} & 7.373 \times 10^{-21} & -2.483 \times 10^{-20} \\ -1.310 \times .10^{-20} & 6.391 \times 10^{-14} & -2.729 \times 10^{-21} \\ -9.602 \times 10^{-20} & 9.612 \times 10^{-21} & 5.902 \times 10^{-14} \end{bmatrix} 7.3$$

$\boldsymbol{D}_{rt}$=

$$\boldsymbol{D}_{tr}{}^{T} = \begin{bmatrix} 5.920 \times 10^{-15} & 6.897 \times 10^{-10} & 1.153 \times 10^{-15} \\ 6.897 \times 10^{-10} & -1.311 \times 10^{-15} & 2.412 \times 10^{-16} \\ 9.618 \times 10^{-16} & -8.168 \times 10^{-17} & -4.448 \times 10^{-16} \end{bmatrix} 7.4$$

$$\boldsymbol{D}_{rr} = \begin{bmatrix} 4.287 \times 10^{-03} & 3.516 \times 10^{-10} & -1.051 \times 10^{-09} \\ 1.387 \times 10^{-09} & 2.300 \times 10^{-03} & 2.635 \times 10^{-10} \\ -1.018 \times 10^{-11} & -3.078 \times 10^{-10} & 2.361 \times 10^{-03} \end{bmatrix} 7.5$$

In eq. 7.3-7.5 are reported the 3 x 3 blocks of $\boldsymbol{D}$. The numerical values of $\boldsymbol{D}_{tr}$ and $\boldsymbol{D}_{tr}{}^{T}$ show that the coupling between rotation and translation around x and y-direction are several order of magnitude higher in respect to the other terms. This is a consequence of the cell shape and represent a major difference in respect to the healthy RBC. Therefore, I expect a strong coupling in the cell's motion intrinsically due to the cell hydrodynamics.

I now proceed to identify the equilibrium configuration of sRBC in a DBOT exploiting the dynamic equilibrium searching method. Initially, the centre of mass of the cell is placed at the origin of the fixed reference frame, and the cell is orientated along the x-direction in its flat configuration (i.e. the concave portion faces downward). Therefore, the light beams are turned on at t = 0 s, and the simulation are let to proceed with Δt = 0.001 s for 10 s.

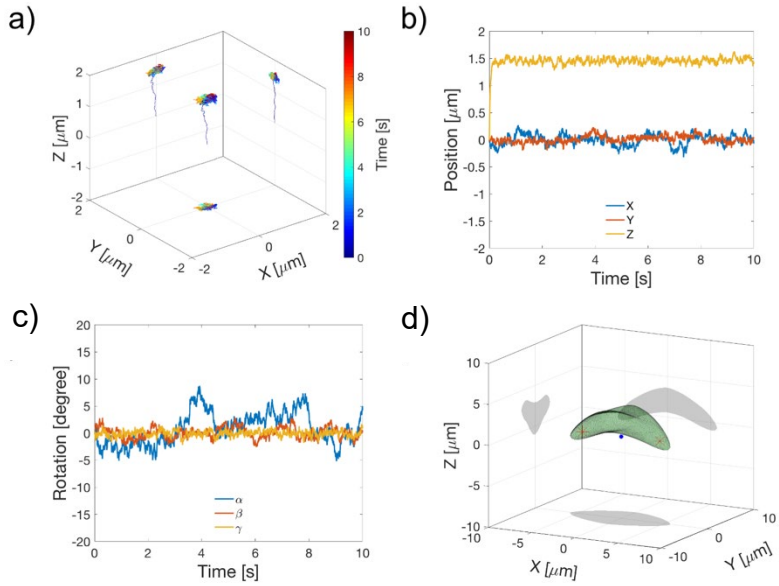

Figure 7.4. a) 3D-trajectory of the centre of mass of a sRBC over a simulation time of 10 s. (b) Position of the centre of sRBC as a function of time in terms of the Cartesian co-ordinates, and (c) cell rotation around the axis of the fixed reference frame (i.e. x- (α), y- (β), and z- (γ)). (d) sRBC at the equilibrium configuration. The red star indicates the position of the beams' foci, while the blue dot represents the origin of the fixed frame of reference.

Figure 7.4-a shows the 3D-trajectory of the sRBC centre of mass while in Figure 7.4-b and -c are shown the position of the sRBC centre of mass in terms of the Cartesian co-ordinates, and the cell rotation around the x- (α), y- (β), and z-axis (γ) of the fixed reference frame, respectively. Initially, under the influence of the scattering force, the cell

migrates from its initial position (i.e. $x = 0, y = 0, z = 0$) along the optical axis towards positive $\hat{\boldsymbol{z}}$. This motion is not accompanied by any re-orientation or strong motion along the transverse directions. Lately, the cell finds its equilibrium configuration within few milliseconds at $x = 0.006 \pm 0.001$ µm, $y = 0.002 \pm 0.001$ µm, and $z = 1.586 \pm 0.0515$ µm, without any significant rotation around any axis ($\alpha = 0.021 \pm 0.005°$, $\beta = 0 \pm 0.02°$, $\gamma = 0 \pm 0.001°$) as shown in Figure 7.4-c and -d. Figure 7.5 shows the correlation plots between the translations and the rotations. Here along the diagonal are present the histogram of each co-ordinate while the off-diagonal plots shown the correlation between two co-ordinates. From this plot, it is immediately evident that some terms are strongly correlated ($x - \beta$ and $y - \alpha$, correlation coefficient < -0.7 and > 0.7, respectively), while others are essentially non-correlated or weakly correlated. This suggests that some cross-terms are present also in the stiffness matrix, and that the decay of the autocorrelation functions are not single or double exponentials, but a sum of multiple exponentials which are not easily identifiable.

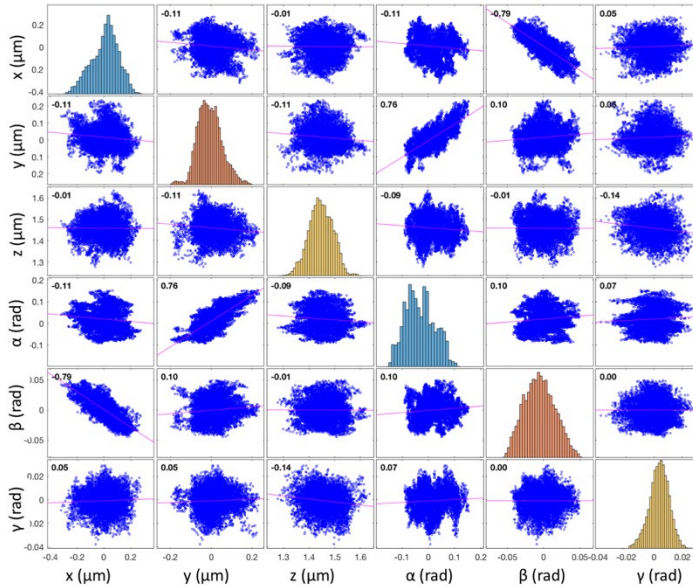

Figure 7.5. Translation-rotation correlation plots.

To verify the presence of cross-terms in the stiffness matrix (i.e. $F_x = -k_x x - k'\beta$) I evaluate $F_x(\beta)$, $F_y(\alpha)$, $\tau_x(y)$ and $\tau_y(x)$. Figure 7.6 and -b show that $F_x(\beta)$ and $\tau_x(y)$ have unstable equilibrium positions and orientations causing a continuous 'circulating' motion of the cell within the optical trap. Similarly, $F_y(\alpha)$ and $\tau_y(x)$ shows the presence of strongly coupled terms, Figure 7.6 and -d. These findings confirms that strong coupling are present also in the stiffness matrix.

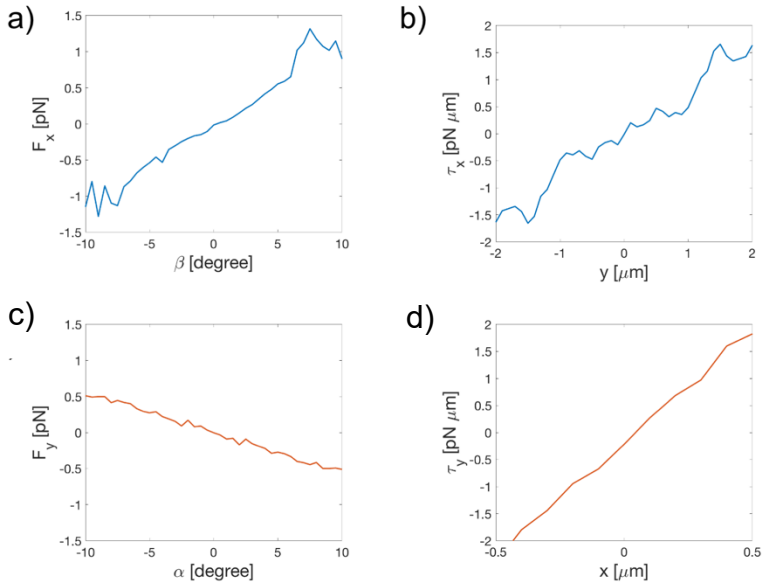

Figure 7.6. Force-rotations and torque-displacements curve for $F_x(\beta)$ (a), $\tau_x(y)$ (b), $F_y(\alpha)$ (c), and $\tau_y(x)$ (d).

Now I evaluate the auto-correlation function as I introduced in chapter 6. From Figure 7.7-a, -b and -c, it is possible to observe that $C_{xx}(\tau)$, $C_{yy}(\tau)$ and $C_{zz}(\tau)$ decay as multiple exponentials characterized by different ω. Therefore, it is not possible to resort on the modelling reported in chapter 6 to characterise the trap constant. Indeed, for this reason, new methodologies, as for example FORMA[22] must be adapted to the current case to characterise the trap constant or new one must be developed.

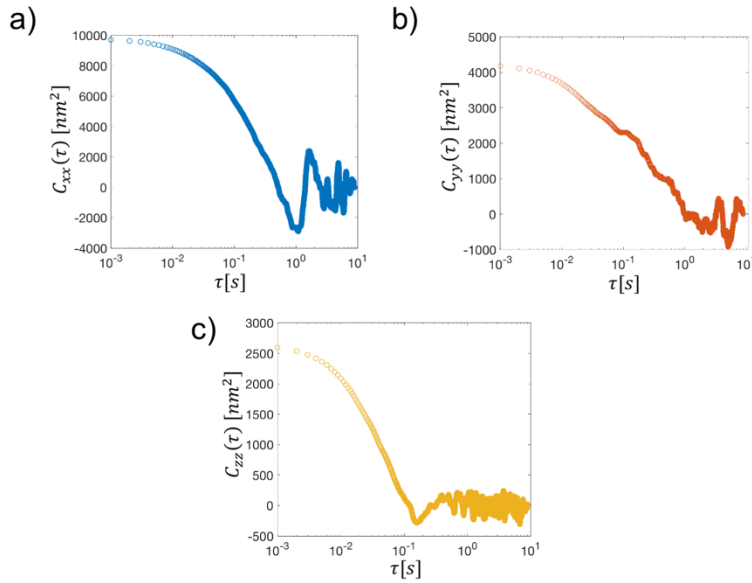

Figure 7.7. Autocorrelation function for the centre of mass of the cell for the x-direction (a), y-direction (b), and z-direction (c).

The peculiar morphology of the sickle cell, however, also permits an alternative equilibrium configuration similar to the 'folded' configuration (i.e. rotated of 90° around the x-axis) found for a healthy RBC. In Figure 7.8 are shown the results for a simulation of sickle cell in its 'folded' configuration carried out with the same parameters used previously. Here, the only difference is the total beams' power is set at 40 mW (i.e. 20 mW each beam). The beam power is increased to make any possible shifting in the cell configuration more visible.

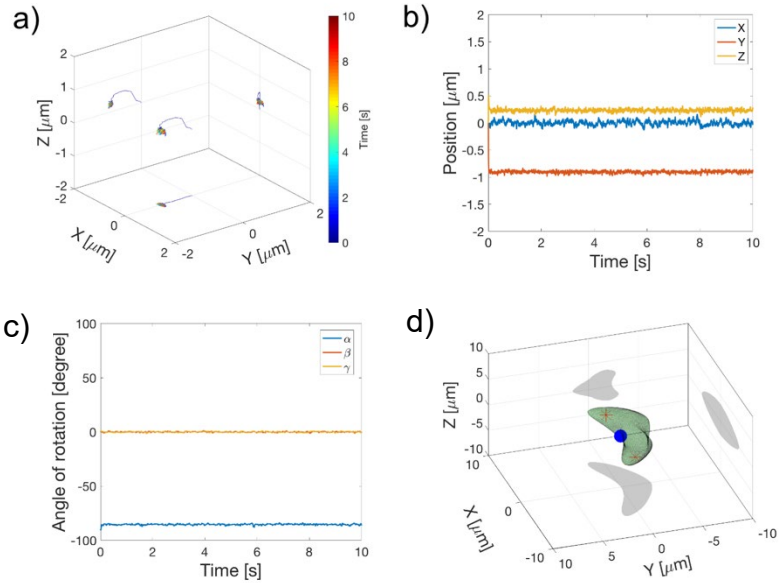

Figure 7.8. a) 3D-trajectory of the centre of mass of a sRBC over a simulation time of 10 s. (b) Position of the centre of sRBC as a function of time in terms of the Cartesian co-ordinates, and (c) cell rotation around the axis of the fixed reference frame (i.e. x- (α), y- (β), and z- (γ)). (d) sRBC at the equilibrium configuration. The red star indicates the position of the beams' foci, while the blue dot represents the origin of the fixed frame of reference.

Initially, the cell, centred in (0, 0, 0) in its 'folded' configuration, starts to migrate towards -$\hat{\boldsymbol{y}}$ and stabilize at approximately y_{eq}=-1 μm because of the cell morphology. Simultaneously, the cell migrates towards +$\hat{\boldsymbol{z}}$ and stabilize at around z_{eq}=+0.25 μm, while the centre of mass of the cell

floats around x_{eq}=0, Figure 7.8-a and -b. Interestingly, the cell seems to be confined in its 'folded' configuration as illustrated in Figure 7.8-c and -d. This is a major difference in respect with a healthy RBC trapped by double-beams optical tweezers. In fact, in the latter case, an increase in the beams' power would result in a stiffer trap but the cell would not change its equilibrium orientation. These findings are also supported by experiments in which alternative equilibrium orientations have never been observed so far. Indeed, because of the cell morphology, the RBC would remain aligned with the beams' propagation direction.

7.6. Chapter summary

In this chapter, I briefly introduced a methodology to perform the ray-tracing and to calculate the optical forces and torques on asymmetrical particle which surface is not easily described by a single function. Indeed, a particle surface description as a points cloud is the only feature necessary to perform the geometrical optics calculation. In particular, the points cloud is meshed in a set of triangles and a ray-triangle intersection algorithm is used to extract the necessary information (i.e. point of intersection and normal line to the point of intersection) to complete the ray trace and to calculate the optical forces and torques. The new algorithm showed to be in good agreement with the standard method used to calculate the optical forces and torques in the geometrical optics approximation. Importantly, the new method was applied to identify the equilibrium position of a sickle cell, a pathological RBC morphology, via the dynamic equilibrium searching. Even though an equilibrium configuration is easily identified, the extrapolation of the trap constants from the particle trajectories is not trivial because of the strong coupling between rotations and translations. A new theory able to extract the trap constant must be developed or adapted from the current available methodology but remains outside the scope of the thesis.

Importantly, the geometrical optics calculation performed with the presented methodology can be expanded to any particle shape, and can also be used as a training data set for a neural network as introduced in chapter 6.

7.7. Bibliography

[1] L. Pauling, H. A. Itano, S. J. Singer, I. C. Wells, *Science (80-.).* **1949**, *110*, 1488.

[2] B. V. M. Ingram, *Nature* **1957**, *180*, 326.

[3] R. E. Samuel, E. D. Salmon, R. W. Briehl, *Nature* **1990**, *345*, 833.

[4] G. W. Christoph, J. Hofrichter, W. A. Eaton, *Biophys. J.* **2005**, *88*, 1371.

[5] L. W. Diggs, J. Bibb, *J. Am. Med. Assoc.* **1939**, *8*, 695.

[6] R. Hoover, R. Rubin, G. Wise, R. Warren, *Blood* **1979**, *54*, 872.

[7] R. P. Hebbel, O. Yamada, C. F. Moldow, H. S. Jacob, J. G. White, J. W. Eaton, *J. Clin. Invest.* **1980**, *65*, 154.

[8] O. S. Platt, D. J. Brambilla, W. R. Rosse, P. F. Milner, O. Castro, M. H. Steinberg, P. P. Klug, *e New Engl. J. Med.* **1994**, *330*, 404.

[9] A. Ashkin, J. M. Dziedzic, J. E. Bjorkholm, S. Chu, *Opt. Angular Momentum* **1986**, *11*, 288.

[10] R. Zhu, T. Avsievich, A. Popov, I. Meglinski, *Cells* **2020**, *9*, 545.

[11] R. Agrawal, T. Smart, J. Nobre-Cardoso, C. Richards, R. Bhatnagar, A. Tufail, D. Shima, P. H. Jones, C. Pavesio, *Sci. Rep.* **2016**, *6*, 1.

[12] G.-B. Liao, P. B. Bareil, Y. Sheng, A. Chiou, *Opt.*

Express **2008**, *16*, 1996.

[13] R. Agrawal, B. Ang, P. K. Balne, C. Richards, T. Smart, J. Cardoso, D. Shima, P. H. Jones, C. Pavesio, *Ocul. Immunol. Inflamm.* **2019**, *27*, 978.

[14] E. Evans, Y. C. Fung, *Microvasc. Res.* **1972**, *4*, 335.

[15] O. K. Clarence, S. Chukwunyelum, C. Perpetua, *Int. J. Med. Med. Sci.* **2015**, *5*, 299.

[16] H. Lei, G. E. Karniadakis, *Biophys. J.* **2012**, *102*, 185.

[17] A. S. Glassner, *An Introduction to Ray Tracing*; Glassner,.; Academic Press: London, 1989.

[18] T. Möller, B. Trumbore, *J. Graph. Tools* **1997**, *2*, 1.

[19] Y. H. Tan, M. Liu, B. Nolting, J. G. Go, J. Gervay-hague, G. Liu, *ACS Nano* **2008**, *2*, 2374.

[20] A. Callegari, M. Mijalkov, A. B. Gököz, G. Volpe, *J. Opt. Soc. Am. B* **2015**, *32*, B6.

[21] J. García de la Torre, J. G. Hernández Cifre, *J. Mol. Biol.* **2020**, *432*, 2930.

[22] L. Pérez García, J. Donlucas Pérez, G. Volpe, A. V. Arzola, G. Volpe, *Nat. Commun.* **2018**, *9*, 1.

8. CONCLUSION

In this thesis, I presented a comprehensive study on the theoretical investigation of erythrocyte optical trapping via optical tweezers exploiting the geometrical optics approximation. The thesis was subdivided in two parts. Part I is divided in two chapters where I briefly introduced the structure, the biology and the physiology of erythrocytes and the physics that is used throughout the thesis. Part II is stranded in five chapters where I presented the results obtained during my studies.

In the first chapter of Part II, I presented a theoretical investigation of the optical trapping of a healthy RBC when trapped by a single- or multi-beams optical tweezers. The investigation highlight how the biconcave shape is critical in determining the rays' path, the optical forces and torques, and thus the equilibrium configuration of a healthy RBC. The methodology used to explore the equilibrium configuration of the healthy RBC within an optical trap has been showed for a single-beam optical tweezers, and then, has been applied to investigate the possibility to completely confine a RBC in space by means of a double-beam optical tweezers. Moreover, it has also been shown that using three or four beams in a very symmetric arrangements confines the cell in

its 'flat' configuration in very good agreement with the experimental evidence.

In the second chapter of Part II, I studied how a reconfigurable triple-beam optical tweezers can control the orientation and the position of a healthy RBC using two different methods for the identification of the equilibrium configuration. The static equilibrium searching proven to be an excellent scheme to explore the trapping mechanism if the equilibrium configuration of the cell is known from experiments or if the trap configuration assumes simple geometrical arrangements. However, as the complexity of the trap configuration increases, the static equilibrium searching becomes too difficult in identifying the final configuration of the cell within the optical trap. For this reason, simulating the non-spherical particles' Brownian dynamics within the force-field demonstrated to be an essential step. In fact, with the dynamic equilibrium searching has been possible to identify the final equilibrium position and orientation even in highly complex light distribution patterns.

In the third chapter of Part II, I reported a numerical investigation on the application of light-sheet optical tweezers in RBC research. Initially, I verified the possibility to optically trap an RBC with a light-sheet of infinite width. Subsequently, I demonstrated how a light-sheet optical tweezers is able to completely confine a healthy RBC, both spatially and

rotationally. A complete trapping was obtained if the light-sheet had a width comparable to the cell diameter. Since with a light-sheet tweezers the RBC is confined in a specific plane, the rotation of the light-sheet can be used to deliberately re-orient the cell via the simple light-sheet rotation.

In the fourth chapter of Part II, it was introduced a preliminary study carried out in collaboration with Nano-Soft Lab at CNR in Messina, Italy. In this work, we trained an artificial neural network (NN) to predict the optical forces and torques generated by a single-beam optical tweezers on a healthy RBC. The NN is demonstrated to be able to predict the optical forces and torques with higher accuracy and in significantly shorter computation time compared to geometrical optics calculation. Moreover, the NN can be used to predict optical forces and torques for multiple-beams optical tweezers, and thanks to the higher computational efficiency, the NN is used to simulate the Brownian dynamic of a trapped RBC in a double-beam optical tweezers. Lastly, the results of the simulation are used to extract the trap constants via the auto-correlation method.

In the fifth chapter of Part II, I briefly introduced a methodology to perform the geometrical optics calculation on asymmetrical particle which surface is described only by a points cloud. The points cloud is subdivided in a set of interconnected triangles and a ray-triangle intersection

algorithm is used to extract the necessary information to complete the ray trace and to calculate the optical forces and torques. The new algorithm demonstrated to be in good agreement with the standard method used to calculate the optical forces and torques. Importantly, this new method has been coupled with the dynamic equilibrium searching to identify the equilibrium configuration of a pathological RBC morphology. Notably, the geometrical optics calculation performed with the presented methodology can be expanded to any particle shape, and can also be used as a training data set for a neural network.

The implemented numerical procedure can be exploited by experimentalists to tweak various parameters. For example, one can explore light beams with various intensity distributions (e.g. Laguerre-Gaussian beam or Hermite-Gaussian beam) to analyse the effect on trapping a healthy or an unhealthy erythrocyte. Another example that can be explored is the distance between the two beams' foci in a double-beam optical tweezers for elongation experiments. Of great interest, for both theorists and experimentalists, is the possibility to simulate the light stress distribution on the surface of the cell. This calculation can be coupled to finite difference (and/or elements) method or other numerical techniques to simulate the deformation of a red blood cell in response to the optical pressure for a given set

of input. Such methodologies can also be useful to extract real world values regarding the biomechanics of the cell. Also, the numerical method here developed can be exploited to investigate new theoretical framework for the calibration of optical tweezers.

In performing numerical experiments some simplifying approximations have been made which impacts several aspects of my work. One great example is the approximation of the cell as a rigid body with fixed and predefined morphological features (e.g. dimple depth). This could limit the possibility to compare quantitatively numerical experiments with the real world outcome of a direct investigation, nevertheless a good qualitative agreement has been already shown. Yet, the rigid body approximation (currently) limits the applicability of the developed NN to the basic case of a healthy RBC. Though, in future a more sophisticated neural network could be trained to predict optical stress distribution, cells deformation, and the new optical forces/torques acting on the deformed RBC for a given set of inputs. Although, the generation of the training data set could be a formidable task. Notwithstanding the limitations, in the current thesis the power of the method has been demonstrated for an important task like the trap calibration. These said, a detailed experimental validation of

the numerical method is still required to identify the boundary of applicability of the numerical framework here presented.

Overall, in this thesis, the great potential of the geometrical optics approximation has been exploited in full and different methodologies have developed to study various aspect of optical trapping healthy and unhealthy red blood cell. Taken as whole the work presented in this thesis offers an advancement in the theoretical understanding of the red blood cell optical trapping through optical tweezers.

9. FUTURE OUTLOOK

The great potential of the methods developed in this thesis has a farther reach outside the red blood cell research. The methodologies developed in chapter 6 and 7 can be a great advantage for the entire optical tweezers community. In fact, the possibility to calculate optical forces on particle with a non-well-defined geometry could be used in other fields as for example in calculating the optical forces acting astronomical dust particles (an example is shown in Figure 9.1), microplastics, or on any other residues derived from human activity. In addition, all these calculations can be coupled with machine learning algorithm to improve the calculations speed. The work in this thesis, therefore, extends the capabilities of geometrical optics to describing forces and torques on irregularly shaped objects, with expected impact not just in physics, but medicine and environmental science also.

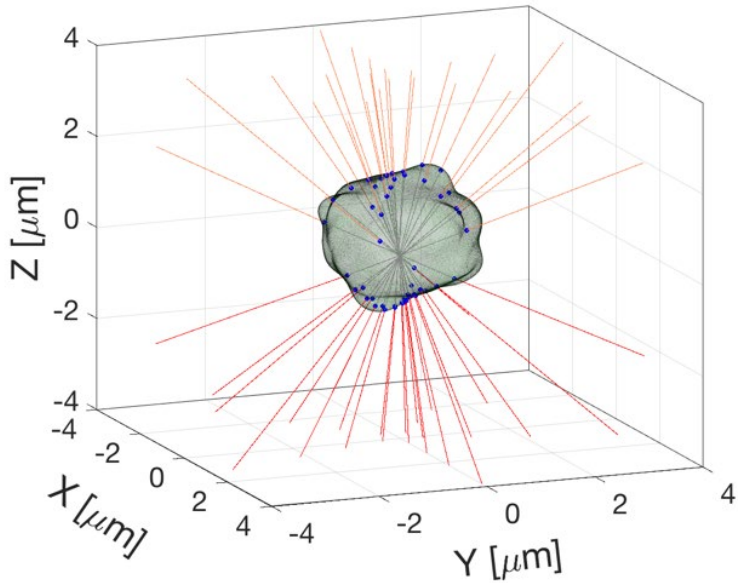

Figure 9.1. Ray trace for an irregularly shaped particle. The ray trace has been performed with the methodology explained in chapter 7.

10. APPENDIX

10.1. Ray triangle intersection with Möller–Trumbore algorithm

The principal information that need to be extracted to perform the ray trace are the point of intersection and the normal line to the point of intersection. However, if the particle lacks of simple geometrical description, one has to resort on the meshing of the surface in a set of triangles to perform geometrical optics calculations. This requires a new algorithm to extract the necessary information. Here I briefly details the maths behind the Möller–Trumbore's ray-triangle intersection method used in chapter 7, and extensively discussed in [1].

A light-ray can be defined by its origin ($\boldsymbol{O}$), its direction ($\boldsymbol{D}$), and a single scalar t that defines a point along the light-ray:

$$\boldsymbol{R}(t) = \boldsymbol{O} + t\boldsymbol{D}. \qquad A.1$$

Here, the light-ray has to be intersected with all the triangles that composes the particle surface. In this algorithm, the authors made use of the barycentric co-ordinate to define

any point inside the triangle with vertices ($\boldsymbol{V}_0$, $\boldsymbol{V}_1$, $\boldsymbol{V}_2$). Following this definition, a point in a triangle is given by:

$$\boldsymbol{T}(u,v) = (1-u-v)\boldsymbol{V}_0 + u\boldsymbol{V}_1 + v\boldsymbol{V}_2 \qquad A.2$$

where (u,v) are the barycentric co-ordinates, which must fulfil $u \geq 0$, $v \geq 0$, and $u+v \leq 1$. To find the intersection one has to equate eq. A.1 and A.2 and solve for u,v and t, as follow:

$$\boldsymbol{O} - t\boldsymbol{D} = (1-u-v)\boldsymbol{V}_0 + u\boldsymbol{V}_1 + v\boldsymbol{V}_2 \qquad A.3$$

distributing the first terms on the right hand side, and grouping the similar terms, one obtains:

$$\boldsymbol{O} - \boldsymbol{V}_0 = -t\boldsymbol{D} + u(\boldsymbol{V}_1 - \boldsymbol{V}_0) - v(\boldsymbol{V}_2 - \boldsymbol{V}_0) \qquad A.4$$

denoting $\boldsymbol{E}_1 = \boldsymbol{V}_1 - \boldsymbol{V}_0$, $\boldsymbol{E}_2 = \boldsymbol{V}_2 - \boldsymbol{V}_0$, and $\boldsymbol{T} = \boldsymbol{O} - \boldsymbol{V}_0$, eq. A.4 can be written in matrix form as:

$$[-\boldsymbol{D} \quad \boldsymbol{E}_1 \quad \boldsymbol{E}_2]\begin{bmatrix} t \\ u \\ v \end{bmatrix} = \boldsymbol{T}. \qquad A.5$$

Eq. A.5 is solved using the Cramer's rules:

$$\begin{bmatrix} t \\ u \\ v \end{bmatrix} = \frac{1}{|-\boldsymbol{D}, \boldsymbol{E}_1, \boldsymbol{E}_2|} \begin{bmatrix} |\boldsymbol{T}, \boldsymbol{E}_1, \boldsymbol{E}_2| \\ |-\boldsymbol{D}, \boldsymbol{T}, \boldsymbol{E}_2| \\ |-\boldsymbol{D}, \boldsymbol{E}_1, \boldsymbol{T}| \end{bmatrix}. \qquad A.6$$

From linear algebra it is know that $|\boldsymbol{A}, \boldsymbol{B}, \boldsymbol{C}| = -(\boldsymbol{A} \times \boldsymbol{C}) \cdot \boldsymbol{B} = -(\boldsymbol{C} \times \boldsymbol{B}) \cdot \boldsymbol{A}$, Therefore Eq. A.6 can be rewritten as:

$$\begin{bmatrix} t \\ u \\ v \end{bmatrix} = \frac{1}{(\boldsymbol{D} \times \boldsymbol{E}_2) \cdot \boldsymbol{E}_1} \begin{bmatrix} (\boldsymbol{T} \times \boldsymbol{E}_1) \cdot \boldsymbol{E}_2 \\ (\boldsymbol{D} \times \boldsymbol{E}_2) \cdot \boldsymbol{T} \\ (\boldsymbol{T} \times \boldsymbol{E}_2) \cdot \boldsymbol{D} \end{bmatrix} = \frac{1}{\boldsymbol{P} \cdot \boldsymbol{E}_1} \begin{bmatrix} \boldsymbol{Q} \cdot \boldsymbol{E}_2 \\ \boldsymbol{P} \cdot \boldsymbol{T} \\ \boldsymbol{Q} \cdot \boldsymbol{D} \end{bmatrix} \qquad A.7$$

where $\boldsymbol{P} = (\boldsymbol{D} \times \boldsymbol{E}_2)$ and $\boldsymbol{Q} = (\boldsymbol{T} \times \boldsymbol{E}_1)$. In the algorithm implementation, all calculations are delayed until they are not needed. For example v is not calculated until the value of u is found to be in an acceptable range.

The second necessary information is the unit normal line ($\boldsymbol{N}$) to the point of intersection. The latter can be readily calculated via the cross-product of the edge of the triangle, and it is then used to determine if the light ray $\boldsymbol{R}$ strike the surface from outside (Figure A.1-a) or from inside the particle (Figure A.1-b), or if it is parallel to the triangle. This test, apart determining the direction of the light ray incidence, is used to further increase the computationally efficiency of the algorithm avoiding unnecessary calculation (i.e. when the light ray is parallel to the triangle).

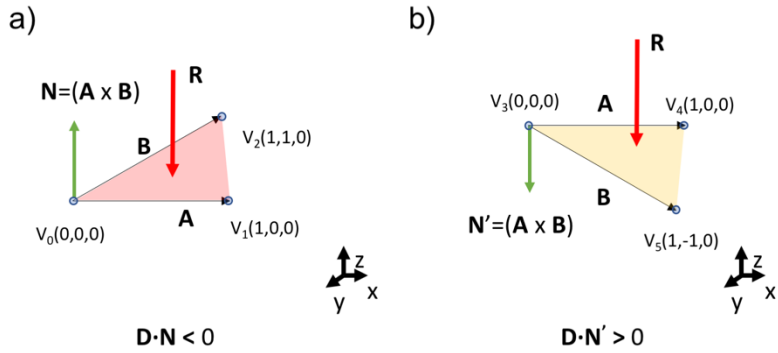

Figure A.10.1. The unit normal vector ($\boldsymbol{N}$) to a triangle can be readily calculated as the cross-product between the triangle edges $\boldsymbol{A}$ and $\boldsymbol{B}$. In (a) a light-ray $\boldsymbol{R}$ is striking the surface of the particle from outside the particle, and thus the dot product $\boldsymbol{D} \cdot \boldsymbol{N} < 0$, where $\boldsymbol{D}$ is the direction of the light-ray, since the vector are antiparallel. In (b), $\boldsymbol{R}$ hits the particle surface from inside the particle volume and thus $\boldsymbol{D} \cdot \boldsymbol{N} > 0$. A third event can occur when the $\boldsymbol{R}$ and $\boldsymbol{N}$ are perpendicular $\boldsymbol{D} \cdot \boldsymbol{N} = 0$, not shown.